CAPITAL UNIVERSITY OF SCIENCE AND TECHNOLOGY, ISLAMABAD

Design and Optimization of Ribbed Fluidic Oscillator for Enhanced Thermal-Hydraulic Performance of Impinging Sweeping Jets

by

Liaqat Hussain

A dissertation submitted in partial fulfillment for the
degree of Doctor of Philosophy

in the
Faculty of Engineering
Department of Mechanical Engineering

2026

Design and Optimization of Ribbed Fluidic Oscillator for Enhanced Thermal-Hydraulic Performance of Impinging Sweeping Jets

By

Liaqat Hussain

(DME201001)

Dr. Farukh Farukh, Associate Professor
De Montfort University, Leicester, UK
(Foreign Evaluator 1)

Dr. Yuting Jiang, Professor
Harbin Engineering University, Harbin, China
(Foreign Evaluator 2)

Dr. Muhammad Mahabat Khan
(Research Supervisor)

Dr. Muhammad Mahabat Khan
(Head, Department of Mechanical Engineering)

Dr. Imtiaz Ahmad Taj
(Dean, Faculty of Engineering)

DEPARTMENT OF MECHANICAL ENGINEERING
CAPITAL UNIVERSITY OF SCIENCE AND TECHNOLOGY
ISLAMABAD
2026

To **Allah**, my strength when I had none.

To my **mother** - your prayers my foundation,
your love my shelter.

To my **father** - your wisdom my compass,
your faith my anchor.

To those who lifted me, guided me,
and believed when I doubted.

"And whoever relies upon Allah - then He is sufficient for him." (Quran 65:3)

CAPITAL UNIVERSITY OF SCIENCE & TECHNOLOGY
ISLAMABAD
Expressway, Kahuta Road, Zone-V, Islamabad
Phone:+92-51-111-555-666 Fax: +92-51-4486705
Email: info@cust.edu.pk Website: https://www.cust.edu.pk

CERTIFICATE OF APPROVAL

This is to certify that the research work presented in the dissertation, entitled "**Design and Optimization of Ribbed Fluidic Oscillator for Enhanced Thermal- Hydraulic Performance of Impinging Sweeping Jets**" was conducted under the supervision of **Dr. Muhammad Mahabat Khan**. No part of this dissertation has been submitted anywhere else for any other degree. This dissertation is submitted to the **Department of Mechanical Engineering, Capital University of Science and Technology** in partial fulfillment of the requirements for the degree of Doctor in Philosophy in the field of **Mechanical Engineering**. The open defence of the dissertation was conducted on **December 15, 2025**.

Student Name : Liaqat Hussain (DME201001) ____________________

The Examining Committee unanimously agrees to award PhD degree in the mentioned field.

Examination Committee :

(a) External Examiner 1: Dr. Muhammad Shehryar Manzoor
Professor
National Skills University, Islamabad ____________________

(b) External Examiner 2: Dr. Talha Irfan Khan
Associate Professor
CEME, NUST, Islamabad Talha ____________________

(c) Internal Examiner : Dr. Muhammad Irfan
Associate Professor
CUST, Islamabad ____________________

Supervisor Name : Dr. Muhammad Mahabat Khan
Professor
CUST, Islamabad Mahabat ____________________

Name of HoD : Dr. Muhammad Mahabat Khan
Professor
CUST, Islamabad Mahabat ____________________

Name of Dean : Dr. Imtiaz Ahmed Taj
Professor
CUST, Islamabad ____________________

Author's Declaration

I, **Liaqat Hussain** hereby state that my PhD dissertation titled **"Design and Optimization of Ribbed Fluidic Oscillator for Enhanced Thermal-Hydraulic Performance of Impinging Sweeping Jets"** is my own work and has not been submitted previously by me for taking any degree from Capital University of Science and Technology, Islamabad or anywhere else in the country/abroad.

At any time if my statement is found to be incorrect even after my graduation, the University has the right to withdraw my PhD Degree.

Liaqat

(Liaqat Hussain)
Registration No: DME201001

Plagiarism Undertaking

I solemnly declare that research work presented in this dissertation titled **"Design and Optimization of Ribbed Fluidic Oscillator for Enhanced Thermal-Hydraulic Performance of Impinging Sweeping Jets"** is solely my research work with no significant contribution from any other person. Small contribution/help wherever taken has been duly acknowledged and that complete dissertation has been written by me.

I understand the zero tolerance policy of the HEC and Capital University of Science and Technology towards plagiarism. Therefore, I as an author of the above titled dissertation declare that no portion of my dissertation has been plagiarized and any material used as reference is properly referred/cited.

I undertake that if I am found guilty of any formal plagiarism in the above titled dissertation even after award of PhD Degree, the University reserves the right to withdraw/revoke my PhD degree and that HEC and the University have the right to publish my name on the HEC/University website on which names of students are placed who submitted plagiarized work.

Liaqat

(Liaqat Hussain)

Registration No: DME201001

List of Publications

It is certified that following publication(s) have been made out of the research work that has been carried out for this dissertation:-

1. **L. Hussain** and M. M. Khan, “Recent progress in flow control and heat transfer enhancement of impinging sweeping jets using double feedback fluidic oscillators: a review,” *Journal of Heat Transfer*, vol. 144, no. 12, p. 120802, 2022.
2. **L. Hussain**, M. M. Khan, and N. Ahmad, “Flow performance enhancement of a fluidic oscillator through the integration of rectangular ribs on Coanda surface,” *Journal of Fluids Engineering*, vol. 146, no. 11, p. 111301, 2024.
3. **L. Hussain**, M. M. Khan, and N. Ahmad, “Flow Performance Improvement of Fluidic Oscillator Through Variation in Number of Ribs on Coanda Surface,” *Journal of Fluids Engineering*, vol. 147, no. 11, p. 111201, 2025.
4. **L. Hussain**, M. M. Khan, and N. Ahmad, “Design optimization of ribbed fluidic oscillator using integrated CFD-Taguchi-GRA method,” *European Journal of Mechanics - B/Fluids*, vol. 113, p. 204284, 2025.
5. **L. Hussain**, M. M. Khan, N. Ahmad, M. Imran, and M. W. Shahzad, “Taguchi-based optimization of a fluidic oscillator for enhanced thermal-hydraulic performance of an impinging sweeping jet,” *International Communications in Heat and Mass Transfer*, vol. 166, p. 109176, 2025.
6. **L. Hussain**, M. M. Khan, M. Masud, F. Ahmed, Z. Rehman, L. Amanowicz, K. Rajski, “Heat Transfer Augmentation through Different Jet Impingement Techniques: A State-of-the-Art Review,” *Energies*, vol. 14, no. 20, p. 6458, 2021.

Liaqat

(Liaqat Hussain)
Registration No: DME201001

Acknowledgement

First and foremost, all praise and gratitude belong to **Almighty Allah**, the Most Merciful and Benevolent, for granting me the strength, perseverance, and wisdom to complete this PhD research. His divine guidance has been my greatest support throughout this journey.

I am deeply indebted to my esteemed supervisor, **Dr. Muhammad Mahabat Khan**, for his invaluable guidance, continuous encouragement, and unwavering support. His profound knowledge, insightful feedback, and dedication to research excellence have been instrumental in shaping this work. Without his mentorship, this dissertation would not have been possible.

I also extend my sincere gratitude to my research collaborator, **Dr. Naseem Ahmad**, for his constructive suggestions, technical discussions, and encouragement throughout my research. His expertise and timely advice were crucial in overcoming many challenges.

I would like to express my appreciation to the faculty members who contributed to my academic growth, particularly **Dr. Muhammad Irfan**, **Dr. Salman Sagheer Warsi**, and **Dr. Muhammad Javed Hyder**, for their excellent teaching and guidance during my coursework.

Special thanks to **Dr. Muhammad Mahabat Khan** (Head of Mechanical Engineering Department), **Dr. Muhammad Mansoor Ahmed** (Vice Chancellor, CUST) and **Dr. Imtiaz Ahmad Taj** (Dean, Faculty of Engineering) for their support in facilitating my scholarship and research endeavors.

I am also grateful to the **Mechanical Engineering Department of CUST**, particularly the **High-Performance Computing (HPC) Lab**, for providing the necessary computational resources and technical support.

To my friends **Dr. Naseem Ahmad**, **Adeel Ghani**, **Arhaam Mubarak**, and **Dr. Sarah Imam**, thank you for your motivation, intellectual discussions, and support during this journey. Your encouragement kept me going in difficult times.

Above all, I owe my deepest gratitude to my family. To my beloved **mother - Hussain Bibi**, whose prayers, sacrifices, and unconditional love have been my greatest strength, this achievement is as much hers as it is mine. I also thank my **father - Rahim Badshah** for his constant encouragement and my **siblings** for their unwavering support and belief in me.

This milestone would not have been possible without the collective support of all those mentioned. May Allah bless them all abundantly.

(Liaqat Hussain)

Abstract

The performance of sweeping jet impingement cooling depends primarily on fluidic oscillators, which serve as the key element in heat removal from heated target surfaces. Fluidic oscillators influence cooling effectiveness through their combined hydrodynamic and thermal characteristics, including fluid oscillatory motion and convective heat exchange. Significantly, the geometrical parameters of the oscillator critically affect jet oscillation characteristics and the resultant heat transfer. Numerical investigation is applied in this study to analyze the flow performance of such oscillators and their implementation in impinging jet based cooling applications. This research explores the design of a novel fluidic oscillator incorporating ribbed structures on its Coanda surface. The primary aim is to establish a structured methodology for evaluating how rib geometry over Coanda surface of the oscillator, specifically the ribs' aspect ratio, number of ribs, and angle of ribs influences its performance. For this purpose a hybrid CFD-Taguchi-Grey Relational Analysis (GRA) framework is employed to optimize the fluidic oscillator's flow performance. Subsequently, the optimum configurations, selected based on oscillation frequency and jet deflection characteristics, are tested in an impinging jet arrangement to assess their heat transfer enhancement relative to conventional smooth Coanda surface oscillator.

Initially, the effect of rectangular ribs with varying aspect ratios (ARribs = 0.64, 0.81, 1.00, 1.23 and 1.56) on Coanda-surface-driven jet oscillations using 2D unsteady RANS simulations was studied. Increasing ARribs raises oscillation frequency (up to 820 Hz vs. 355 Hz for smooth case) but reduces jet deflection angles. Ribs also lower pressure drop by 22% (ARribs = 1.56) by altering separation bubble dynamics. The performance parameter (frequency-deflection-pressure ratio) improves by 43% for ARribs = 1.56 compared to the smooth Coanda surface oscillator. Then the influence of number of ribs (1–6) on Coanda-surface-driven jet oscillations is investigated. The highest frequency (875 Hz) occurs with 4 ribs, a 146% increase over the smooth case (355 Hz). While ribs reduce deflection angles (53.3° to 37.1° for 4 ribs), they also lower pressure drop by modifying separation bubble dynamics. The performance parameter (frequency-deflection-pressure ratio) improves by 87.7% for the 4-rib configuration compared to the smooth oscillator.

Finally, CFD-based Taguchi-Grey relational analysis is used to optimize Coanda-surface rib design, considering three factors: aspect ratio (0.64, 1.00, 1.56), number of ribs (4, 6, 8), and rib angle (-18.5°, 0°, +18.5°). Using an L9 orthogonal array and weighted Grey Relational Analysis (AHP-supported), multi-objective optimization and ANOVA were performed. Results show number of ribs dominates oscillation frequency, rib angle most affects jet deflection, and aspect ratio significantly reduces pressure drop. The optimized design improves frequency by 19.9%, deflection angle by 39.7%, and reduces pressure drop by 17.6%. This integrated approach demonstrates effective multi-objective optimization for fluidic oscillators, offering insights for future performance enhancements. For thermal performance evaluation, four factors: oscillator design group, Reynolds number, jet-to-target distance, and target surface length, were analyzed using a 2D CFD model and an L9 orthogonal array. Thermal analysis demonstrated a 24.3% enhancement in Nusselt number (Nu) over the smooth oscillator, with a performance evaluation criterion (PEC) of 1.252 for the optimized design. These findings underscore the significant potential of fluidic oscillators in improving both flow dynamics and heat transfer efficiency.

Keywords: Fluidic oscillator, Sweeping jet impingement, Heat transfer, Fluid flow, Optimization, Taguchi method

Contents

List of Figures

List of Tables

Abbreviations

AHP	Analytical Hierarchy Process
AR	Aspect Ratio
BR	Blowing Ratio
CFD	Computational Fluid Dynamics
CI	Consistency Index
CR	Consistency Ratio
DOE	Design of Experiment
ER	Expansion Ratio
FDPR	Frequency Jet Deflection-Pressure Ratio
FFT	Fast Fourier Transform
Ff	Dimensionless Pressure Drop
FPR	Frequency-Pressure Ratio
FVR	Peak Velocity Ratio
GA	Genetic Algorithm
GM	Geometric Mean
GRA	Grey Relational Analysis
H/D	Jet to Target Surface Distance
JDPR	Jet Deflection-Pressure Ratio
L/D	Target Surface Length
RANS	Reynolds-Averaged Navier–Stokes
RI	Random Index
RSM	Response Surface Methodology
S/N	Signal-to-Noise Ratio
SST	Shear Stress Transport

SWJ	Sweeping Jet
URANS	Unsteady Reynolds-Averaged Navier–Stokes
WGRA	Weighted Grey Relational Analysis

Symbols

M	Mach number
f	Oscillation frequency
St	Strouhal number
Nu	Nusselt number
Re	Reynolds number
D	Exit nozzle throat diameter
AR_{ribs}	Aspect ratio of ribs
R_h	Height of rib
R_b	Width (base) of rib
Tu	Turbulent intensity
k	Turbulent kinetic energy
ω	Specific dissipation rate
μ_t	Turbulent viscosity
a_1	Model constant (value = 0.31)
F_2	Blending function in SST model
V_{exit}	Time-averaged exit velocity of the jet
V_i	Inlet velocity
V_{peak}	Peak jet velocity at the oscillator exit
Δp	Pressure drop across the oscillator
S_2	Nozzle spacing between inlet and exit
Δp_s	Pressure drop of the smooth case
Δp_e	Pressure drop of the enhanced case
f_s	Frequency in the smooth case

f_e	Frequency in the enhanced case
θ	Jet deflection angle
θ_s	Deflection angle of smooth case
θ_e	Deflection angle of enhanced case
q	Heat flux
T_s	Target surface temperature
T_{ref}	Reference temperature
λ	Thermal conductivity
c_p	Specific heat at constant pressure
ρ	Fluid density
u_i, u_j	Velocity components
τ_{ij}	Stress tensor
S_{ij}	Mean rate of strain tensor
δ	Jet half-width
x	Axial distance from oscillator exit
T	Temperature
y_i	i^{th} observed objective value
n	Number of observations in a trial
$\bar{y}$	Mean of the performance characteristic
s^2	Variance of the performance characteristic
x_{ij}	Initial value of criterion j for alternative i
x'_{ij}	Normalized value of criterion j for alternative i
$x_j^{\min}$	Minimum value of criterion j
$x_j^{\max}$	Maximum value of criterion j
Δ_{ij}	Absolute difference between normalized value and reference
$\Delta_{\min}$	Minimum Δ_{ij} across all alternatives
$\Delta_{\max}$	Maximum Δ_{ij} across all alternatives
ξ_{ij}	Grey Relational Coefficient for alternative i, criterion j
ξ_{ij}^w	Weighted Grey Relational Coefficient
w_j	Weight of criterion j
G_i	Grey Relational Grade for alternative i

A	Pairwise comparison matrix in AHP
a_{ij}	Comparative value between responses i and j
GMi	Geometric mean of row i in AHP matrix
w_j	Normalized weight of criterion j
$\lambda_{\max}$	Maximum eigenvalue of the AHP matrix

Chapter 1

Introduction

1.1 Background

Th progress in high-performance thermal engineering applications stimulated the demand for thermal-hydraulic performance enhancement of heat exchange systems. Different passive and active cooling methods have been used in the past to achieve the goal of attaining high heat transfer rates without increasing hydraulic losses. The passive cooling methods do not require any external energy source for cooling. The heat transfer rates are achieved through conduction, radiation, and convection processes as used by Grubišić-Čabo et al. [1] and Xu et al. [2]. Whereas in the active control methods external energy source is required for heat removal as utilized by Zhou et al. [3] and Hackenhaar et al. [4] during their studies. Thermal applications requiring high heat transfer rates utilize active cooling methods despite their use of external energy. In the active cooling methods, the method of jet impingement gives high heat transfer performance and finds its role in various engineering applications, which includes cooling of electronic devices [5, 6], gas turbine blades [7, 8], solar systems [9, 10], use in aerospace technology [11, 12], drying of paper [13], ink drying [14] and heat treatment of steel [15]. Many researchers have studied the fluid and thermal characteristics of impinging jets to attain enhanced thermal performance [16–19]. Thermal and hydraulic performances of jet impingement have been extensively reviewed by [20–25] for jet impingement.

It is important to understand the flow characteristics of impinging jets and their impact on heat transfer. The fluid flow characteristics strongly affect the heat transfer phenomenon in jet impingement. The flow structure of a single jet can be divided into three distinct regions: (a) free jet region, (b) stagnation region, and (c) wall jet region (see Fig. 1.1).

The free jet region starts from the nozzle and is far away from the target surface, thus acting as a free jet. The entrainment of mass, momentum, and energy takes place due to the shear-driven interaction of the jet periphery and surroundings in this region.

The free jet can be subdivided into (i) a potential core, (ii) a developing zone, and (iii) a fully developed zone (see Fig. 1.1). In the potential core zone, the jet average velocity is equal to the nozzle exit velocity.

The jet core region length is measured from a point from the nozzle inlet to the point where the jet average velocity is around 95% of the nozzle exit velocity. The jet velocity decreases rapidly after the potential core, as presented by Jambunathan et al. [20].

This makes the jet plate/nozzle–target surface spacing an important parameter that affects the rate of heat transfer. After the potential core, the developing region exists where the decay of the axial velocity profile occurs due to large shear stresses at the jet periphery.

Subsequently, the effects of shear stresses start to penetrate inside the core of the jet. A fully developed profile is obtained after the shear effects reach the core of the jet. In the fully developed region, at the centerline of the jet, the axial velocity component is the maximum and the radial velocity component the minimum . The region where the jet strikes the target surface is termed the “stagnation region.” In the stagnation region, static pressure rises due to diminishing axial velocity.

The region hereafter is called the wall jet region, where bulk fluid is directed radially outward. It is pertinent to mention that the maximum heat transfer takes place at the stagnation point (with the exception of a small separation distance) and a reduction in heat transfer rates occurs radially. The heat transfer between the impinging jet and the target surface can be affected by various factors, such as nozzle geometry, velocity profile, jet exit velocity, jet and target surface spacing, and turbulence level.

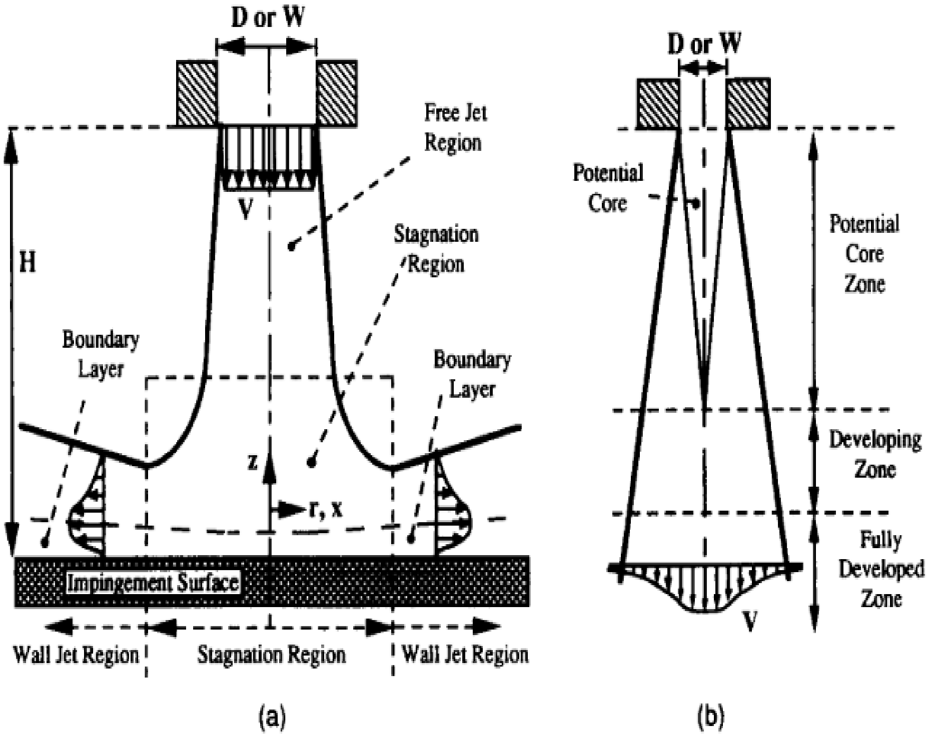

FIGURE 1.1: (a) Flow regions of the impinging jet and (b) main flow zones of the free jet (Reprinted with permission from ref. [26] - Elsevier)

1.2 Jet Excitation

The quest for further improving the heat transfer performance of jet impingement cooling on a target surface made way for jet excitation using passive and active excited jets as shown in Fig. 1.2.

These excited jets have considerable implications for thermal system performance by improving jet turbulence and mixing characteristics.

These excited jets have the potential to intensify impingement over a larger area of the target surface as compared to steady jets [27].

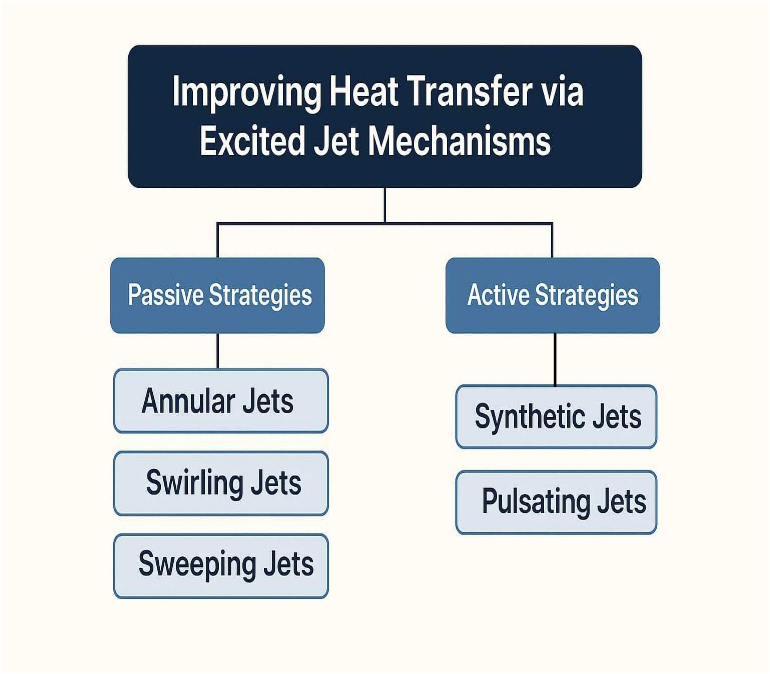

FIGURE 1.2: Jet Excitation Methods

The heat transfer enhancement through jet excitation is achieved through passive and active jet excitement methods. Exciting the turbulent jets through both passive and active methods has received considerable attention recently from researchers due to their significant role in the improvement of jet turbulence using jet impingement in thermal systems. Various experimental and numerical studies are available in the literature, that consider passive [28, 29] and active jet excitation [30, 31] for the investigation of thermal and hydraulic characteristics.

1.3 Active Exciting Jets

Active exciting jets as presented in Fig. 1.2 are used in various engineering applications to improve fluid mixing and thereby enhance heat transfer performance. These jets require an external energy source and often include moving parts for the purpose of excitation. Two primary types of active jets are employed: synthetic jets [32–36] and pulsating jets [37–39]. Synthetic jets are formed by the periodic ejection and suction of fluid through an orifice without net mass injection, while pulsating jets involve controlled flow oscillations with or without flow interruption.

Excitation of these jets is typically achieved through mechanical means, such as vibrating diaphragms or pistons [40], or through acoustic methods where pressure waves are used to induce oscillations in the jet stream [41]. These methods lead to enhanced turbulence and improved heat transfer rates by periodically disturbing the boundary layer near the impinged surface.

Although active excitation techniques are highly effective, particularly in small-scale thermal systems like electronic cooling or microchannel devices, their applicability in large-scale systems is limited. This limitation arises due to the increased power consumption, complexity of moving components, and maintenance challenges associated with such systems.

1.4 Passive Exciting Jets

Passive jet excitation methods as shown in Fig. 1.2 provide a more robust and maintenance-free approach for heat transfer enhancement, as they do not involve any moving mechanical parts. These methods utilize inherent flow instabilities and geometric features to induce jet excitation. Common passive techniques include swirling jets, annular jets, and sweeping jets. These jets enhance heat transfer by increasing turbulence intensity and promoting better fluid mixing near the target surface. Swirling jets are produced by imparting angular momentum to the jet stream using helical vanes or twisted nozzles [42–47], which create a rotational flow pattern that improves the convection mechanism.

Annular jets, on the other hand, involve a ring-shaped jet flow and are typically employed in applications requiring uniform cooling across a circular area [48–52]. The advantage of passive techniques lies in their simplicity and durability, as they do not depend on external power sources or mechanical excitation mechanisms. These systems are particularly advantageous in harsh environments or in large-scale industrial applications where reliability and low maintenance are critical.

Given their unique self-sustaining oscillation and broad cooling coverage, sweeping jets are the primary focus of this study.

1.5 Sweeping Jets

Among the passive techniques, sweeping jets represent a special category of passive self-exciting jets, characterized by high-frequency spatial oscillations of the jet stream. This oscillation is induced without moving mechanical parts, utilizing the natural instability mechanisms within specially designed devices known as fluidic oscillators. These devices exploit the Coanda effect and pressure feedback loops to produce a periodic jet deflection from a steady inlet flow. The fundamental mechanism behind sweeping jet formation relies on intrinsic instabilities within the flow, which are amplified in the mixing chamber of the oscillator. The alternating attachment of the flow to the oscillator walls, aided by pressure feedback channels, creates a self-sustained oscillating jet. This jet, upon impingement on a surface, induces strong turbulent mixing and promotes high convective heat transfer rates. Compared to steady jets, sweeping jets cover a larger surface area due to their lateral movement, leading to better thermal uniformity and reduced hot spots. These jets are particularly effective in cooling applications such as electronic devices, gas turbine blades, and solar thermal systems. Design variations such as single or double feedback loops in the fluidic oscillator significantly influence the oscillation frequency, deflection angle, and ultimately the thermal performance. Among these, double feedback fluidic oscillators are most commonly used due to their ability to sustain stable high-frequency oscillations and their adaptability to various geometrical configurations. Overall, sweeping jet impingement is a promising technique for achieving superior thermal-hydraulic performance in both small and large-scale applications.

1.6 Importance of Sweeping Jets

An unsteady oscillating jet formed by a fluidic oscillator possesses many opportunities for flow control [53, 54], acoustic control [55], separation control [56–58], enhancement of flow mixing [59], flow measurement [60], and increase in the rate of removal of heat from hot surfaces [61]. The oscillating jets can sustain high heat transfer rates while covering a significantly broader target surface area.

Additionally, sweeping jet impingement setups have the potential to adopt design improvements and their fluidic oscillators can be altered more than the other types of jet impingement setups. According to the literature review, double feedback oscillators were used more frequently than zero feedback or single feedback oscillators for sweeping jet impingement. The main reason behind their frequent use is the capacity to adopt design changes. Therefore, this research is focused on double feedback oscillators used in impinging sweeping jets.

1.7 Problem Statement

Hot surfaces in high-temperature thermal applications pose a persistent challenge to achieving efficient and reliable system performance. Excessive surface temperatures can significantly degrade efficiency, structural integrity, and operational lifespan, making effective cooling a critical requirement. Conventional convective cooling techniques often fall short in high heat flux environments due to their limited heat removal capability.

Jet impingement cooling has therefore emerged as a practical alternative for such applications. Among the available jet impingement approaches, sweeping jet impingement offers improved surface coverage and more uniform heat transfer compared to steady jets.

However, the effectiveness of sweeping jet cooling is strongly dependent on the geometric design of the fluidic oscillator, and a clear understanding of how oscillator geometry influences flow behavior and heat transfer performance remains limited. This lack of comprehensive insight into the relationship between fluidic oscillator design parameters and thermal performance represents a key research problem. Addressing this gap is essential for developing efficient cooling solutions for high heat flux systems such as gas turbines, electronic devices, and industrial thermal equipment.

1.8 Research Objective

The primary objective of this research is to design and optimize a double feedback fluidic oscillator capable of enhancing heat transfer rates and ensuring uniform cooling when an oscillating jet impinges on a high-temperature target surface. To achieve this goal, the following specific objectives are outlined:

i. Investigate the influence of ribbed Coanda surface on the flow behavior of the jet formed by the fluidic oscillator.

ii. Conduct numerical study to evaluate the performance of the ribbed fluidic oscillator configuration in terms of oscillation frequency, jet deflection angle and pressure drop characteristics.

iii. Employ the Taguchi optimization method to systematically determine the optimal geometry of the ribbed fluidic oscillator for maximizing its flow performance.

iv. Quantify the thermal performance enhancement achieved by the optimized ribbed fluidic oscillator when applied to a heated surface in sweeping jet impingement system.

This study aims to contribute to the advancement of active cooling techniques by developing an efficient fluidic oscillator design suitable for high temperature applications, such as gas turbine blade cooling, electronics thermal management, and industrial heat exchangers.

1.9 Scope of Study

This study employs a numerical approach to investigate the flow and thermal performance of a novel fluidic oscillator designed for sweeping jet impingement cooling. CFD simulations were conducted to analyze the oscillator's behavior under varying geometric and flow conditions. The study focuses on design and parametric analysis of a fluidic oscillator with ribbed Coanda surface to enhance oscillation characteristics and flow control. The flow performance was evaluated based on key performance parameters, including oscillation frequency, jet deflection angle and pressure drop. For thermal performance the heat transfer on a heated surface was enhanced in sweeping jet impingement system.

The working fluid (air) was maintained at ambient temperature (25°C), while the target surface was heated to 400°C, representing typical heated surface applications. Key geometric parameters, including jet to target distance, target surface length and Re, were systematically varied to optimize thermal performance.

Computational constraints necessitated the use of steady-state RANS models rather than more accurate but resource-intensive transient or LES approaches. Only single-phase air flow was considered, excluding multiphase flows or phase-change effects that might occur in practical cooling applications.

The findings provide theoretical and computational insights into optimizing fluidic oscillators for high temperature applications, such as cooling of electronics systems and gas turbine blade cooling.

1.10 Thesis Structure

This dissertation consists of eight chapters, with the primary objective of developing innovative solutions for designing an enhanced double-feedback fluidic oscillator capable of superior flow performance and heat transfer augmentation. The chapter organization is as follows:

Chapter 1 introduces thermal management techniques, categorizing cooling methods into active and passive approaches. Focusing on active cooling, the discussion emphasizes jet impingement techniques, particularly sweeping jet excitation and its significance in thermal applications. This chapter also presents the research motivation, clearly defined objectives, and the study's scope.

Chapter 2 presents a comprehensive review of existing research on double-feedback fluidic oscillators, focusing on their application in flow control and heat transfer enhancement. The review systematically examines previous studies, analyzing their methodologies, key findings, and limitations. Through critical evaluation of the literature, specific research gaps are identified, particularly in oscillator design optimization and thermal performance characteristics.

Chapter 3 outlines the numerical framework developed for the computational analysis of the double feedback fluidic oscillator. The foundation is established through a rigorous presentation of the governing equations, including the continuity, momentum and energy equation. The numerical model is developed by carefully defining the computational domain, boundary conditions and discretization schemes.

The chapter includes a comprehensive validation procedure, where mesh independence studies are conducted and numerical results are compared against benchmark cases to establish confidence in the simulation methodology. The validated numerical approach provides the basis for the parametric studies and performance evaluations presented in subsequent chapters.

Chapter 4 investigates the influence of Coanda surface modification on the performance of a double feedback fluidic oscillator. Rectangular ribs with varying aspect ratios are introduced to the Coanda surface, and their effects on jet characteristics are evaluated through two-dimensional unsteady numerical simulations. The chapter outlines the numerical setup, including the variation of rib geometry, and analyzes the resulting changes in jet oscillation frequency, deflection angle, and pressure drop. A performance metric combining these parameters is used to assess the overall effectiveness of the ribbed designs.

Chapter 5 explores the effect of varying the number of rectangular ribs on the Coanda surface of a double feedback fluidic oscillator. Building on the findings from the previous chapter, this study aims to enhance the flow performance by systematically analyzing how the number of ribs influences key jet characteristics. The chapter presents the numerical methodology used to simulate different rib configurations and examines their impact on jet oscillation behavior, including frequency, deflection angle, and pressure drop. A performance evaluation metric is employed to identify the optimal rib configuration.

Chapter 6 presents an optimization study of the double feedback fluidic oscillator by modifying the Coanda surface geometry. The aim is to improve flow performance by simultaneously analyzing the effects of multiple geometric parameters, including aspect ratio, number of ribs, and rib angle.

Using the Taguchi-GRA optimization method, the study identifies optimal parameter combinations that enhance jet oscillation frequency and deflection angle. This chapter consolidates the geometric design insights developed in earlier chapters into a unified optimization framework for flow performance enhancement.

Chapter 7 focuses on evaluating and enhancing the thermal characteristics of the optimized double feedback fluidic oscillator configurations. The study extends the flow analysis by incorporating thermal performance evaluation under different operational and geometric conditions. A two-dimensional CFD model is employed along with an L9(3^3) orthogonal array based on the Taguchi method. Four factors, oscillator design, Reynolds number, jet-to-target distance, and target surface length are varied to investigate their influence on thermal performance. The outcomes of this chapter provide a comprehensive assessment of the heat transfer capability of optimized oscillator configurations and validate their effectiveness in practical thermal applications.

Chapter 8 summarizes the key findings and contributions of the research. It highlights the improvements in jet oscillation behavior and thermal performance achieved through systematic geometric modification and optimization of the Coanda surface in a double feedback fluidic oscillator. The chapter concludes by reflecting on the overall impact of the study on flow and thermal control strategies in fluidic devices. It also outlines potential future directions, including three-dimensional modeling, experimental validation, and exploration of additional passive or active control methods for further performance enhancement.

Chapter 2

Literature Review

A detailed literature study was performed to study the recent advancements and the assessment of fluid flow and heat transfer performance of fluidic oscillators used in sweeping jet impingement. The literature review is focused on presenting state-of-the-art research progress on self-exciting fluidic oscillator design, jet flow, impingement, and heat transfer characteristics. The main focus is to report literature about double feedback fluidic oscillators which are mainly in use due to their higher efficiency. The recent geometric design advancements of double feedback fluidic oscillators for enhancement of jet flow control and the augmentation in associated thermal-hydraulic characteristics of the jet impingement are discussed in detail. The performance of jet impingement heat transfer in single-phase flows is reviewed. The important geometrical parameters and their role in the performance enhancement of double feedback fluidic oscillators are reported.

2.1 Advancements in Fluidic Oscillator Designs for Flow Control

The prime operating mechanism of a fluidic oscillator consists of inherent self-sustained instabilities which leads to an oscillating behavior of the jet. The frequency of the oscillating jet is mainly dependent upon the particular geometry of the oscillator and the flow rate through it [62]. Fluidic oscillators are broadly categorized into wall attachment and jet interaction types [63]. Wall attachment oscillators use feedback loops and are divided into single [64] and double feedback [65] designs. Single feedback oscillators utilize a single feedback loop, where fluid is redirected through one pathway to induce jet oscillation, while double feedback oscillators employ two separate and distinct feedback pathways to achieve the oscillatory flow. Jet interaction oscillators, or zero feedback designs, operate without external feedback loops, relying instead on mechanisms like jet collisions and vortical patterns, as seen in Raghu's [66] patent design. For a detailed classification of oscillators, Tesar [67] provides a comprehensive framework based on feedback principles, working modes, and the number of amplifiers.

The double feedback oscillator has become more popular in the recent past due to its high efficiency and more leverage for further design enhancements as per the requirement of the particular application. The double feedback oscillator design originated from the patent of Stouffer [68]. The mechanism of a double feedback oscillator is that fluid enters through the supply nozzle and from there it moves inside the mixing chamber (interaction region). In the mixing chamber, due to instability in the flow, it is attached to either wall through the Coanda effect as presented in Fig. 2.1(a). The fluid enters the feedback channel and rejoins the flow in the interaction region but flips over to the other side and repeats the same phenomenon thus producing oscillating flow at the exit of the fluidic oscillator and generating a self-sustaining oscillation jet as shown in Fig. 2.1(b).

The double feedback oscillator is used in sweeping jet impingement for applications such as turbine blade cooling. Improving the frequency, the jet spread angle and the pressure drop across the oscillator (between the inlet and exit throat) plays a critical role in effective hydraulic and thermal performance. A higher frequency and wider jet spread angle enhance heat transfer performance, while a minimized pressure drop ensures energy-efficient operation, both of which are essential for effective turbine blade cooling.

The intrinsic geometrical characteristics of the oscillator are designed to figure out

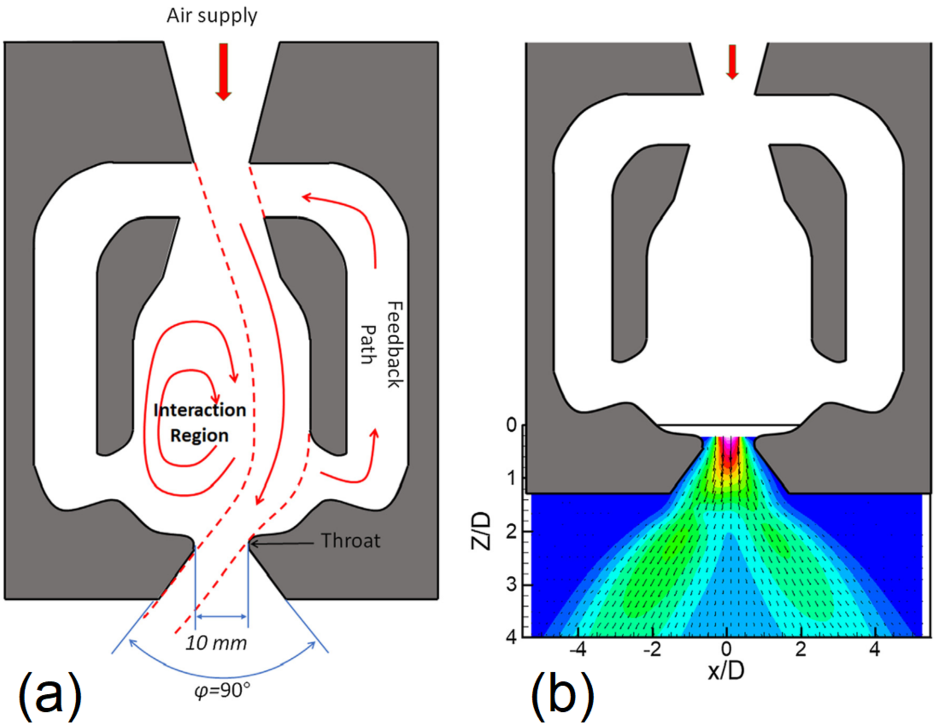

FIGURE 2.1: Fluidic Oscillator with double feedback channel (a) schematic (b) mean velocity distribution [69] (Reprinted - Courtesy Elsevier)

these vital parameters. The geometric configuration of the fluidic oscillator plays an important role in augmenting the flow characteristics of the oscillating jet. In this regard, the geometric parameters including length, volume, inlet wedges of mixing chamber, inlet, and outlet regions of feedback channel were explored by Bobusch et al.[70].

Sang et al. [71] performed a numerical investigation to study the impact of nozzle power and throat width on the characterization of various internal flow characteristics. The important design parameters of the fluid oscillator have been presented in Fig. 2.2(a). It was also observed the operation of the oscillator was strongly dependent on the throat width. It was reported that if the width of the outlet of the power nozzle is significantly smaller than the width of the inlet of the mixing chamber, the time between each fluid flip within the oscillator increased as the width of the throat decreased. An experimental parametric study was performed by Koklu [72] during which the placement of the oscillator (spread angle, pitch, and stream-wise position) and oscillator size were investigated to obtain flow separation control. The investigation of fluidic oscillator's geometric configurations such as widths and wall's angles of inclination of both inlet and outlet of mixing chamber, as shown in Fig. 2.2(b), on the output characteristics of the sweeping jet were performed by Baghaei and Bergada [73].

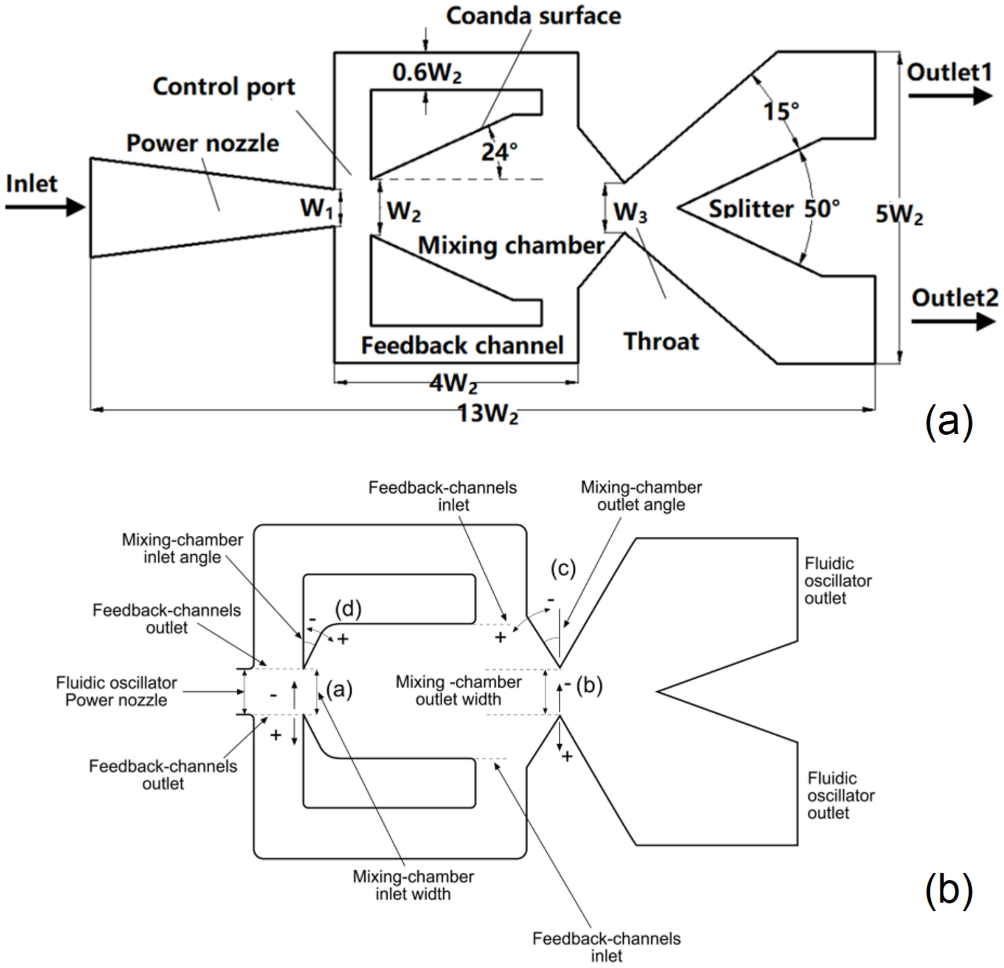

FIGURE 2.2: Different geometric parameters of a fluidic oscillator (a) Sang et al. [71] (b) Baghaei and Bergada [73] (Reprinted - Courtesy MDPI open access)

A reverse flow within and at the outlets of feedback channels was found for the smaller inlet width of the nozzle due to the production of large pressure waves hence generating a large fluctuation in fluid mass flow rate as compared to the larger inlet width of the nozzle. The larger nozzle width generates low stagnation pressure and a small sweeping jet region. In another study, Bergada et al. [74] investigated the influence of feedback channel geometry on the amplitude and frequency of fluidic oscillator flow at the outlet. As the feedback channel length grows, the frequency of the exit mass flow oscillation decreases.

Over lengthy feedback channel lengths, the former main oscillation tends to disappear, leaving the jet inside the mixing chamber to just oscillate at high frequencies. An experimental and numerical study was performed by Abdulnaim et al. [75] which determines the effects of the fluidic oscillator's exit geometry on the flow characteristics inside and outside of the device. The findings show that the absence of the splitter causes an increase in the deflection angle and a trend for continuous outflowing jets. The splitter increases the outflow fluctuation amplitudes, which makes them perfect for a range of applications. Various fluidic oscillator designs have also been reviewed by Abdelmaksoud and Wang [63].

Recently, several design modifications of fluidic oscillators have been proposed in the literature to enhance flow control and impingement characteristics of sweeping jets. In this regard, Ostermann et al. [76] performed a comparative flow field analysis of curved and angled fluidic oscillators experimentally as shown in Fig. 2.3.

It was revealed through flow fields and pressure measurement that similar oscillation mechanisms and frequencies were incorporated by both designs. The internal dynamics was not observed to be changed for curved oscillator as for angled oscillator. Reverse flow in the feedback channel, present in the angled oscillator, was prevented in the curved oscillator due to the large spacing between the inlet wedges of the mixing chamber. 20% reduced supply pressure was required for curved oscillators which makes them more effective in terms of energy requirement as compared to the angled oscillator. A different oscillation pattern and higher maximum deflection angle were caused in external flow fields for curved oscillators due to the attachment of its jet to the walls of the diverging part of the outlet nozzle.

A numerical investigation was performed by Nilli-Ahmadabadi et al. [77] to study the performance of a new vortex-based fluidic oscillator using URANS, as illustrated in Fig. 2.4. Two chambers, primary and secondary with a mid-throat separation

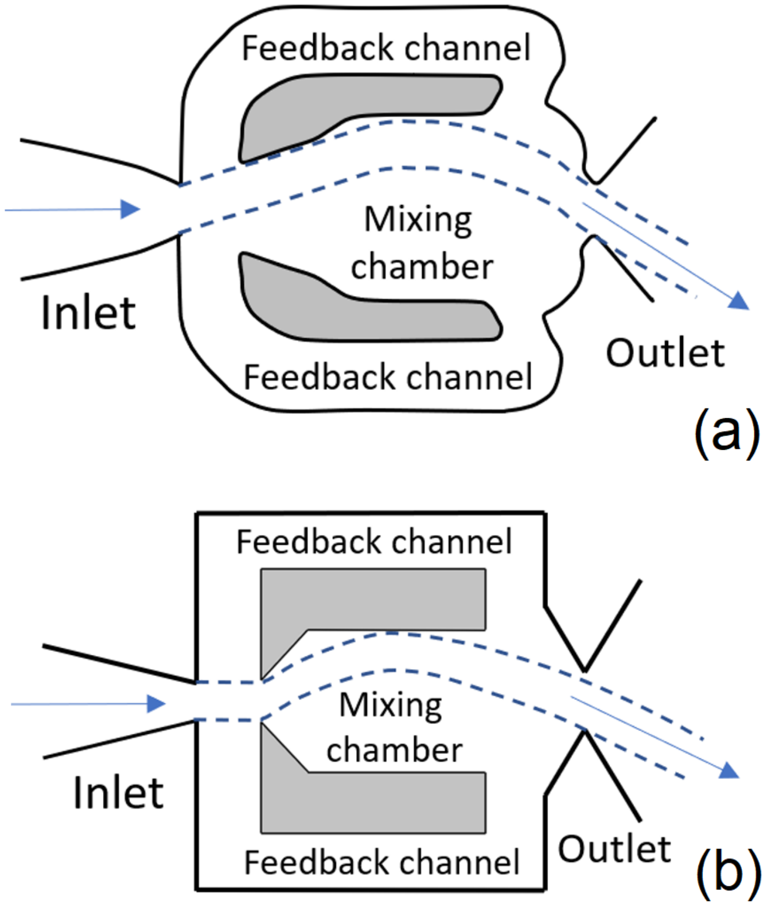

FIGURE 2.3: Double feedback fluidic oscillators (a) curved, (b) angled (Adapted from [76])

and bi feedback channels were part of the oscillator. Double pair vortices were generated inside these chambers by the main jet.

Asymmetric growth and shrinkage were experienced by these vortices and feedback flow was activated which resulted in harmonic oscillation as seen in Fig. 2.4. A portion of the jet shear layer was trapped inside the primary chamber due to the colliding oscillatory jet with mid-throat, which resulted in a strong vortex that turned the jet to the opposite side. The secondary chamber vortex forced the attachment of the jet to a single side of the secondary chamber, which caused the deviation of the outlet jet to the opposite side. The newly designed fluidic oscillator produced increased oscillation frequency and output momentum flux and decreased pressure drop. A numerical and experimental study was performed by Tomac and Sundstrom [78] for the introduction of a fluidic oscillator design that could give the advantage of sweep and inclination angle control irrespective of supply flow rate. To achieve this, fluid was injected through four control ports present in the vicinity of the fluidic oscillator's throat. Based on the quantity of control flow, it was observed from the results that a variation of 17° to 70° of sweep angle and up to 20° variation in inclination angle was achieved. With an increase in control flow rate, up to 5% and a 7.7% decrease in oscillation frequencies were noted for variable sweep angle and variable inclination angle design respectively.

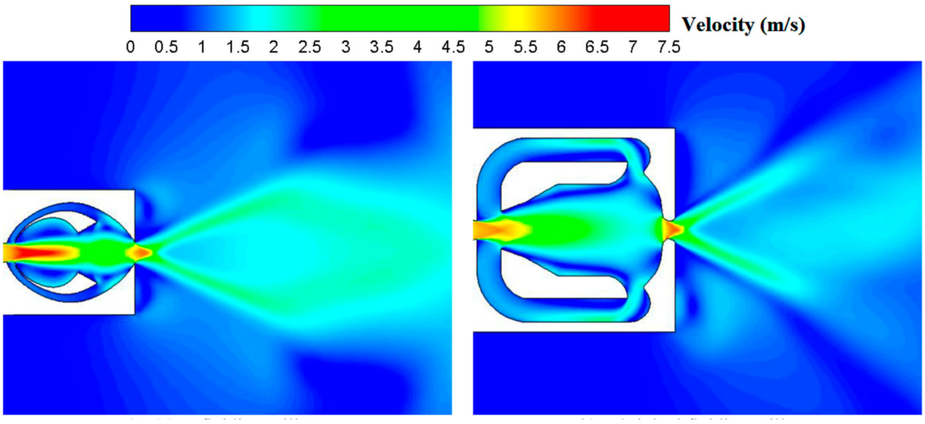

Figure 2.4: Comparison of time-averaged velocity contours of new vortex-based oscillator and original oscillator at Re = 60,000 [77] (Reprinted – Courtesy Taylor and Francis open access)

A numerical study was performed by Kim and Kim [79] to investigate the impact of bending angle ranging between 0–40° of bent outlet nozzle on characteristics of the fluidic oscillator with the external flow and without it. For the evaluation of the performance of the fluidic oscillator, two performance parameters were presented peak velocity ratio and dimensionless pressure drop. The enhancement in peak velocity of the exiting jet from the oscillator is influenced by the peak velocity ratio. The velocity ratio is generally used in fluidic oscillators for separation control applications. Dimensionless pressure drop was the second performance parameter that also affected pumping power directly. The necessary pumping power for driving the fluid flow through the oscillator is directly affected by pressure drop. It was observed from the results that during the study peak velocity ratio showed an increasing trend with an increase in mass flow rate but for the reference model it first increased up to lower bending angles then increased.

It is generally assumed that the effectiveness of the oscillator is enhanced due to an increase in peak velocity ratio which results in imparting more momentum to jet flow. The pressure drop increased almost uniformly with a bending angle at all ranges of mass flow rates. This increase in pressure dropped increased by pumping power.

At a high mass flow rate, bending angle caused the increase in jet frequency but jet oscillation vanished at the bending angle of 40°. Mohammadshahi et al. [80] performed an experimental study of flow dynamics of jets originating from a double feedback fluidic oscillator in confined and non-confined geometry. The experiments were conducted for a range of Reynolds numbers from 2500 to 10,000. The expanded region aspect ratio (AR) and expansion ratio (ER) effects were also investigated.

The oscillation frequency was found to be rather insensitive to the external domain and almost constant for AR and ER. A much larger spreading angle of the fluidic oscillator was recorded with an increasing Reynolds number.

Tajik et al. [81] performed an experimental investigation of the role of the geometric variations of the fluidic oscillator, including feedback channel width (D1), outlet diameter (D2), and the Coanda surface structure (Si) in the performance enhancement of sweeping jet. Fig. 2.5 depicts the general behavior characterization of the jet flow for all geometrical variations of fluidic oscillators used during the study. Bifurcated and homogenous velocity profiles were the two main distinguishable flow behaviors recorded and produced by geometric alterations.

The bifurcated velocity profile resembled the velocity profile of the canonical curved oscillator and the homogeneous velocity profile was similar to the angled oscillator. The modifications in the shape of the Coanda surface of the curved fluidic oscillator resulted in jet flow profiles resembling that of the angled fluidic oscillator. In the diffuser section, the spread angles of the jet along with the fluctuations in static pressure were found to be the direct functions of supply pressure hence the flow performance parameters such as pressure drop in the oscillator are directly related to the external flow regime. The weak influence of flow regime was observed over

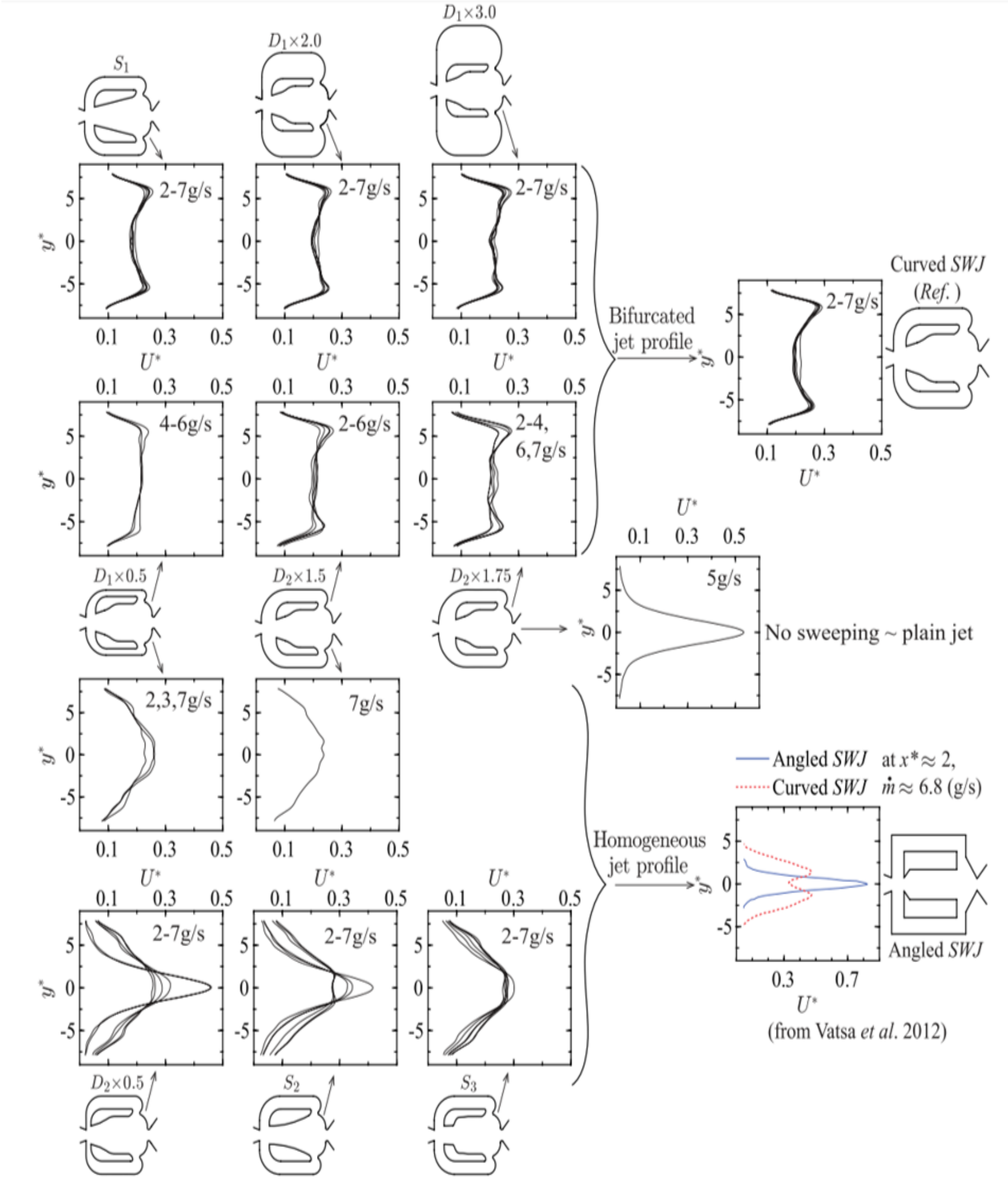

Figure 2.5: Flow regimes characterization for all variations in fluidic oscillators [81] (Reprinted - Courtesy Springer open access)

sweeping frequency, however, bifurcated velocity profile produced lower sweeping frequency as compared to homogeneous velocity profile of jet.

The experimental and numerical study of Zhou et al. [82] investigated the spatial and temporal distributions of nitrogen gas injected from a typical and compact fluid oscillator at the back of the 777-shaped hole for blowing ratio (BR) variations of 1.0 to 3.0. The compact fluidic oscillator outperformed the typical oscillator providing much wider impingement area coverage but at the cost of a reduction in

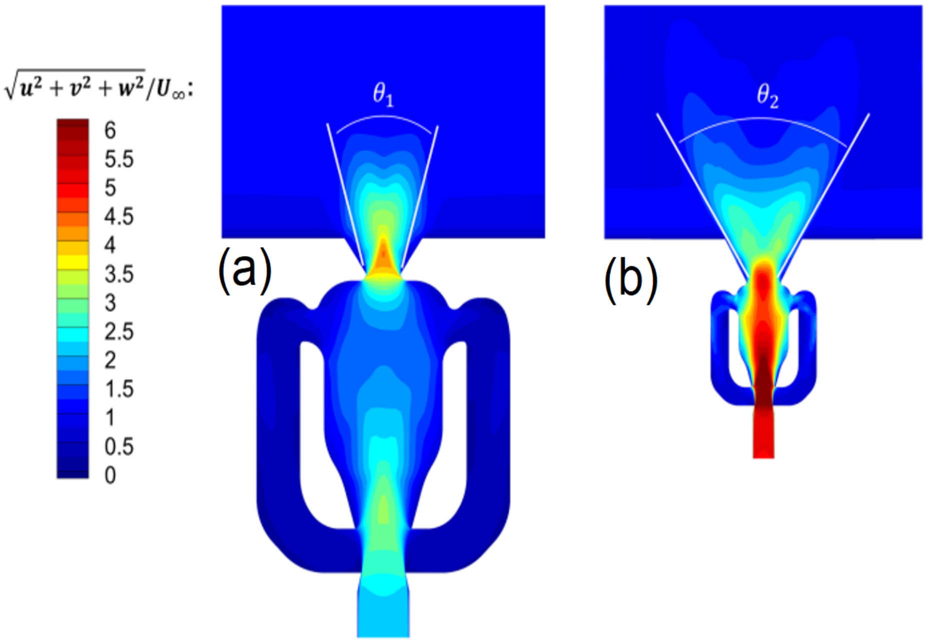

Figure 2.6: Schematic of the (a) typical sweeping jet, (b) compact sweeping [82] (Reprinted – Courtesy American Institute of Physics)

flow coherence. The compact sweeping jet showed lower jet momentum at the exit but produced more uniform jet-surface interaction, thus manifesting its enhanced effectiveness as observed in Fig. 2.6(a, b).

A numerical study was performed by Oz and Kara [83] to understand the flow dynamics of the sweeping jet fluidic oscillator at the throat and various downstream locations of the oscillator. The results of the non-dimensionalized (by throat velocity) mean velocity profile were compared at the throat and 3 different downstream locations for various flow rates as presented in Fig. 2.7(a-d). At location x/h = 1 double peak started appearing at mass flow rate 4.5359 g/s and above. It can also be observed from the results that peak velocities showed an increasing trend with an increase in flow rate. However, the peak velocity remained almost the same at all downstream locations for a certain flow rate value. The jet oscillations were found to increase linearly with increasing Mach number as observed in Fig. 2.7(e). The relationship of the oscillation frequency of the jet as a function of subsonic nozzle exit Mach number is obtained to be linear i.e. f = 511.22 M + 46.618 for 0<M<1.

The oscillation frequency is dependent on two parameters: (i) the size of the fluidic oscillator and (ii) the velocity of flow. The oscillation frequency can be compared through the calculation of the Strouhal number. In the study the size of the oscillator was fixed so the flow velocity was important. For experimental data, the oscillation frequency of the jet was found by calculating the differences in velocity between symmetrical two points at the center of leaving jet. The frequency was then obtained through a low pass filter and FFT (Fast Fourier transform) analysis on velocity difference earlier calculated.

It was shown by the results that oscillation frequency had no dependency on both mass flow rate and the type of working fluid. Reynolds number increase produced strong vortices and caused the increase in oscillation frequency. An average Strouhal number of 0.0131 is found which remains almost constant for different Mach numbers as observed in Fig. 2.7(f).

Flow control in large-scale applications was explored by Aram et al. [84] by exploring the unsteady behavior of sweeping jets produced by fluidic oscillators during their numerical investigation. It was observed from the results of actual and scaled-up oscillators that the Reynolds number based on the jet outlet diameter was the appropriate quantity for the scale-up of fluidic oscillators. The results showed that a pair of streamwise counter-rotating vortices were formed which grew in size and strength with an increase in jet velocity and the penetration of the jet was recorded to be greater in normal and sideways directions at high jet velocities. Alam and Kara [85] numerically investigated the effect of nozzle exit geometry over the heat transfer performance of sweeping jets impinging on a target surface. The geometric changes in nozzle exit geometry showed no impact on the oscillation frequency. A lower downstream velocity was reported with the increase in nozzle exit width. The distributions of velocity and pressure in the flow field were also discovered to be influenced by changes in nozzle exit geometry. The Modal analysis technique is employed by Song et al. [86] to study the oscillation mechanisms and spatial-temporal flow structures of novel double feedback fluidic oscillator designs. They reported that geometrical parameters, including inlet-wedge width and feedback-channel inlet diameter, were found to significantly influence flow

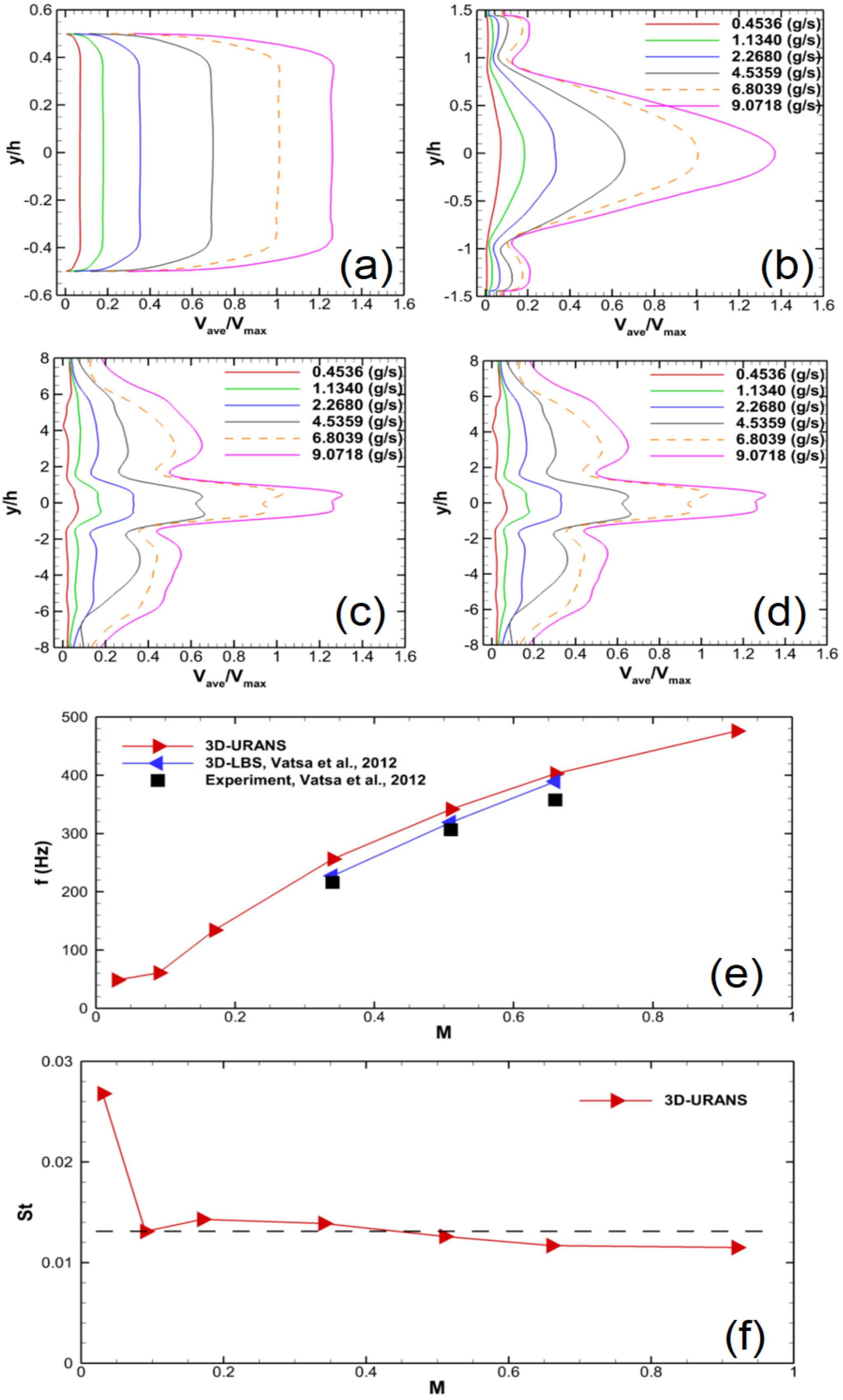

FIGURE 2.7: Velocity profiles at various downstream locations of sweeping jet oscillator (a) throat (b) x/h=0 (c) x/h=1 (d) x/h=3; For different subsonic Mach numbers the plots of (e) Oscillation frequency (f) Strouhal number [83] (Reprinted - Courtesy MDPI open access)

dynamics, affecting jet oscillation frequency, deflection angle, and recirculation bubble formation. An experimental and numerical study was conducted by Zhai and Fan [87] to explore the effects of varying thicknesses and outlet throat widths of the double feedback oscillator on the flow rate, deflection angle, and oscillation frequency. The results showed critical thresholds and driving mechanisms, highlighting the interplay between mass flow and pressure in influencing airflow deflection within the oscillator. The oscillation behavior of a sweeping-vortex low-frequency fluidic oscillator and the effects of its key geometric parameters were analyzed by Yang et al. [88] using computational fluid dynamics.

The study revealed that the jet deflection is influenced by counter-rotating vortex dynamics, with parameters such as oscillator width, chamber height, and outlet diameter significantly impacting oscillation frequency. Woszidlo et al. [89] centered their study on the movement of fluid within the mixing channel and the feedback loops of the double feedback oscillator. They observed that widening the mixing chamber inlet increases frequency, while rounded feedback channels reduce the bubble size formed in the mixing chamber. Slupski and Kara [90] performed a numerical investigation of the influence of changes in the geometry of the feedback loop of a double feedback oscillator. It is observed that increasing feedback channel height raises the oscillation frequency, but greater width lowers it.

Following the analysis of variation of different geometrical parameters and their effects on performance parameters such as frequency, deflection angle, and pressure drop, attention is directed toward the Coanda surface, a critical yet underexplored geometrical parameter in double feedback fluidic oscillator performance. While the Coanda surface has not been extensively studied, the experimental work by Tajik et al. [81] explored variations in Coanda surface shape alongside other geometrical parameters of the double feedback oscillator. Their results demonstrated that the shape of the Coanda surface is the most influential parameter, showing the highest sensitivity to changes in oscillation frequency. Similarly, Hossain et al. [91] found the square-ribbed Coanda surface to be more sensitive towards the oscillation frequency during their numerical study of variation in the feedback channel surface and the Coanda surface of the double feedback oscillator.

The physical behavior of sweeping jet ejecting from a double feedback fluidic oscillator was experimentally studied by Samsam-Khayani et al. [92]. A fully confined and free fluidic oscillator having Reynolds numbers range of 2680–10,730 was investigated.

It was observed from temporally-averaged results that the free domain resulted in a self-oscillating jet. However, under confinement, the jet faced resistance to oscillate from twin symmetric vortices. the Coanda vortex made the externally located flow pattern non-symmetric and the subsequently self-oscillating jet vanished.

The jet tended to oscillate and its strength inclined to cope with these vortices at Reynolds number = 10,730. However, a non-symmetric pattern was achieved through the creation of strong vortices near the fluidic oscillator exit region. An experimental investigation was performed by Wen et al. [93] to study the unsteady flow behavior of a sweeping jet at a jet to target surface distance H/D = 8. It was observed from the results that the sweeping frequency linearly increased in the Reynolds number range of 2.7 x 10^3 to 9.3 x 10^3.

A more uneven sweeping motion was exhibited by the jet in the near exit region at a higher Reynolds number 9.3 x 10^3. Faster switching was observed due to longer intervals of the jet at maximum deflection angle during one cycle of oscillation with high peak velocity and narrower jet. At Reynolds number of 4.0 x 10^3, the flow was observed to be in the outer sides of the near-wall region for more duration and thus a double peak was generated for impingement effects on outer both sides while plotting time-averaged and fluctuating components of velocity. Moreover, the diameter of those vortices increased with the increment in the nozzle to plate distance, therefore, augmenting the jet spread.

The flow dynamics of sweeping jet impingement on a confined concave target surface were experimentally studied by Li et al. [94]. The experiments were conducted at three different Reynolds numbers (Re = 1650, 3300, and 6601) and concave surfaces with various surface curvatures having diameters (R = ∞ , 20D, and 10D) and were located at a spacing of 5.5D (hydrodynamic diameter of jet) from the throat of the jet. An increase in Reynolds number led to intrinsic bi-stability augmentation as a result of a change in jet oscillation wave profile from saw-tooth wave to sinusoidal wave and ultimately to a square wave.

Large trapped vortices pair was observed at a region of lateral recirculation of sweeping jet when the most curved surface (R = 10D) was used in contrast to the flat impinging target surface ($R = \infty$). Enhanced fluctuating velocity, away from the region of direct jet impact, was induced by outer strong vortices. Transitional flow dynamics behavior was shown by surface curvature having an intermediate diameter (R = 20D).

A comparative numerical investigation was performed by Aram and Dejong [95] for the steady and sweeping jet to control jet flow. A larger covered area in spanwise direction was observed for sweeping jet as compared to steady jet and sweeping jet showed better mixing mechanism which controls separation. At reduced spacing (between oscillators) arrangement, adjacent sweeping jets exhibited stronger interaction in the case of sweeping jets. Fuchiwaki and Raghu [96] performed an experimental investigation of the flow structure of a sweeping jet produced by the fluidic oscillator and ejected into the flow. The results showed an evident disruption of the main flow by this sweeping jet at higher velocity ratios which resulted in a significantly changed flow structure. A wider range spreading of the ejected sweeping jet was also observed caused by the interaction of ejected sweeping jet and main flow. A numerical study was carried out by Zheng et al. [97] to analyze the evolution of the external flow field of a sweeping jet double feedback fluidic oscillator. Large vortical structures were observed outside the exit of the oscillator at the start of the oscillation cycle $\Phi = 0°$ and a small vortex was also observed between the main jet and right outlet wall. With the jet sweep moving in the opposite direction induction of another vortex V2 was observed between the main jet and the left outlet wall. The growth and movement of both vortices away from the throat of the oscillator were observed at $\Phi = 45°$ and $\Phi = 90°$. The enlargement was observed till $\Phi = 225°$ and beyond that, at $\Phi = 270°$ the appearance of secondary small vortices near the throat of the oscillator was also observed. At the end of this oscillation cycle, the pair of vortices V1 and V2 moved a distance away from the oscillator exit and the large vortical structures that appeared at frame $\Phi = 0°$ were also pushed away and their strength was decayed. Wen et al. [98] experimentally investigated the flow dynamics of interacting dual sweeping impinging jets at various Reynolds numbers as displayed in Fig. 2.8(a). Three different Reynolds numbers 1.8 x 10^3, 5.5 x 10^3, and 9.2 x 10^3 based on jet hydraulic diameter were used during the study. The results showed that at the lowest Reynolds number of 1.8 x 10^3 the dual sweeping jets showed behavior similar to that of two separate jets having relatively steady sweeping jet velocity and in-phase sweeping movement. A wall vortices pair was noted in the central region between the two dual sweeping jets Fig. 2.8(b). From the near-wall temporally averaged flow fields it was observed that a maximum peak of streamwise velocity for both jets and a peak pair (positive and negative) of transverse velocity sideways along the wall were generated. A lateral peak for turbulence fluctuations in either direction was also produced. Whereas at the highest Reynolds number 9.2 x 10^3 during a single actuation cycle, highly distorted patterns of oscillation and significant changes in jet velocities were experienced by dual jets. A transition stage of dual-stage sweeping jet performance was observed at an intermediate Reynolds number of 5.5 x 10^3. Dual jets produced results in terms of induced wall vortices, dynamic behavior, and resulting temporally averaged impingement, similar to results produced by sweeping jets with a single large fluidic oscillator. Meng et al. [99] numerically studied the dual sweeping jet actuator by installing an oscillator on the suction side of the blade. A reduced pressure loss coefficient of 6.8% was obtained using a dual sweeping jet as compared to a single sweeping jet. Transient structures and flow field unsteadiness was also analyzed.

Tomac and Gregory [100] carried out an experimental investigation of a dual impinging jet with oscillatory behavior in a dome-shaped mixing chamber, at a relatively high flow rate corresponding to a Re = 6800. A saddle point formation jet's bifurcation was recorded at high flow rates, whereas a continuous collision was experienced by jets at low and medium flow rates. The bifurcation altered the mixing of dual jet impingement.

In a given flow regime the location of saddle point formation dictated the oscillator sweep angle. The variation in sweeping angle varied from 10° to 80° in the Reynolds

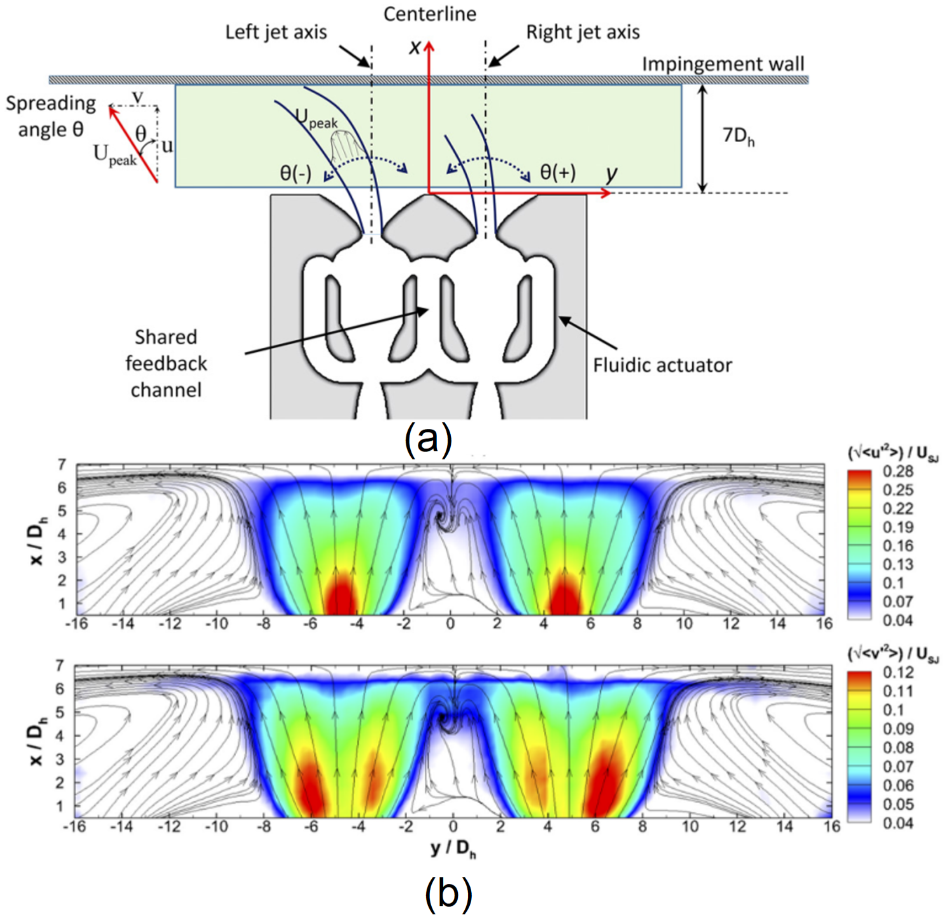

FIGURE 2.8: Dual sweeping jet impingement (a) geometry (b) turbulent energy x and y directions [98] ((Reprinted - Courtesy American Institute of Physics)

number range of Re = 800-2000 and for a higher range of Reynolds number (Re = 2000-7000), an almost constant sweep angle of 46° was obtained.

Double feedback fluidic oscillators in a stacked arrangement were studied both experimentally and numerically to investigate the characteristics of flow and frequency of sweeping jets by Tomac and Hossain [101]. The range of Reynolds numbers used during the study was from 5660 to 17,000 and oscillation frequency varied between 263 and 672 Hz. Three-dimensional symmetric time-averaged flow streamlines were observed at section plans of synchronized interacting feedback channels and were considered to be responsible for the overall synchronized behavior of the jets.

Another interesting numerical investigation was performed by Sundstrom and Tomac [102] using oppositely faced back-to-back double feedback fluidic oscillators for studying its flow characteristics. The goal achieved through this design was the production of two synchronized sweeping jets through a shared feedback channel which can help in flow control.

A numerical investigation was conducted by Kim and Kim [103] to study the aerodynamic performance of an airfoil by changing the angle of attack from 0° to 24° and four different installation locations of the fluid oscillator on the airfoil. Reduced drag was achieved with installation location of fluidic oscillator closed to leading-edge irrespective of the value of angle of attack. Kim and Kim [104] further investigated the impact of the bending outlet of the fluidic oscillator on airfoil to study its aerodynamic performance. Melton et al. [105] observed a similar increase in the lift at a low flow rate for a steady jet and when a fluidic oscillator was used on the airfoil. In other applications, a non-vented fluidic oscillator was numerically studied by Tseng et al. [106] for enhancing the water removal rate from Polymer Electrolyte Membrane Fuel cells. For high Reynolds number cruise configuration applications, various fluidic oscillator designs were explored both experimentally and numerically by Jones et al. [107].

Pandey and Kim [108] carried out a comprehensive numerical investigation on a double-feedback fluidic oscillator using two widely adopted turbulence modeling approaches: Large Eddy Simulation (LES) and Unsteady Reynolds-Averaged Navier–Stokes (URANS). The purpose of this comparison was to evaluate the predictive capabilities and accuracy of each method in capturing the unsteady flow characteristics inherent to the fluidic oscillator. While LES is generally known for its ability to resolve a wide range of turbulent scales with high fidelity, it is computationally expensive. On the other hand, URANS provides a more computationally efficient approach by averaging the effects of turbulence over time. In their study, URANS showed better agreement with the available experimental data compared to LES. This outcome suggests that, for the specific case of the double-feedback fluidic oscillator under investigation, URANS may offer a more practical and reliable option in terms of both accuracy and computational cost. In the recent studies, Martinke et al. [109] experimentally demonstrated that the oscillation in fluidic oscillators is primarily governed by the fluid volume in the feedback channels, a finding established using a novel design with externally controlled valves.

At the end, Table 2.1 comprehensively presents the various geometrical parameters considered in this study, along with a detailed description of their individual and combined impacts on the flow characteristics.

Table 2.1: Geometrical parameters of fluidic oscillators and their key role in flow control

Geometrical parameters	**Impact on flow characteristics**	**Key role in jet flow dynamics**
Power nozzle exit width	Internal and external	Increased power nozzle velocity increases the oscillating frequency. Lower velocity causes variations in stagnation pressure oscillations at the mixing chamber.
Mixing chamber inlet and outlet widths	Internal and external	Faster fluid flip with larger exit when nozzle exit is smaller.
		Equal inlet/exit areas reduce impact. Jet oscillations cease beyond critical area due to fluid starvation and Coanda effect loss.
Mixing chamber inlet angle	External	Jet amplitude and frequency increase with greater inlet angle.
Mixing chamber outlet angle	External	Larger angles reduce amplitude and frequency of oscillations.

Table 2.1: Geometrical parameters of fluidic oscillators and their key role in flow control (continued)

Geometrical parameters	**Impact on flow characteristics**	**Key role in jet flow dynamics**
Mixing chamber vertical length	External	Oscillation frequency decreases with length (inverse nonlinear relationship).
Feedback channel vertical length	External	Longer channels reduce or stop oscillations due to randomness.
Exit nozzle length	External	Shorter nozzles reduce jet spread angle and flow efficiency.
Exit nozzle angle	External	Spread angle increases up to a limit then decreases. Internal flow is mostly unaffected.
Feedback channel width	External	Wider channels increase frequency but reduce jet pressure and deflection.
Coanda surface shape	External	Curved shape bifurcates the flow; angled gives homogeneous profile. Frequency is slightly higher with homogeneous profile.

2.2 Heat Transfer through Sweeping Jet Impingement

The behavior of cyclical oscillation of fluid stream produced through operation of sweeping jets is influenced by various geometrical parameters (inlet and outlet geometry, size and shape of obstacle, and dimensions of feedback channel) of fluid oscillator and Reynolds number. Sweeping jet impingement using a double feedback oscillator has been widely used in heat transfer enhancement studies over hot surfaces. The application of fluidic oscillators in thermal systems has attained significant interest among researchers, primarily because of the self-induced oscillating behavior of sweeping jets. The first reported experimental study on sweeping jet fluidic oscillators for jet impingement cooling was conducted by Herr and Camci [110], who examined the heat transfer coefficient and jet-to-wall distance effects under unconfined conditions. Their results showed up to 70% enhancement in heat transfer compared to steady jets. However, some other techniques to excite the jets for thermal applications are also in use. In this regard, Camci and Herr [111] performed an experimental investigation to study heat removal performance from a flat target surface using sweeping jet impingement where a self-oscillating jet was achieved through a simple fluidic nozzle.

The jet to target surface spacings were kept at 24D, 30D, 40D, 50D, and 60D, and Reynolds numbers used during the experiment were 7500, 10,000, and 14,000. It was observed from the results that 20-70% enhanced heat transfer was achieved by using a self-oscillating jet when compared to a steady jet.

Wen et al. [112] performed an experimental study using a master-slave fluidic oscillator design to study its heat transfer characteristics in thermal applications. The parameters used during the study were master flow rate (percentage of flow rate in the master flow rate ranging between 0 and 1), the jet spread angle = 0°-100°, Re = 4,000, and convex cylinder diameter ratio D/Dh = 2.5 and 12.5. It was observed from the results that a larger heat transfer region and high thermal exchange were obtained at a master flow rate of 1 as compared to the master flow rate of 0 when a higher D/Dh ratio cylinder was used. Weak sweeping jet interaction with the cylinder, at a master flow rate of 1, was produced by enhanced jet spreading angle. The design of the sweeping impinging jet in this study could induce a change in jet spreading angle even if the actuator geometry and flow rate remain unchanged therefore, it was considered more flexible in thermal applications. An experimental study was performed by Kim et al. [113] using a feedback-free oscillator to investigate the effect of sweeping jet impingement on thermal performance. The parameters used were Re = 8,000-32,000 and spacing between jet and target surface Z/dh = 3-8. Thermal performance of sweeping jet obtained from feedback-free oscillator decreased with increase in spacing between jet to wall. At narrow spacings feedback-free sweeping jet exhibited superior performance when compared to square jet at all values of Reynolds number.

A new sweeping jet was proposed in the experimental study of Tomac [114] for enhancement of the resultant spray jet flow. This increase in mixing efficiency was achieved by the provision of continuously synchronized jet impingement and a large volume was stably covered in this manner. The unsteady behavior of flow at the exit of the double feedback fluid oscillator makes sweeping jet impingement an effective method to attain intensified heat transfer in different applications.

An enlarged area of enhanced heat transfer on the target surface was recorded with the sweeping jet as compared to the steady jet. A numerical study was performed by Lundgreen et al. [115] to investigate heat transfer characteristics of sweeping jet impingement using a double feedback oscillator.

The study was performed for a flat plate target surface with jet to plate spacing 3, 4, 6, and 8 and five different flow rates 10 slpm, 25 slpm, 50 slpm, 75 slpm, and 100 slpm. It was observed from the results that the average Nu was higher for sweeping jets as compared to steady jets at the low jet to plate spacing. However, at the large jet to plate spacing heat transfer performance suffered due to the large sweeping distance of the oscillating jet.

An experimental study was conducted by Agricola et al. [116] to study the heat transfer performance of sweeping jet impingement using a curved fluidic oscillator for different Reynolds numbers, jet to target surface spacing, and exit nozzle angle. The results of the Nusselt number showed that heat transfer performance improved for sweeping jet impingement, similarly to a steady circular jet, with an increase in Reynolds number. Near the stagnation point, the Nusselt number increased by reducing the space between jet and target surface from 7dh to 5dh. The jet to target surface spacing for maximum heat transfer performance for the sweeping jet was noted to be different than the steady jet because of the extra distance that an angled sweeping jet had to travel before hitting the target surface as compared to the steady jet. It was also observed that maximum spreading and resultant large heat transfer area was achievable at the greatest exit angle of fluidic oscillator that still keeps the jet attached to nozzle walls. The high spreading of the jet, however, may decrease impingement heat transfer in the stagnation region and thus the exit angle can be reduced for such requirement.

An experimental investigation was performed by Thurman et al. [117] for studying the cooling performance of sweeping jet impingement using double feedback fluidic oscillator. The parameters used during the study were: Re = 11,000, blowing ratio, BR = 1-2.5, area of exit = 1.69mm x 0.95mm and nominal sweeping fluidic hole diameter = 6.35 mm having angle of 300°. The results showed that contours of velocity and flow temperature were obtained at discreet positions at flow fields located downstream. While uniformity in cooling distribution was exhibited by sweeping fluidic holes due to mixing enhancement. In another study, Hossain et al. [118] numerically investigated the impact of fan exit angle of sweeping jet over heat transfer performance. The coolant mass flow rates used during the study were 50 slpm, 75 slpm, and 100 slpm, and three jets to target surface distances (H/D) of 3, 5, and 8 were studied. The numerical simulations were performed for eight different sweeping jet fan exit angles in the range of $0° \leq \theta \leq 130°$. The role of fan exit angle upon local Nu distribution was found to be significant for sweeping jet impingement. Deterioration in average heat transfer at the target surface was observed as the exit angle was increased. However, the heat transfer was more uniformly distributed over the target surface with an increase in exit angle. Additional hot air entrainment was recorded by temperature flow fields which caused significant heating of core flow by the sweeping motion of the jet.

The characterization of the heat transfer capability of sweeping jet impingement on a flat target surface, as shown in Fig. 2.9(a), was experimentally investigated by Park et al. [119]. The experimental study for local Nu evaluation was performed at Reynolds number values of Re = 3600, 6400, 11,000, and 15,300 and for the distance between the nozzle to the target plate of H/d = 1.0, 1.5, and 2.0 as presented in Fig. 2.9(b). Based on Nu distribution, two regions of the impingement heat wall were identified; a high Nu region near the central region and the monotonically decreasing Nu region away from the center. It was established that unsteady effects produced by sweeping motion had an influential role in the determination of the local rate of heat transfer. For all three nozzles to target plate spacing H/d = 1.0, 1.5, and 2.0 the value of Nu showed an increasing trend with an increase in Reynolds number as observed in Fig. 2.9(b). The reason for this increased Nu is the capability of high jet velocity (Reynolds number) to convect more heat energy from the hot surface. An interesting trend was observed at fixed Reynolds number when H/d was varied, Nu showed a steep decline in the region of $x/d < 1$ as compared to $x/d > 1$ region. Similarly, from Fig. 2.9(c), it could be observed that the heat transfer rates of sweeping jets were significantly greater as compared to round jets.

An experimental investigation was performed by Agricola et al. [120] to analyze the heat transfer performance of a sweeping impinging jet in a turbine vane leading edge by using a low-speed linear cascade. The flow parameters used during the study were 0.3% and 6.0% free turbulence levels with a constant cascade inlet freestream velocity of 9.75 m/s and three different impingement coolant plenum mass flow rates of 0.125, 0.188, and 0.25 g/s. The fluid oscillator used during the study was double feedback curved fluidic oscillator as depicted previously in Fig. 2.3(a). Steady circular jet recorded better heat transfer performance at both turbulence intensity levels and all three mass flow rates as compared to sweeping jets and a lesser pressure drop were experienced across steady circular jet geometry when compared to sweeping jet geometry. Spens and Bons [121] performed an experimental study to investigate the cooling performance of sweeping jet impingement using a double feedback oscillator for turbulence intensity Tu = 0.5% and 11% and blowing ratio, BR = 1.0-4.0. It was observed from the results that lower cooling performance was experienced for synchronized sweeping jet pair design as compared to individual sweeping jet and unsynchronized sweeping jet pair. The decrease in cooling performance was caused by internal streamwise alternating vortices.

An experimental study was performed by Hossain et al. [122] to investigate the

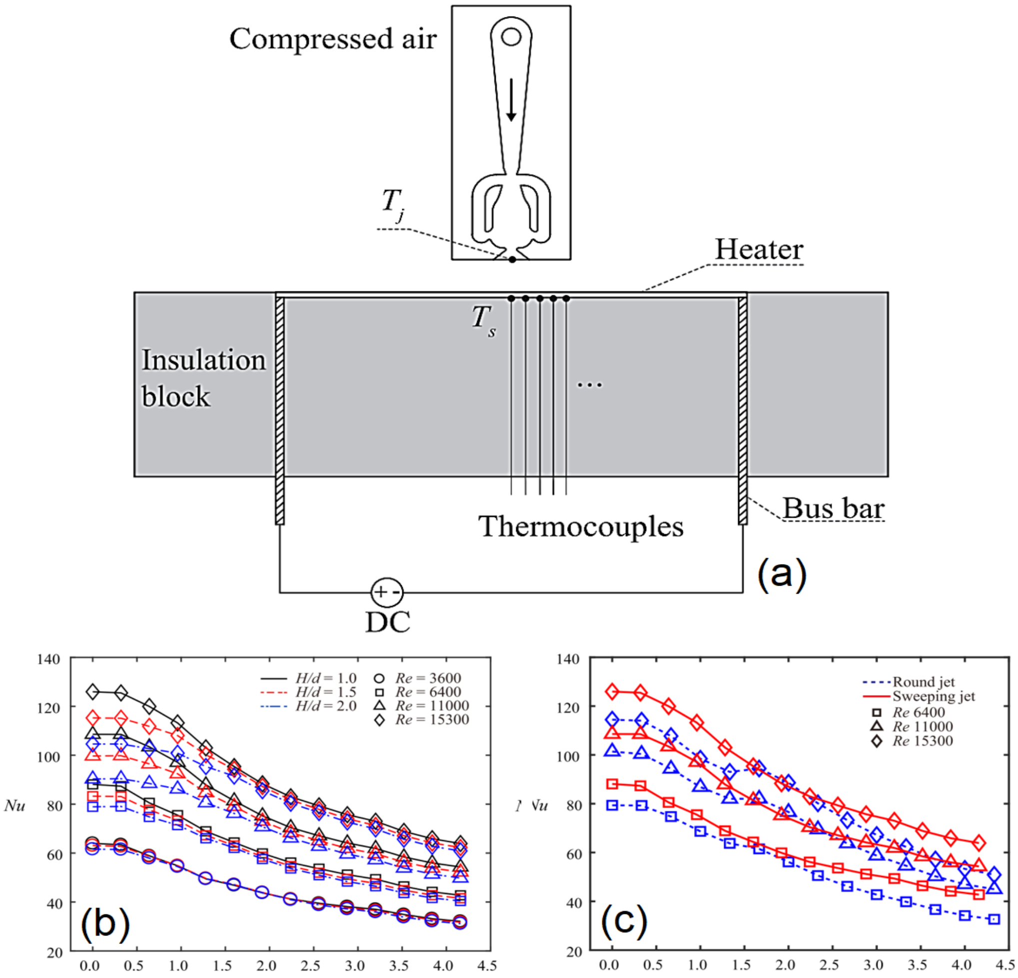

FIGURE 2.9: (a) Experimental setup for heat transfer measurement; Local Nusselt numbers for (b) different nozzle to plate spacing and Re (c) round jet and sweeping jet comparison [119] (Courtesy Elsevier)

cooling performance of a double fluidic oscillator using sweeping jet impingement. The parameters used during the study were: aspect ratio AR = 0.5-1.0, turbulence intensity Tu = 0.5% and 10.1% and spacing between jet and target surface H/D = 3, 5 and 8. Cooling performance was observed to decrease as AR decreased and the maximum cooling performance was recorded at an AR value of 1.0. Maximum cooling performance was noted for the sweeping jet at H/D = 5 at all AR values as compared to the steady jet due to the dominant sweeping motion of the jet. Zhou et al. [69] performed an experimental study to investigate the effect of sweeping jet impingement on heat transfer performance at the narrow jet to target surface spacings of H/D = 0.1, 1.0, 2.0, and 3.0 and Reynolds number values of 5000, 10,000, and 15,000. Heat transfer performance was observed to be improving with increasing Reynolds number and decreasing jet to target surface spacing. Enhanced heat transfer in the far region was obtained due to oscillation of coolant which enabled the sweeping jet to cover a larger area. As compared to the circular jet, a 14% increased heat transfer was noted while using the sweeping jet.

The two fluidic oscillator models (i) angled oscillator and (ii) curved oscillator, used by Ostermann et al. [76] were further utilized by Wu et al. [123] and compared to direct jet in their large eddy simulation study for analyzing heat transfer performance of sweeping jet impingement. An increase in heat transfer performance was reported for sweeping jet impingement in all three models with an increase in Reynolds number. The direct impinging jet was found to be most effective near stagnation point heat removal performance but a sharp deterioration in its effectiveness to cool the target surface was observed away from the stagnation point. The angled and curved fluidic oscillators presented a better average and more uniformly distributed heat transfer performance with an increase in heat removal performance of 7.4-8.6% and 3.0-8.3% respectively at the Reynolds number range of 3000 to 5000. The heat transfer performance of the angled oscillator was superior to that of the curved oscillator. At higher Reynolds numbers the space between high Nu spots was widened to each other and the coverage area of sweeping jet also increased. Fig. 2.10(a-c) also manifests that the curved and angled design of fluidic oscillators shows a much larger high heat transfer span. The double feedback angled fluidic oscillator of Ostermann et al. [76] alongside a single loop and a feedback-free oscillator were experimentally studied by Ghanami and Farhadi [124] for heat transfer investigation in a single pipe heat exchanger. The results were obtained for a Reynolds number range of 5600 to 16,400 and surface thermal conditions of (i) CCHF: constant continuous heat flux and (ii) CPIHF: constant periodically interrupted heat flux. By installing a fluidic oscillator at the inlet of the tube using CCHF, heat transfer was enhanced by 37% for feedback-free, 83% for a single feedback loop, and 23% for two feedback channel fluidic oscillators as compared to a steady flow. In the case of CPIHF, only a single loop fluidic oscillator produced a 57% enhancement in thermal performance as compared to the steady flow.

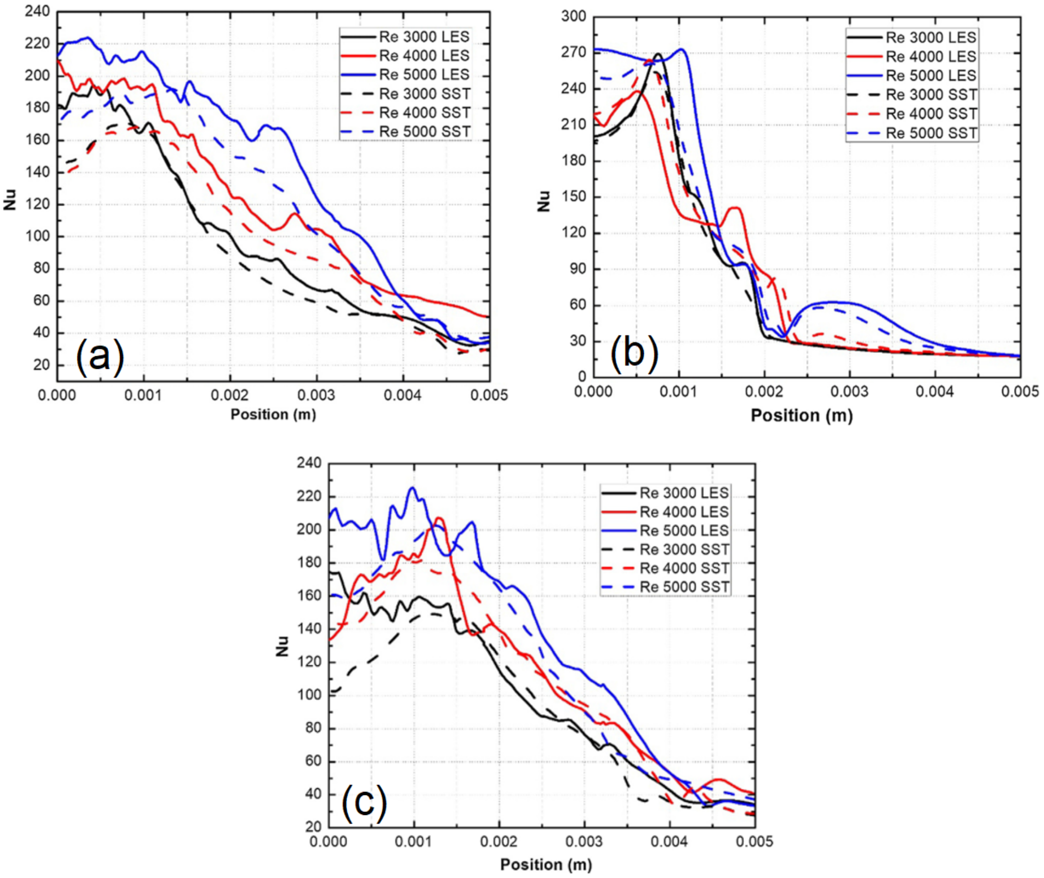

FIGURE 2.10: Time-averaged Nu results of LES of sweeping jets at Re 3000 and 5000 (a) curved design (b) direct jet design (c) angled design [123] (Courtesy Elsevier)

An experimental study was performed by Kim et al. [125] to investigate the 2D heat transfer performance of sweeping jet impingement while using a double feedback oscillator. The experiments were performed for a Reynolds number range of 8000-32,000 and jet to target surface spacing range of Z/dh = 3-10. A linear increase from 60 Hz to 220 Hz in oscillation frequency was observed with an increase in Reynolds from 8000 to 24,000. The increase in heat transfer performance was substantially high while using sweeping jet impingement instead of steady square jet impingement because of the greater turbulence induced by sweeping jet flow oscillation and enhanced impinging jet velocity near the stagnation point. However, as the gap between the jet and target surface was increased, a drastic reduction in heat transfer performance was observed due to a reduction in impinging velocity. 53% reduction in maximum Nu for sweeping jet and 10% decrease in maximum Nu for the steady square jet was recorded at Reynolds number 32,000 when Z/dh was increased from 3 to 5. A wider plateau of Nu distribution at the center region and a much smaller decay in the slope of Nu along the x-axis from the center point were observed for sweeping jet as compared to steady jet.

An experimental investigation was performed by Mohammadshahi et al. [126] to study the sweeping jet impingement, produced by a double feedback fluidic oscillator, in a crossflow. The range of blowing ratios used during experiments was 1-3.33 and the cross-flow Reynolds number ranged from 510 to 2700. The results demonstrated a dominant role of cross-flow over heat transfer and variation in blow ratio was found insignificant.

The impinging jets as compared to oscillating jets under crossflow conditions resulted in an increase in heat transfer by 200%. Hewakandamby [127] presented a numerical heat transfer enhancement study for two oscillating jets originating from adjacent slots; of the same frequency but a phase shift $\pi/2$ on a planar surface.

The Reynolds number range used during the study was $0 < Re \leq 1200$. 100% improved heat transfer was observed when results for oscillatory flow jets were compared to conventional steady jets. This enhancement in heat transfer was caused by the disruption of the boundary layer periodically by oscillating jets.

A numerical investigation was performed by Eghtesad et al. [128] to study the potential of heat transfer performance using twin turbulent sweeping jets (TTSIJ). Eight different design variables are divided into 4 groups; Group I: Reynolds number, hydraulic diameters of the nozzle, and phase shift between TTSIJ, Group II: Jet to target surface distance and maximum swing angle, Group III: Oscillation frequency and pulsation frequency, and Group IV: Jet to jet spacing were studied to evaluate their impact on Nu distribution on impinging target surface. It was observed from the results that the parameters included in group I had a positive impact on heat transfer.

The heat transfer coefficient increased with an increase in Reynolds number. More cooling through the attainment of higher heat transfer performance was achieved through increased hydraulic diameter which resulted in the application of a higher flow rate of air into the domain.

Heat transfer augmentation and the potential of shifting the maximum heat transfer in lateral directions from the center were obtained through periodic vortex generation produced by phase shift between twin turbulent jets. Unlike the positive effects induced by the previously mentioned parameters, an increase in jet to target surface spacing resulted in decreased intensity in the collision of twin jets and hence maximum Nu was reduced.

The faster sweeping motion was achieved through an increase in a maximum sweeping angle which reduced the time to transfer heat but with the advantage of more uniform cooling of the target surface. At low oscillation frequency, the heat transfer rate was increased by disturbing the impingement surface boundary layer and higher flow fluctuations and at medium oscillation frequency, the rate of heat transfer was observed to be constant due to nullification of negative impact of reduced interaction between the target surface and flow by the positive impact of rapid boundary layer disturbance. While at higher oscillation frequency the twin sweeping jets were forced to exhibit fast sweeping motion resulting in reduced heat transfer time but the cooling on the target surface was more uniformly distributed. Improved heat transfer was observed with pulsation frequency through more flow mixing and boundary layer disturbance. The jet to jet spacing was involved in moving the location of maximum Nu on the target surface with no alteration in the magnitude of the average Nu of the target surface. Hossain et al. [129] performed an experimental and numerical study to investigate the heat transfer performance of a double feedback curved fluidic oscillator. The parameters used during the study were blowing ratios, BR = 0.98 to 3.96, spacing between any two feedback channels = 6.9D, and spacing between leading and trailing edge = 2D. It was observed from the results that the fluidic oscillator's sweeping action produced a significant enhancement in cooling effectiveness laterally. The lateral spread was caused by twin alternative streamwise vortices for all M values.

In another study, Hossain et al. [130] performed an experimental and numerical investigation to study the effect of the nozzle exit angle of a double feedback fluidic oscillator over heat transfer performance on a hot surface using sweeping jet impingement. The nozzle exit angle used was: $0° \leq \theta \leq 130°$, nozzle to flat plat distance: H/D = 5, and Coolant mass flow rates were $\dot{m} = 0.97$, 1.48, and 1.97 g/s. The results showed that at large exit angles the cooling of the flat target surface was more uniform and average heat transfer was observed to reduce with an increase in exit angle. Mohammadshahi et al. [131] performed a numerical and experimental investigation to study a double feedback oscillator for different working fluids (water and air) at a Reynolds number range of 8000-32,000. However, no significant influence was shown on heat transfer with variation in mass flow rate due to an increase in vortices convection velocity with enhancement in mass flow rate. A numerical study was performed by Ming et al [132] to investigate the heat transfer performance of sweeping jet impingement produced by an array of the self-oscillating oblique fluidic oscillator. The tilt of the fluidic oscillator was at 30° increasing the jet influence area over the impingement target surface. Three different modes of oscillation i.e co-directional, reverse and regular, were observed while recording pressure and velocity fields. Heat transfer performance was improved through sweeping jet impingement achieved by using oblique double feedback fluidic oscillator. An increase in Nu and an enlarged jet influence area above the target surface were achieved. A higher average Nu and more uniform cooling were recorded by sweeping jet impingement. All three oscillation modes of sweeping jets showed similar heat removal performance.

Few researchers have also explored the target surface variation under sweeping jet impingement for improvement in thermal performance. In this regard, Hossain et al. [133] performed a numerical investigation to study the heat transfer performance of sweeping jet impingement at a different radius of curvature of the impingement surface. Normalized by throat hydraulic diameter (Dh), two surfaces with a radius of curvature of 20Dh and 10Dh and a flat target surface are used during the study. The study was conducted for three different Reynolds numbers 10,000, 20,000, and 35,200 along with a jet to target surface spacings of 3, 5, and 8. The results showed that a non-monotonic behavior of heat transfer performance with surface curvature for the sweeping jet was observed. However, while using a steady jet, heat transfer was augmented with surface curvature. An increased heat transfer rate was achieved with an increase in Reynolds number and reducing jet to target surface spacing. An improved heat transfer performance for sweeping jet as compared to steady jet was observed at the jet to target surface spacing of H/Dh = 5, Reynolds number 35,200, and radius of curvature R = 20Dh. The application of sweeping jet impingement to analyze heat transfer performance on a concave, convex, and flat target surface was experimentally studied by Kim et al. [134] using a double feedback fluidic oscillator as shown in Fig. 2.11(a).

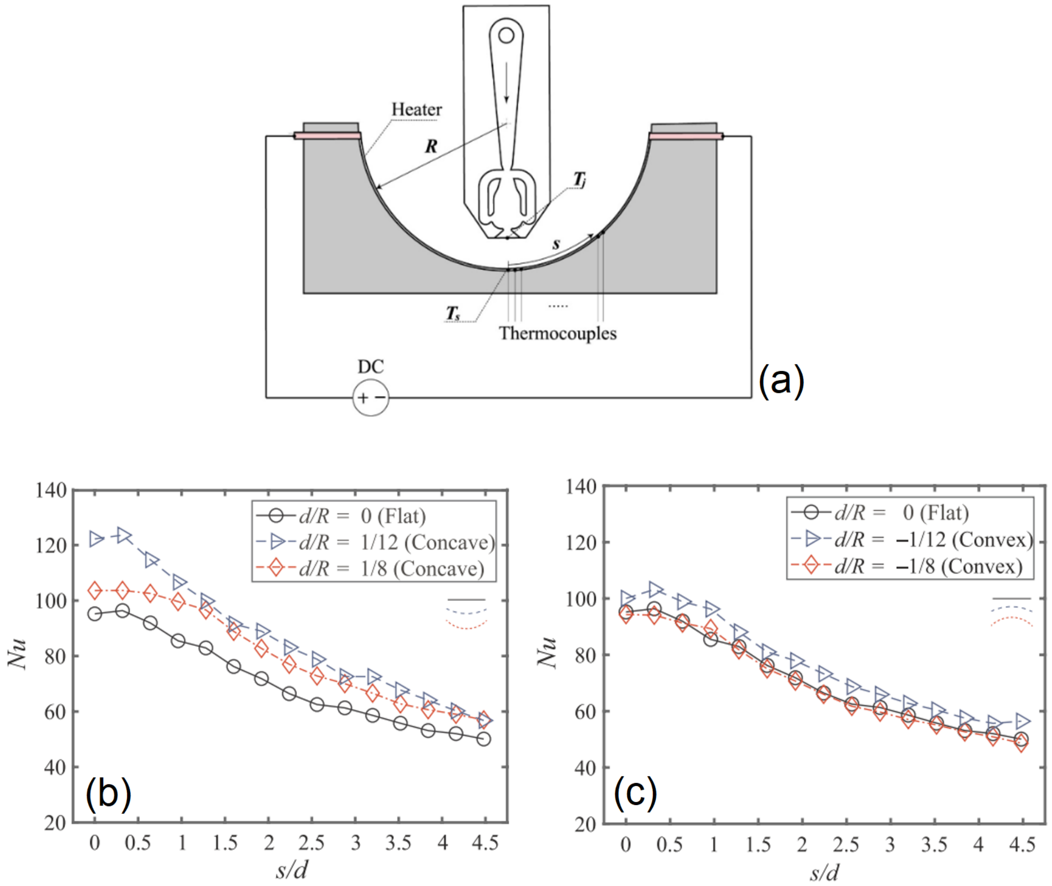

FIGURE 2.11: (a) Experimental setups for heat transfer and flow measurement; Comparison of local Nusselt number at Re = 11,000 and H/d = 1.5 for flat plate and (b) concave surfaces (c) convex surfaces [134] (Courtesy Elsevier)

It was observed from the results that the concave surface showed better heat transfer performance when compared to the flat target surface and the convex surface showed a smaller enhancement in heat transfer rate as manifested in Fig. 2.11(b, c). The curvature magnitude variation for both curved surfaces (concave and convex) did not show a monotonic relation with Nu but a peak in Nu was observed at moderate curvature. Improved heat transfer was achieved for both concave and convex surfaces due to a thinner jet wall as compared to the flat surface. However, the turbulent kinetic energy for the concave surface at moderate curvature was larger than the convex surface when both were compared to the flat surface and hence the concave surface showed better thermal performance.

An experimental study was accomplished by Osorio et al. [135] to study the heat transfer performance of sweeping jet impingement on a heated circular target surface for two configurations i.e confined and unconfined. The series of experiments were conducted for a fixed jet Reynolds number and varying jet to target surface distance. Enhancement in heat transfer was observed for sweeping jet impingement unconfined case at the jet to target surface distance of 3 and lower heat transfer was recorded for confined cases at the jet to target surface distance of 4 and 6 when results were compared to rectangular slot orifice. The use of a fluidic oscillator resulted in increased jet momentum and level of mixing which caused the intensified heat transfer. In another published work, Kong et al. [136] performed a numerical study to investigate heat transfer performance on a flat plate with film holes using sweeping jets. The results showed radially more uniform cooling by using sweeping jets instead of direct jets.

A 2D numerical study was performed by Abdelmaksoud and Wang [137] to explore the fluidic and thermal performance of sweeping impingement jets, comparing free and confined impingement configurations. A k-ω SST turbulence model was employed to analyze a system with a constant heat flux of 3000 W/m^2, a jet-to-wall distance of 4, and a Reynolds number of 2500. The findings indicate that confined impingement schemes enhance cooling efficiency for sweeping jets in comparison to steady jets, whereas steady jets perform marginally better in unconfined setups. Joulaei et al. [138] performed a numerical study to compare the thermal performance of oscillators, both in the presence and absence of the external diffuser. The results indicated that fluidic oscillators without external diffusers exhibit the highest thermal efficiency. Furthermore, they observed better heat transfer performance between the oscillator designs at lower jet to target hot

Table 2.2: Important parameters of sweeping jet impingement and their impact on thermal performance

Parameter	**Impact on target surface heat transfer**
Jet-to-target surface spacing	Lower spacing increases collision intensity and impinging velocity, enhancing heat transfer rate.
Oscillation frequency	Higher frequency enhances heat transfer through increased jet fluctuations. Very high frequencies diminish peak Nu values due to reduced surface–fluid interaction time. Produces more uniform cooling. Sensitive to power nozzle exit width, mixing chamber dimensions, feedback channel geometry, and Coanda surface shape.
Exit nozzle angle	No effect on oscillation frequency as internal flow dynamics remain unchanged. Larger angles deteriorate area-averaged heat transfer but improve uniformity.
Nozzle hydraulic diameter	Larger diameter increases fluid flow rate, resulting in higher heat transfer.
Reynolds number	Higher Reynolds number enhances fluid momentum, increasing the heat transfer coefficient. Linearly increases sweeping jet oscillation frequency.

plate spacing. The oscillatory frequency is the key parameter for describing the flow dynamics and performance of sweeping jets. An increase in the oscillatory frequency of the sweeping jet is observed when the dimensions of the oscillator are reduced [139, 140]. Joulaei et al. [141] conducted a two-dimensional numerical study on the impact of geometric scaling on thermal performance for a heated plate subjected to jet impingement. The study explored scaling factors ranging from 0.33 to 1.3. The results showed that reduced scaling factors increased oscillation frequency and heat transfer due to smaller separation bubbles. The highest Nu was observed at a scale factor of 0.33, showing a 13% improvement over the baseline. Table 2.2 presents various key parameters used in the sweeping jet impingement system and their role on thermal performance.

2.3 Optimization Techniques to Enhance Flow and Heat Performance

The performance of a double feedback oscillator can be significantly improved through single and multi-objective optimization, as enhancing its oscillating frequency and jet spread angle leads to better heat transfer and more effective cooling of heated surfaces in impinging sweeping jet applications like turbine blade cooling while minimizing pressure loss ensures energy-efficient operation. Several optimization techniques have been used to achieve this goal. A numerical study was performed by Jeong and Kim [142] to optimize a fluidic oscillator, aiming to enhance peak jet velocity while minimizing pressure loss.

Multi-objective genetic algorithm-based optimization, supported by surrogate modeling, was employed, with inlet nozzle width ratio and splitter distance as design variables. The results demonstrated that a jet velocity-focused design achieved an 11.18% increase in peak jet velocity and a 16.82% rise in the friction factor compared to a pressure drop-oriented design.

A numerical study was conducted by Eghtesad et al. [128] to analyze the performance of oscillators used in sweeping impinging jets. Eight design variables, including nozzle hydraulic diameter and maximum sweeping angle, were optimized using an artificial neural network (ANN) in combination with a genetic algorithm (GA). The investigation demonstrated that increasing the Reynolds number and nozzle diameter resulted in increased fluid momentum and higher airflow rates, significantly improved cooling efficiency.

Taguchi method is the most significant and common technique used for optimization in various fields. Taguchi method has been effectively applied to optimize fluidic oscillator performance. An experimental study using the Taguchi design of experiment was conducted by Park et al. [143] on the sweeping jet oscillator, where five design variables with four levels were varied, including the length of the oscillator gap size between inner blocks.

The results showed that the aforementioned two factors were the most influential design factors on oscillation frequency and jet oscillation angle. Furthermore, oscillator length had a greater impact on oscillation frequency than gap distance, regardless of nozzle pressure ratio.

In some cases, the combined CFD-Taguchi-GRA analysis is performed for multi-objective optimization. A combined approach of CFD modeling and Taguchi-GRA was utilized by Shenge, D [144] for optimization of the flow control device in a single-strand tundish. By applying multi-objective optimization, the study effectively maximized inclusion removal and minimized the dead volume fraction, demonstrating the robustness of the Taguchi-GRA method in enhancing CFD-driven designs.

A weighted Grey Relational Analysis combined with Taguchi and the Analytic Hierarchy Process was used by Younas et al. [145] to optimize machining parameters for turning Ti6Al4V alloy. This approach effectively improved multiple performance metrics, demonstrating significant enhancements in material removal rate, specific cutting energy, tool life, and surface roughness.

The numerical study performed by Tang and Li [146] focused on the shape optimization of a fluidic oscillator by employing an adjoint optimization technique, with numerical simulations conducted under specific operating conditions, including a jet Reynolds number of 10,308. The optimized design minimized surface-averaged temperature, reducing the jet's oscillation angle and enhancing velocity concentration, which strengthened the wall jet and expanded the cooling range. Results demonstrated an 11.6% increase in the Nu and a 2.4 K reduction in temperature compared to the baseline configuration. Jabbari and Esmaeili [147] also used adjoint optimization and showed that Coanda surface and feedback channels can simultaneously enhance jet oscillation frequency by 70% and reduce internal pressure losses by 18%.

The numerical study conducted by Kim et [148] focused on optimizing an impingement system using the second-order response surface method, with thermal analysis performed under varying design conditions, including jet spacing, channel height, mass flux ratio, and main flow temperature. The optimized design minimized thermal stress by evaluating inline and staggered jet configurations and cooling flow directions.

2.4 Conclusion

Jet impingement remains one of the most effective techniques for achieving high heat transfer rates in engineering applications. Among its variations, sweeping jet impingement, driven by fluidic oscillators, has gained significant attention for its ability to enhance both the rate and uniformity of cooling by spreading the jet across a larger surface area.

From the reviewed studies, it is evident that the geometric configuration of the fluidic oscillator including the inlet, outlet, and feedback channels strongly influences jet behavior and, consequently, the thermal performance of the impinging flow.

Both numerical and experimental investigations have demonstrated that optimizing these design parameters can significantly improve the oscillation frequency, jet deflection, and overall heat transfer performance.

Furthermore, the flow characteristics at the oscillator's throat and the resulting oscillation dynamics play a crucial role in determining the cooling effectiveness of sweeping jets. These oscillatory jets enhance convective heat transfer primarily through periodic boundary layer disruption, promoting better coolant mixing and a more uniform temperature distribution across the target surface.

Overall, the literature confirms that while sweeping jet impingement offers superior thermal performance compared to steady jet impingement, the degree of enhancement strongly depends on the oscillator's internal geometry and operating conditions. These insights provide a clear foundation for exploring novel geometric modifications, such as Coanda surface alterations, to further improve the heat transfer characteristics of double feedback fluidic oscillators, an aspect that remains underexplored in existing research.

2.5 Research Gap

Extensive research on double feedback oscillators has primarily focused on altering design parameters such as feedback channel dimensions, inlet/outlet configurations, and mixing chamber geometry. Despite its significant role in determining oscillator flow performance, the Coanda surface has received limited attention in prior studies. No existing study demonstrates the effect of increased oscillation frequency, achieved through Coanda surface modifications, on heat transfer performance. Ribs were incorporated on the Coanda surface based on established surface-texturing concepts, which are known to modify near-wall momentum distribution and introduce controlled flow disturbances. The novelty of the present study is that it aims to optimize the Coanda surface by varying three parameters: rib aspect ratio, number of ribs, and rib angle. This comprehensive approach seeks to improve the oscillatory jet frequency and spread angle, thereby providing a more in-depth understanding of fluidic oscillator flow performance. The rib angle on the Coanda surface, along with the aspect ratio and the number of ribs, is optimized using a combination of CFD-Taguchi-Grey relational analysis techniques. This technique is a comprehensive and efficient optimization technique widely used for the optimization of single-objective and multiple-objective functions. The main advantage of this approach is its capacity to generate robust and reliable designs while minimizing the number of required simulation runs. This characteristic enhances its efficiency, making it a versatile, economical, and simple method for identifying optimal solutions in engineering applications.

This study also proposes a novel approach by integrating ribbed Coanda surfaces into a fluidic oscillator to examine their impact on the heat transfer rate of a heated surface through sweeping jet impingement. The dimensions of the inlet and outlet throats remain consistent across all designs. Additionally, the effects of varying Reynolds number, jet-to-target surface distance, and target surface length on heat transfer performance are examined. The results of the novel oscillator design heat transfer study are compared to the results of a smooth Coanda surface oscillator. The Taguchi optimization method is employed to systematically optimize the heat transfer performance of the fluidic oscillator system used in the current study. The findings aim to provide insights into optimizing heat transfer for ribbed oscillators and to explain the relationship between oscillation frequency and heat transfer enhancement. The increased frequency and jet spread angle enhance the cooling rate and increase the effective cooling area in sweeping jet impingement. A higher jet frequency improves coolant mixing with the hot boundary layer, increasing heat transfer, while a wider jet spread angle ensures better surface coverage, enabling more uniform cooling. These improvements significantly enhance heat transfer performance in critical applications such as turbine blade cooling systems.

Chapter 3

Numerical Methodology

3.1 Flow Domain Configuration

The SWJ (Sweeping Jet) oscillator exhibits a geometric layout similar to previous computational studies as outlined in [83, 85, 140, 149, 150]. A geometry of the oscillator and its 2D computational domain can be observed in Fig. 3.1. The SWJ oscillator comprises curved geometry having a mixing chamber, a nozzle for outlet flow, and two feedback channels. The throat size of the exit nozzle, denoted by D, serves as the length scale. In this study, the exit nozzle throat diameter D is 6.35mm. The feedback channel along with maximum mixing chamber widths are 7.43mm and 21.52mm, respectively. The mixing chamber inlet width is 10.47mm and its length is 25.79mm.

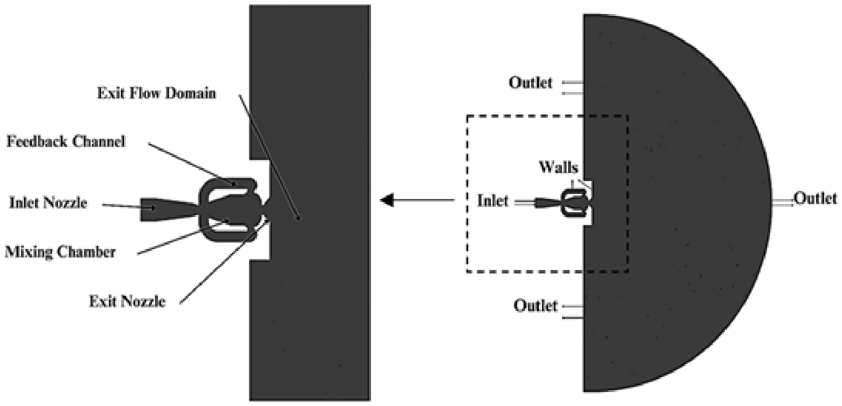

Figure 3.1: Fluidic oscillator and domain details with boundary conditions

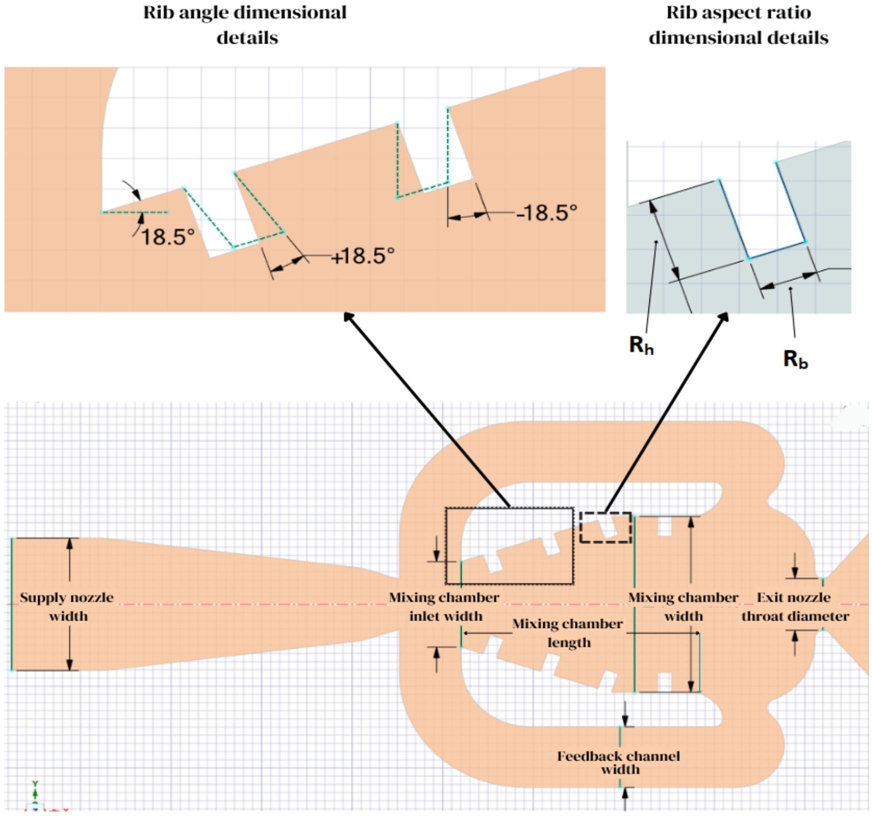

FIGURE 3.2: Detailed ribbed oscillator geometry used in the present study.

Fig. 3.2 shows ribbed oscillator with details of the aspect ratio of the rib and the angle of the rib. Aspect ratio of the rib is the ratio of its height to base, $\mathrm{AR}_{\mathrm{ribs}} = R_h/R_b$ and the angle of the rib is decided on the basis of the Coanda surface angle to the inlet flow direction, 18.5°. The angle of the rib is 0° when the rib's base is parallel to the Coanda surface, +18.5° when the rib is tilted in the direction of the flow and −18.5° when it is titled in opposite direction to the jet flow.

3.2 Mathematical Formulation

According to the findings presented by Kruger et al. [151], a two-dimensional analysis of the fluidic oscillator adequately captures both the qualitative and quantitative aspects of the flow field and its dynamic behavior. Consequently, the Unsteady Reynolds-Averaged Navier-Stokes (URANS) equations in two dimensions were utilized to model the flow characteristics within and around the fluidic oscillator. These equations govern the conservation of mass, momentum, and energy, as outlined in Eqs. (3.1), (3.2), and (3.3). The Shear Stress Transport (SST) k–ω turbulence model turbulence model, introduced by Menter et al. [152], was applied to compute the Reynolds stress component in the momentum equation, as detailed in Eqs. (3.4) and (3.5).

3.2.1 Continuity Equation

$$\frac{\partial \rho}{\partial t} + \frac{\partial (\rho u_i)}{\partial x_i} = 0 \tag{3.1}$$

3.2.2 Momentum Equation

$$\frac{\partial (\rho u_i)}{\partial t} + \frac{\partial (u_i u_j)}{\partial x_j} = -\frac{\partial P}{\partial x_i} + \frac{\partial \tau_{ij}}{\partial x_j} + \frac{\partial}{\partial x_j}\left(\mu \frac{\partial u_i}{\partial x_j}\right) \tag{3.2}$$

In Eq. (3.2), τ_{ij} denotes the stress tensor and equals $-\overline{\rho u_i'' u_j''} = 2\mu_t S_{ij}$, where S_{ij} denotes the strain tensor's mean rate.

3.2.3 Energy Equation

$$\frac{\partial (\rho c_p T)}{\partial t} + \frac{\partial (\rho c_p u_j T)}{\partial x_j} = \frac{\partial}{\partial x_j}\left(\lambda \frac{\partial T}{\partial x_j}\right) - \tau_{ij}\frac{\partial u_i}{\partial x_i} + S_i \tag{3.3}$$

3.2.4 k Equation

$$\frac{\partial (\rho k)}{\partial t} + \frac{\partial (\rho k u_j)}{\partial x_j} = \frac{\partial}{\partial x_j}\left(\left(\mu + \frac{\mu_t}{\sigma_k}\right)\frac{\partial k}{\partial x_j}\right) + \left(\tau_{ij} S_{ij} - \frac{2}{3}\rho k \frac{\partial u_i}{\partial x_j}\delta_{ij}\right) - \beta^* \rho k \omega \tag{3.4}$$

3.2.5 ω Equation

$$\begin{aligned}\frac{\partial(\rho\omega)}{\partial t}+\frac{\partial(\rho\omega u_j)}{\partial x_j}=&\frac{\partial}{\partial x_j}\left(\left(\mu+\frac{\mu_t}{\sigma_{\omega,1}}\right)\frac{\partial\omega}{\partial x_j}\right)+\gamma_2\left(2\rho S_{ij}S_{ij}-\frac{2}{3}\rho\omega\frac{\partial u_i}{\partial x_j}\delta_{ij}\right)\\&-\beta_2\rho\omega^2+\frac{2\rho}{\sigma_{\omega,2}}\frac{\partial k}{\partial x_k}\frac{\partial\omega}{\partial x_k}\end{aligned}\tag{3.5}$$

The constant parameters $\sigma_{\omega,1}$ and μ_t were incorporated into a combined function, which is effective for modeling both near-wall and far-field regions. The remaining coefficients, namely σ_k, β^*, $\sigma_{\omega,2}$, γ_2, and β_2, were assigned values of 2.0, 0.009, 1.17, 0.44, and 0.083, respectively. The foundational framework for the k-ω (SST) turbulence model, including the definition of μ_t, was established by Launder and Sandham [153], who outlined its theoretical and practical principles and defined as Eq. (3.6)

$$\mu_t=\frac{a_1k}{\max(a_1\omega,SF_2)}\tag{3.6}$$

In the context of turbulence modeling, k represents the kinetic energy associated with turbulent motion, while ω denotes the specific dissipation rate. The constant a_1 is assigned a value of 0.31, and the function F_2 takes on a value of 0 within the boundary layer and transitions to 1 in regions characterized by free shear layer flow. Consequently, the Nusselt number (Nu) can be determined on the hot target surface using the following Eq. (3.7), as referenced [154].

$$Nu=\frac{q}{(T_s-T_{\text{ref}})}\frac{D}{\lambda}\tag{3.7}$$

The reference temperature, denoted as T_{ref}, corresponds to the fluid temperature at the inlet of the fluidic oscillator, with a value of 300 K. The heat flux applied to the wall is represented by q, and T_s represents the hot target surface temperature with a value of 400 K. The area-averaged Nusselt number was calculated directly on the target surface using ANSYS Fluent post-processing tools.

The turbulence model k-ω SST (Shear Stress Transport), which incorporates turbulent kinetic energy (k) and the specific dissipation rate (ω), is used to model the turbulent viscosity μ_t. Compared to conventional k-ε and k-ω models, the SST model more effectively captures turbulence near the wall as well as in regions far from it. The SST model blends k-ω and k-ε formulations, enhanced by a shear stress limiter to improve free-stream predictions. This addresses k-ε's limitations in adverse pressure gradients and k-ω's freestream sensitivity [152]. This model is selected for the numerical analysis of the fluidic oscillator in the present study due to its capability to handle adverse pressure gradients and accurately capture wall shear stress. To ensure computational precision, the wall y+ value is maintained below 1 (0.2), ensuring accurate shear stress representation at the wall interface. The SST model's detailed approach improves understanding of fluid dynamics and ensures reliable simulation results for engineering applications. While the results provide valuable insights into the influence of ribbed Coanda surfaces on oscillator performance, the 2D computational approach, as supported by Kruger et al. [151], simplifies the geometry and may not capture three-dimensional effects. Additionally, the RANS turbulence model, though efficient, may not fully resolve transient and highly turbulent flow features. These limitations highlight opportunities for further exploration using advanced techniques.

3.2.6 Characterization of Fluidic Oscillator Performance Parameters

This section illustrates how the key output parameters, the oscillation frequency of the jet, the deflection angle of the jet, and the pressure drop across the fluidic oscillator are determined during this study. Fig. 3.3 illustrates the details for determining the oscillation frequency of the jet, the deflection angle of the jet, and the pressure drop across the fluidic oscillator. The oscillation frequency is defined as the number of jet oscillation cycles completed per second, where a jet oscillation cycle corresponds to the jet returning back to its initial position after completing a full oscillation. To accurately determine the oscillation frequency of

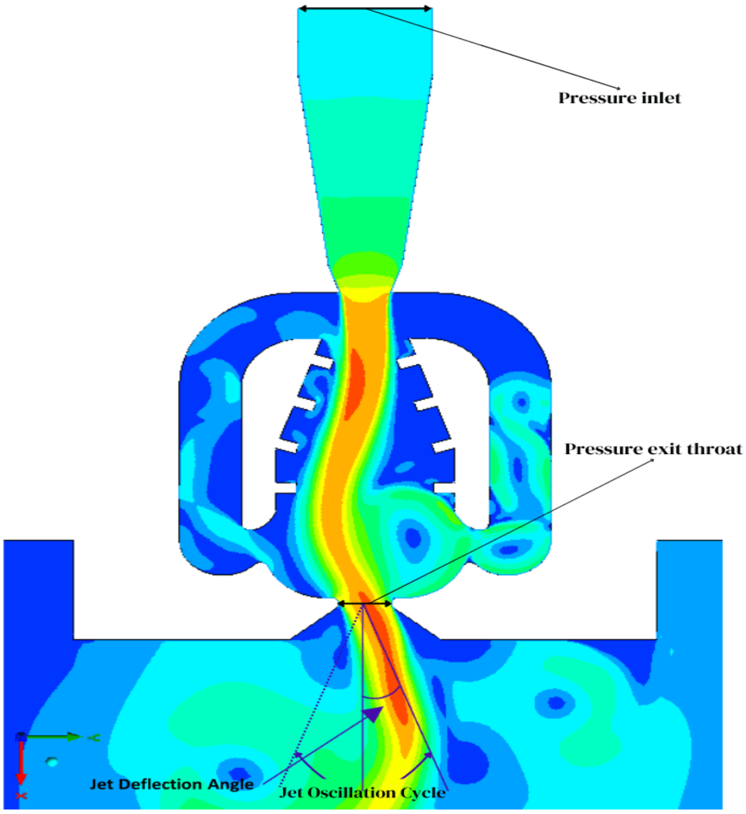

FIGURE 3.3: Oscillation frequency, deflection angle, and pressure drop calculation details

the fluidic oscillator, time-resolved velocity magnitude data is collected at a probe point positioned 6 mm directly downstream from the oscillator exit. This specific location is chosen to effectively capture the periodic fluctuations in the jet flow induced by the oscillator geometry. The recorded velocity signal is then subjected to a Fast Fourier Transform (FFT) analysis, which decomposes the time-domain data into its frequency components. The dominant peak in the resulting frequency spectrum corresponds to the primary oscillation frequency of the jet flow.

To calculate the jet deflection angle θ, the jet half-width δ is first determined. The jet half-width represents the distance between $y = 0$ (centreline) and the point where $U_{\text{avg}}(y) = 0.5\,U_{\max}$. Using the calculated jet half-width, the deflection or spreading angle can be obtained using $\theta = \tan^{-1}(\delta/x)$, where $x = 3D$ is the axial distance from the exit of the fluidic oscillator in the flow direction. Additionally, the pressure drop is calculated as the difference in pressure between the inlet and the exit nozzle throat.

3.2.7 Flow Performance Evaluation Parameters

For the flow performance evaluation of the fluidic oscillators of different geometries based on the placement of ribs with different aspect ratios on the Coanda surface, six non-dimensional performance parameters are defined namely; the peak velocity ratio of the sweeping jet, the dimensionless pressure drop across the fluidic oscillator, the frequency-pressure ratio, Strouhal number, the jet deflection angle-pressure ratio, and the frequency jet deflection-pressure ratio of the oscillator. The peak velocity ratio F_{VR} is used to enhance the peak velocity of the leaving jet at the oscillator exit [155] and is defined as follows in Eq. (3.8)

$$F_{VR} = \frac{V_{\text{peak}}}{V_i} \tag{3.8}$$

Where V_i is the inlet velocity and V_{peak} is the peak or maximum velocity of the jet at the exit throat of the oscillator. The dimensionless pressure drop F_f is the next performance parameter [76] used and defined through Eq. (3.9)

$$F_f = \frac{\Delta p \cdot D}{2\rho V_i^2 S_2} \tag{3.9}$$

Here Δp denotes the pressure drop across the oscillator, D is the exit nozzle throat diameter and S_2 represents the spacing between the inlet and exit nozzle throat. The pressure drop has a direct impact on the amount of pumping power needed to move the fluid across the oscillator. The performance parameter frequency-pressure ratio (FPR) is used for the oscillator to increase its oscillation frequency and is expressed in Eq. (3.10)

$$\text{FPR} = \frac{f_e/f_s}{(\Delta p_e/\Delta p_s)^{1/3}} \tag{3.10}$$

Where f_s is the frequency, Δp_s is the pressure drop of the smooth case (no ribs) and f_e is the frequency, Δp_e is the pressure drop of the enhanced case (with ribs).

The Strouhal number expressed in Eq. (3.11) is defined as a ratio of the product of jet oscillating frequency (f) and nozzle exit diameter (D) to the exit velocity of the jet (V_{exit}). Where f is the jet oscillation frequency, D is the exit nozzle throat diameter, and time-averaged velocity at the exit nozzle (V_{exit}).

$$St = \frac{f \cdot D}{V_{\text{exit}}} \tag{3.11}$$

The performance parameter jet deflection-pressure ratio (JDPR) is defined and expressed as follows in Eq. (3.12):

$$\text{JDPR} = \frac{\theta_e/\theta_s}{(\Delta p_e/\Delta p_s)^{1/3}} \tag{3.12}$$

Where θ_s is the jet deflection angle of the smooth case (no ribs) and θ_e is the jet deflection angle of the enhanced case (with ribs).

The last performance parameter is the frequency jet deflection-pressure ratio (FDPR) which is defined in Eq. (3.13):

$$\text{FDPR} = \frac{f_e/f_s \cdot \theta_e/\theta_s}{(\Delta p_e/\Delta p_s)^{1/3}} \tag{3.13}$$

3.3 Boundary Conditions and Discretization Schemes

The numerical simulations in this study were conducted using Ansys-Fluent 2022 to analyze the fluid flow and heat transfer characteristics of the fluidic oscillator system. The working fluid, air, was modeled as a two-dimensional, unsteady, and incompressible flow. The Unsteady Reynolds-Averaged Navier-Stokes (URANS) equations were solved to capture the transient behavior of the system, with turbulence effects accounted for using the Shear Stress Transport (SST) k-ω model. A pressure inlet boundary condition was employed, to study the system's flow and thermal performance. The target surface was maintained at a constant temperature of 400 K, simulating a high-temperature heat source.

This approach allowed for a detailed analysis of the convective cooling effectiveness of the oscillating jet under different operating conditions. The walls of the fluidic oscillator were modeled with a no-slip boundary condition, ensuring that the velocity components in both the x and y directions were set to zero at the wall surfaces. Additionally, the inlet (reference for the fluid properties) and the walls of the oscillator were maintained at a constant temperature of 300 K, providing a well-defined thermal boundary condition for the simulations. A second-order implicit scheme was used for temporal discretization to ensure numerical stability and accuracy.

The pressure-velocity coupling was resolved using the SIMPLE algorithm, which iteratively solves the equations of continuity and momentum to attain a pressure corrective field. The convective terms in the equations of momentum, turbulent kinetic energy, and specific dissipation rate were discretized through a second-order upwind scheme to minimize numerical diffusion and enhance solution accuracy. To attain a fully developed sweeping jet, the computational model was run for 10^{+4} time-steps, with each time step carefully selected to resolve the high-frequency oscillations of the jet. Convergence was monitored by tracking the residuals of all governing equations, with a convergence criterion of 10^{-6} or each variable. To ensure statistical reliability, time-averaged data were collected over 10,000 time steps after achieving a fully developed oscillating jet. This approach minimized the influence of initial transients and provided representative results for fluid flow and heat transfer analysis.

3.4 Time-step Sensitivity

A comprehensive time-step sensitivity study is conducted to ensure solution accuracy. Simulations are performed at different time steps as presented in Table

3.1. It can be observed from the results that reducing the time step below 7.5 µs resulted in 0.003% change in the oscillation frequency, indicating that further refinement is unnecessary. To balance computational efficiency with accuracy, a 5.0 µs time-step size is chosen for all subsequent simulations.

TABLE 3.1: Time-step sensitivity analysis for different time-step sizes

Time-step size (µs)	**Time interval for data saving (ms)**	**Frequency (Hz)**	**Percentage change in frequency**
10.0	50	355.55	0.101%
7.5	50	355.42	0.065%
5.0	50	355.19	–
2.5	50	355.18	(0.003%)

3.5 Grid Independence and Model Validation

3.5.1 Grid Independence

A grid independence study was conducted to assess the impact of domain discretization on the numerical results. In this investigation, four distinct computational grids were generated utilizing the meshing functionalities of Ansys Fluent (version 2021), as illustrated in Fig. 3.4. The primary criterion for grid construction was the throat diameter (D = 6.35 mm) of the nozzle exit. To ensure precise resolution of the near-wall boundary layer, low y^+ values, and capture wall shear stress and heat transfer gradients reliably, 20 layers were established perpendicular to the wall surface of fluidic oscillator and target surface. The initial layer thickness was configured at D/500, with a growth factor of 1.15 applied to the subsequent layers. Mesh refinement was achieved through the sphere of influence technique, employing radii of 20D. The mesh types and their corresponding element sizes and frequencies are as follows: The coarse mesh (N20) had an element size of D/20 and the normal mesh (N40) featured an element size of D/40. The fine mesh (N60) was

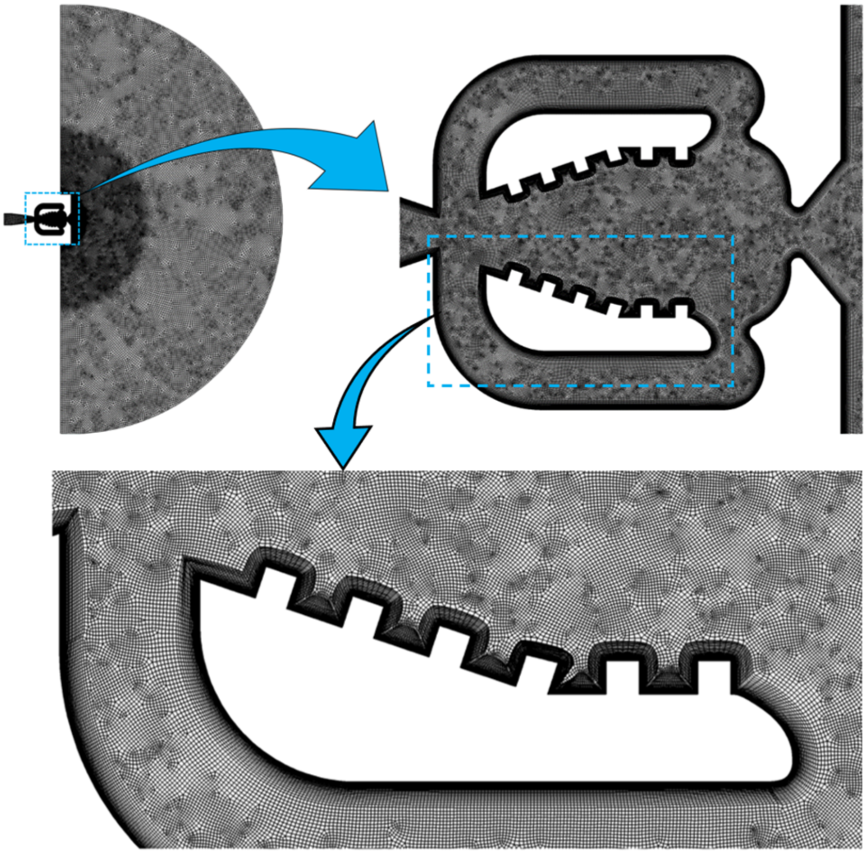

FIGURE 3.4: Detailed mesh used in the present study

constructed with an element size of D/60 and finally, the finer mesh (N80) had an element size of D/80.

A mesh sensitivity assessment was performed to examine the effect of grid refinement on the primary output variable, oscillation frequency. This evaluation employed static local mesh refinement using the sphere of influence method to compare outcomes across varying grid densities. Fig. 3.5 illustrates the findings derived from the Fast Fourier Transform (FFT) evaluation carried out on multiple grid resolutions, ranging from coarse to finer configurations. The dominant frequency peaks observed in the graphical representations correspond to the N20, N40, N60, and N80 grids, with measured values of 340 Hz, 355 Hz, 358 Hz, and 357 Hz, respectively.

To assess numerical precision, the relative percentage variation in frequency between successive grid refinement levels was calculated. As indicated in Table 3.2, the frequency values stabilize for grid densities exceeding N40, with deviations remaining under 1%. This implies that additional refinement beyond N40 provides minimal enhancement in accuracy. Therefore, using the static local mesh refinement using the sphere of influence method, the N40 grid was selected for further analysis, as it represents an optimal balance between computational efficiency and result accuracy. This grid independence validation confirms that the selected grid density is adequate for accurately capturing critical characteristics within the simulation domain.

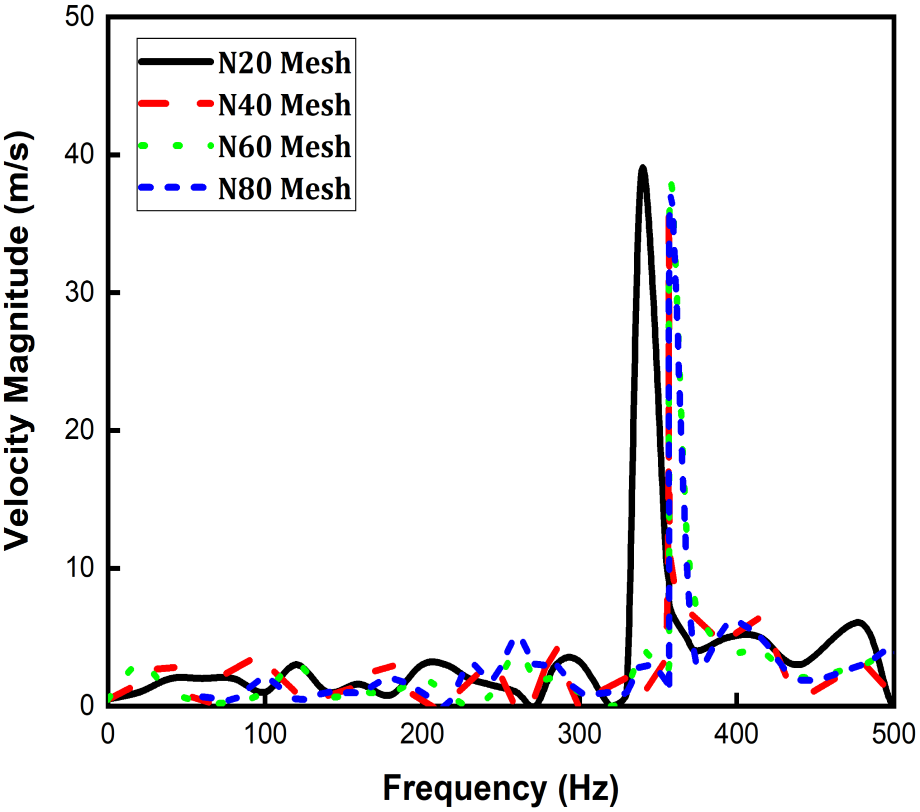

Figure 3.5: FFT results for the different meshes used in the grid independence study

3.5.2 Validation

To validate the computational approach used in the present study, an extensive validation procedure was carried out. For the flow analysis, the results achieved by

Table 3.2: Percentage change in frequency at different mesh refinement levels

Levels of mesh refinement	**Change in frequency**	**Percentage change**
N20 mesh to N40 mesh	340 Hz to 355 Hz	4.41%
N40 mesh to N60 mesh	355 Hz to 358 Hz	0.85%
N60 mesh to N80 mesh	358 Hz to 357 Hz	0.28%

the current numerical method were compared with the numerical data provided by Jurewicz and Kara [150]. The oscillation frequency analysis, employing the Fast Fourier Transform (FFT) for the velocity profile downstream of the nozzle exit, as illustrated in Fig. 3.6(a), reveals a high degree of correlation with the findings from [150].

Additionally, the frequency results obtained in this research were validated against experimental data from Slupski et al. [140], the two-dimensional computational study by Kara [149], the three-dimensional simulations by Oz and Kara [83], and the two-dimensional numerical investigations by Alam and Kara [85], as presented in Fig. 3.6(b).

The discrepancies relative to both experimental and computational outcomes were quantified at 0.3%, 2.6%, 1.2%, -1.4%, and 2.6%, respectively as presented in Table 3.3.

Fig. 3.7(a) includes validation of the jet deflection angle, showing present study result of 54.4° compares well with the experimental value of 56.2° from Tajik et al. [81], representing a 3.2% error. The close agreement demonstrates the reliability of present simulation approach.

For heat transfer analysis, the results of the current numerical investigation were evaluated against the combined computational and experimental work of Joulaei et al. [141].

Fig. 3.7(b) contrasts the time-averaged Nu derived from the present numerical approach with the computational and experimental results of Joulaei et al. [141],

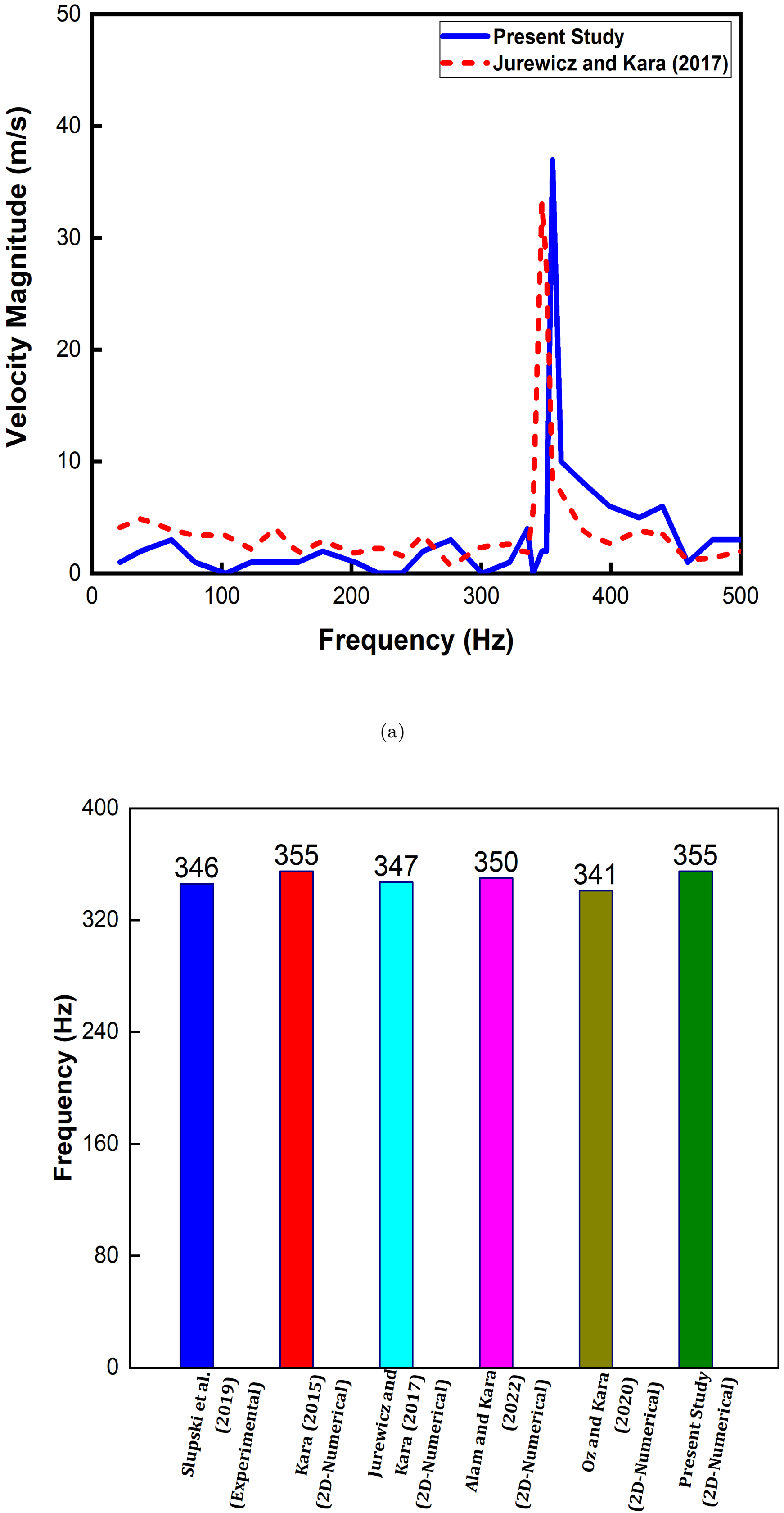

(a)

(b)

FIGURE 3.6: Validation results of the present study with results from literature for (a) Velocity magnitude FFT (b) Oscillation frequency

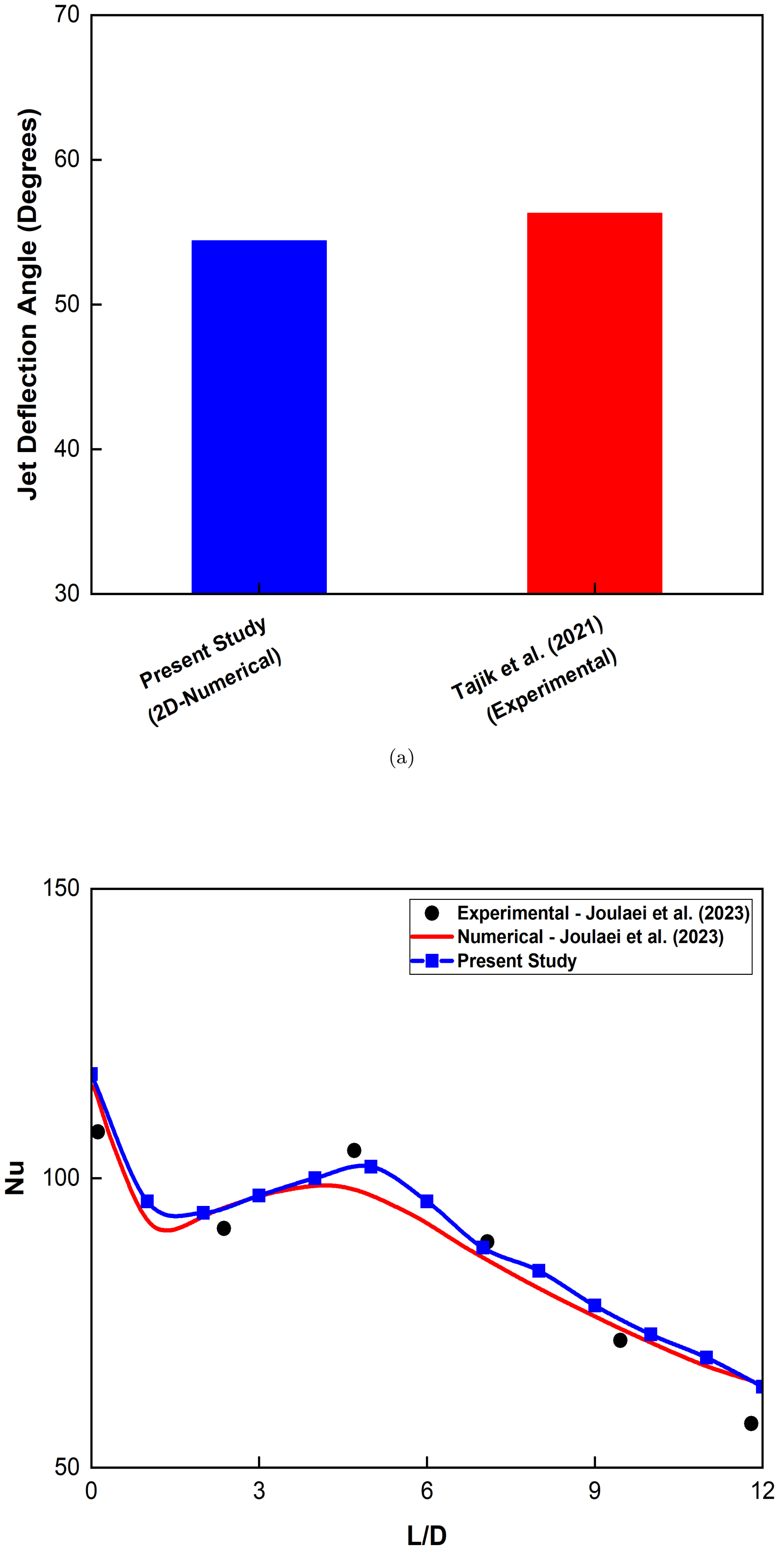

(a)

(b)

FIGURE 3.7: Validation results of the present study with results from literature for (a) Jet deflcetion angle and (b) Nu

TABLE 3.3: Model validation for the present study

Ref.	**Analysis type**	**Oscillation frequency**	**Error**
Slupski et al. [140]	Experimental	346 Hz	–
Jurewicz and Kara [150]	2D-numerical	347 Hz	0.3%
Alam and Kara [85]	2D-numerical	350 Hz	1.2%
Oz and Kara [83]	3D-numerical	341 Hz	-1.4%
Present study	2D-numerical	355 Hz	2.6%

demonstrating a strong level of agreement. The maximum deviation between the current numerical study and the referenced computational study is approximately 7%, while the difference with the experimental data is less than 2%, observed at L/D = 5.

Consequently, the reliability of the present numerical results is substantiated by both computational and experimental findings from the existing literature.

3.6 Optimization Methodology

3.6.1 Optimization Design Objectives and Solution Methodology

The goal of this study is the performance improvement of a fluidic oscillator by optimizing the key flow performance characteristics of oscillating frequency, deflection angle of the jet, and pressure drop. The solution strategy involves using the Taguchi method for single objective optimization of performance parameters obtained through CFD simulations and an integrated approach combining CFD simulations, the Taguchi method, and the Grey Relational Analysis. The process is structured in two phases:

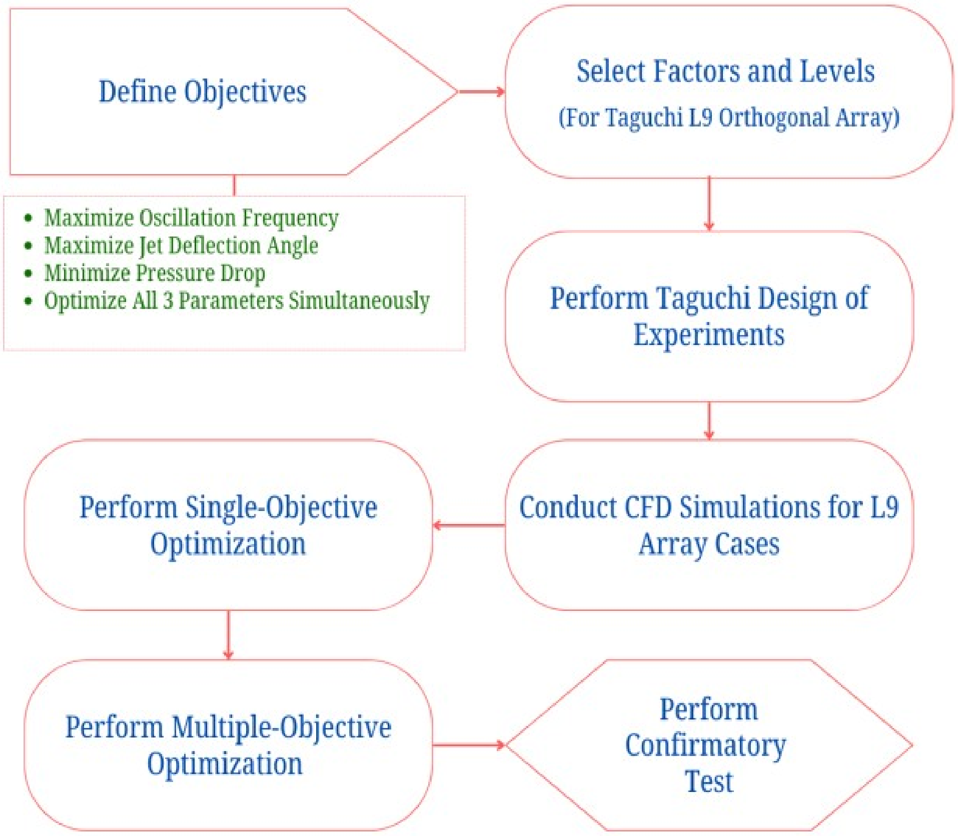

FIGURE 3.8: Design Objective and Solution Strategy Flow Chart

Single Objective Optimization: Each output (frequency, deflection angle, and pressure drop) is optimized individually using the Taguchi method.

Multi-Objective Optimization: A combined optimization of all three outputs using Weighted GRA-Taguchi.

A flow diagram summarizing the solution strategy is provided in Fig. 3.8.

3.6.2 Design of Experiment

DOE analysis is performed using Minitab V.21 software. The DOE analysis includes four phases: (1) planning, (2) characterization, (3) optimization, and (4) verification. The multiple-objective optimization is achieved through an integrated CFD-Taguchi- approach.

3.6.3 Taguchi Design

The Taguchi design method serves as an effective experimental approach for system optimization, employing structured orthogonal arrays to facilitate multi-parameter design optimization. Within this framework, various input variables, termed factors, and their associated levels are systematically organized using standard orthogonal arrays. This structured methodology significantly minimizes the number of experimental trials required compared to full-factorial designs.

The primary goal of the present study is to determine the most effective set of geometric parameters associated with ribs installed on a Coanda surface for performance improvement of the fluidic oscillator system.

To achieve this, the signal-to-noise (S/N) ratio has been employed as the objective function in the experimental design. Generally, the analysis focuses on three types of performance characteristics: smaller the better, larger the better, and nominal the better. Accordingly, three corresponding S/N ratios are utilized based on the chosen performance characteristic in the optimization problem.

The smaller-the-better performance characteristic is applied to minimize the response variable. The signal-to-noise (S/N) ratio for this category is calculated using Eq. 3.14:

$$\frac{S}{N} = -10\log\left(\frac{1}{n}\sum_{i=1}^{n} y_i^2\right) \tag{3.14}$$

The larger-the-better performance characteristic is used to maximize the response variable. The signal-to-noise (S/N) ratio for this category is found through Eq. 3.15:

$$\frac{S}{N} = -10\log\left(\frac{1}{n}\sum_{i=1}^{n} \frac{1}{y_i^2}\right) \tag{3.15}$$

The nominal-the-better performance characteristic is applied when the target value is a specific nominal value. The S/N ratio for this category is calculated using Eq. 3.16:

$$\frac{S}{N} = 10 \log \left(\frac{\bar{y}^2}{s^2} \right) \tag{3.16}$$

In the above equations, y_i represents the ith observed objective value from the Taguchi trial runs, n is the number of observations in a trial run, $\bar{y}$ is the mean of the performance characteristic, and s^2 represents the variance.

The current research aims to identify the optimal combination and associated values of ribs installed on the Coanda surface of the double feedback oscillator, including the aspect ratio of the ribs, the number of ribs, and the angle of the ribs.

3.6.4 Taguchi Control Factors and Levels

In the Taguchi method, control factors and their respective levels are carefully selected to evaluate the influence of different parameters on system performance. In this case, three control factors: rib aspect ratio, number of ribs, and rib angle, were each tested at three levels.

An orthogonal array L9 (3^3) was employed to efficiently design the simulation experiments, ensuring a balanced and systematic variation of parameters across nine simulation runs. This approach allows for a comprehensive analysis of each factor's impact while minimizing the number of experiments required.

3.6.5 Weighted Grey Relational Analysis

Grey relational analysis, a prominent framework within the Grey-system theory, was originally introduced by Deng [156].

This methodology characterizes scenarios as black when information is fully missing and white when information is completely available. Nevertheless, such absolute scenarios are rarely encountered in practical applications. While grey represent the situation when incomplete or partial information are available.

An adaptation of this model, known as the Taguchi-based GRA, has gained considerable attention in contemporary engineering research. In fluidic oscillator design, achieving a multi-objective target is crucial.

To address the constraints associated with the Taguchi method, which focuses on a single response, the GRA approach is utilized to transform multi-objective challenges into a single-objective optimization framework.

The optimization criteria employed include larger is better for both the oscillating frequency and deflection angle and smaller is better for the pressure drop. Weighted Grey Relational Analysis (WGRA) technique is used to evaluate and compare multiple alternatives based on various criteria.

It integrates the concept of grey system theory and incorporates weights for each criterion to prioritize their importance in the analysis. Following are the key steps and relevant equations for Weighted Grey Relational Analysis.

For the larger-the-better case, the normalized value for each alternative i and criterion j is calculated using Eq. 3.17:

$$x'_{ij} = \frac{x_{ij} - x_j^{\min}}{x_j^{\max} - x_j^{\min}} \tag{3.17}$$

While for the smaller-the-better case, the normalized value for each alternative i and criterion j is computed using Eq. 3.18:

$$x'_{ij} = \frac{x_j^{\max} - x_{ij}}{x_j^{\max} - x_j^{\min}} \tag{3.18}$$

Where x_{ij} is the initial value of the criterion, $x_j^{\min}$ and $x_j^{\max}$ are the minimum and maximum values for the jth criterion across all alternatives.

The formula scales the values between 0 (minimum) and 1 (maximum).

The grey relational coefficient (GRC) for each alternative is calculated to measure its similarity to the ideal solution. The grey relational coefficient ξ_{ij} is calculated using Eq. 3.19:

$$\xi_{ij} = \frac{\Delta_{\min} + \zeta \cdot \Delta_{\min}}{\Delta_{ij} + \zeta \cdot \Delta_{\min}} \tag{3.19}$$

Where Δ_{ij} is the absolute change between the normalized value of alternative i and the reference value for criterion j, $\Delta_{\min}$ is the minimum change across all alternatives and criteria, $\Delta_{\max}$ is the maximum change across all alternatives and criteria, and ζ represents the distinguishing coefficient (value ranges from 0 to 1 but mostly taken as 0.5).

To incorporate the importance of each criterion, the grey relational coefficient is multiplied by the weight of the respective criterion.

The weighted grey relational coefficient for each alternative is calculated using Eq. 3.20:

$$\xi_{ij}^{w} = w_j \cdot \xi_{ij} \tag{3.20}$$

Where w_j is the jth criterion weight (the relative importance of the criterion).

The grey relational grade (GRG) is the total assessment score for each alternative and is calculated as the summation of the GRCs for all criteria through Eq. 3.21:

$$G_i = \sum_{j=1}^{m} \xi_{ij}^{w} \tag{3.21}$$

Where m represents the overall number of criteria and G_i is the grey relational grade for the individual alternative. The alternatives are ranked based on their grey relational grades (highest being the best).

In Grey Relational Analysis, assigning appropriate weights to performance parameters is essential for accurately evaluating grey relational grades. Several well-established methods are commonly employed for determining these weights, including the Equal Weight Method, Expert Judgment, Analytical Hierarchy Process (AHP), Entropy Method, Principal Component Analysis (PCA), Regression Analysis, and Fuzzy Logic.

Each of these methods is tailored to specific contexts, offering flexibility in addressing various decision-making scenarios.

The pairwise comparison scale utilized in the Analytical Hierarchy Process is formulated based on a systematic framework introduced by Thomas L. Saaty. This methodology enables decision-makers to systematically evaluate and express their preferences regarding the relative significance of various criteria.

The pairwise comparison matrix, denoted as A, is an $m \times m$ matrix [145]. This matrix is constructed using the Saaty scale, where the values represent the comparative scale between the responses as presented in Eq. 3.22:

$$A = \begin{bmatrix} a_{11} & a_{12} & \cdots & a_{1m} \\ a_{21} & a_{22} & \cdots & a_{2m} \\ \vdots & \vdots & \ddots & \vdots \\ a_{m1} & a_{m2} & \cdots & a_{mm} \end{bmatrix} \tag{3.22}$$

Where $a_{ii} = 1$ for all i (indicating that a criterion is equally important as itself), and $a_{ji} = 1/a_{ij}$ for reciprocal comparisons between responses.

For each response, the geometric mean (GM) is calculated using Eq. 3.23:

$$GM_i = \left(\prod_{j=1}^{m} a_{ij} \right)^{1/m} \tag{3.23}$$

The normalized weight w_j for each response is obtained by Eq. 3.24:

$$w_j = \frac{GM_i}{\sum_{i=1}^{m} GM_i} \tag{3.24}$$

For checking the consistency of the comparisons, the consistency index (CI) is calculated through Eq. 3.25:

$$CI = \frac{\lambda_{\max} - m}{m - 1} \tag{3.25}$$

Here $\lambda_{\max}$ represents the maximum eigenvalue of the matrix. The consistency ratio (CR) is then calculated using Eq. 3.26:

$$CR = \frac{CI}{RI} \tag{3.26}$$

Here, RI is the random index based on the matrix size. A CR of 0.1 or less shows that consistency is acceptable; otherwise, the matrix requires revision.

The AHP pairwise comparison Saaty scale ranges from 1 to 9, offering the following interpretations for decision-making as shown in Table 3.4.

TABLE 3.4: Saaty scale details for AHP pairwise comparison

Scale Number	**Scale Significance**	**Contribution**
1	Equal significance	Both elements contribute equally to achieving the objective.
3	Moderate significance	One element is to some extent more preferred based on experience or judgment.
5	Strong significance	One element is strongly preferred based on experience or judgment.
7	Very strong significance	The preference for one element is evident and well-demonstrated.
9	Extreme significance	The evidence supporting one element's dominance is conclusive.
2, 4, 6, 8	Intermediate values	Nuanced judgments between the primary levels.

The structured prioritization afforded by this scale ensures that the optimization process accurately reflects these preferences, leading to more effective and meaningful results.

The Taguchi-GRA method offers significant advantages over other optimization schemes, such as genetic algorithms (GA) and response surface methodology (RSM). It reduces computational costs by using orthogonal arrays.

For example, in our study, an L9 array is used requiring only 9 simulations instead of 27, saving 66.7% of resources. It is also easier to implement than GA, as it avoids complex parameter tuning. Additionally, the integration of GRA enables effective multi-objective optimization by converting multiple responses into a single grey relational grade.

Chapter 4

Flow Performance in Fluidic Oscillators: Influence of Aspect Ratio of Ribs

4.1 Introduction

This chapter presents the results of a numerical investigation examining the influence of aspect ratios of the ribs installed along the Coanda surface of a double feedback fluidic oscillator. The study aims to characterize the flow dynamics and assess the potential for enhancing oscillator performance through these novel geometric modifications in a smooth double feedback fluidic oscillator. The Coanda surface was equipped with ribs as a deliberate design choice, since surface texturing is widely recognized for promoting near-wall momentum redistribution, faster jet switching and improved flow mixing. A systematic analysis is conducted to evaluate the effects of varying rib dimensions on key flow parameters, including mainly oscillation frequency, jet deflection angle and pressure drop. The results provide insights into the enhancing of the Coanda surface features to improve the flow performance capabilities of fluidic oscillators. The main goal of the present study is to examine the variations in the most critical geometrical parameter Coanda surface of the fluidic oscillator. Five different designs of fluidic oscillators with various aspect ratios of ribs installed over the Coanda surface are studied. The influence of the variation in aspect ratio of the ribs installed over the Coanda surface on six nondimensional performance parameters; the peak velocity ratio of the sweeping jet, the dimensionless pressure drop through the fluidic oscillator, the frequency-pressure ratio, Strouhal number, the jet deflection angle-pressure ratio and the frequency jet deflection-pressure ratio of the oscillator is evaluated. The highest combined effect of frequency and jet spreading angle is found for the fluidic oscillator design using the SST turbulence model.

4.2 Problem Formulation

As discussed, in this study, we have modified the Coanda surface by adding ribs over it. We studied 5 different geometries of the fluidic oscillator having different sizes of ribs over the Coanda surface and a smooth oscillator as shown in Fig. 4.1 and Table 4.1. Initially, square ribs with 0.25D length (where D is the Fluidic Oscillator's exit nozzle throat diameter), having aspect ratio = 1 were added on the Coanda surface. The aspect ratio of the ribs, ARribs is defined as the ratio of the rib's height (Rh) to the rib's base (Rb).

TABLE 4.1: Details of different geometries investigated in the present study

Case	**No. of ribs**	**Height (mm)**	**Base (mm)**	**Aspect ratio**	**Gap (mm)**	**Total area ($\mathbf{mm^2}$)**
Case $\mathrm{AR_{ribs}}$=0	0	–	–	–	–	–
Case $\mathrm{AR_{ribs}}$=0.64	6	1.28	2.00	0.64	2.46	15.36
Case $\mathrm{AR_{ribs}}$=0.81	6	1.44	1.78	0.81	2.68	15.36
Case $\mathrm{AR_{ribs}}$=1.00	6	1.60	1.60	1.00	2.86	15.36
Case $\mathrm{AR_{ribs}}$=1.23	6	1.78	1.44	1.23	3.02	15.36
Case $\mathrm{AR_{ribs}}$=1.56	6	2.00	1.28	1.56	3.18	15.36

The length of the height and the base of the ribs were modified in such a way that the total area of the ribs remains constant as shown in Table 5. In this way when the height of the ribs was reduced from 0.25D to 0.225D and then 0.2D, aspect ratios of 0.81 and 0.64 were attained respectively. In the next phase, the base of the

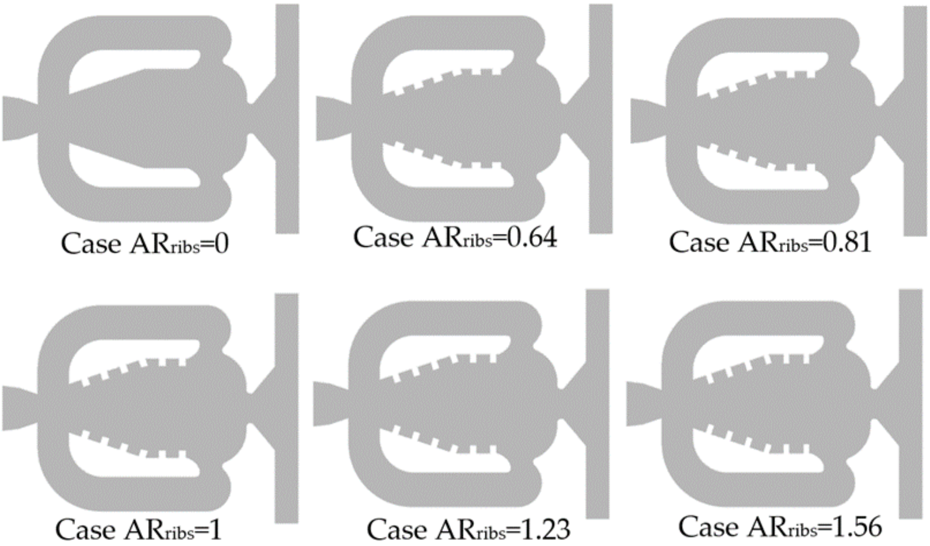

Case AR_{ribs}=0 Case AR_{ribs}=0.64 Case AR_{ribs}=0.81

Case AR_{ribs}=1 Case AR_{ribs}=1.23 Case AR_{ribs}=1.56

FIGURE 4.1: Fluidic oscillator with different Coanda surface configurations

ribs was modified from 0.25D to 0.225D and 0.2D, attaining aspect ratios of 1.23 and 1.56 respectively. The gap represents the distance between two consecutive ribs.

4.3 Results and Discussions

The fluidic oscillator enables the production of a spanwise oscillating jet with bi-stable behavior at the exit. To evaluate the efficiency of the fluidic oscillator in active flow control and cooling heated surfaces, two important output parameters; oscillation frequency and the jet deflection angle are used.

The oscillation frequency plays a significant role in determining the uniformity of the cooling process on a heated surface. On the other hand, the deflection angle of the jet has a direct impact on the spreading of the jet, influencing the coverage area and, consequently, the effectiveness of the cooling mechanism.

In essence, these two parameters, the oscillation frequency, and the deflection angle, are instrumental in optimizing the performance of the fluidic oscillator for efficient cooling of heated target surfaces.

In the current study, modifications were made to the Coanda surface of the oscillator to improve its performance by enhancing the combined effect of oscillation frequency and jet spreading.

4.3.1 Effects of Coanda Surface Ribs on Internal Flow Dynamics of the Oscillator

The effect of the ribs placed over the Coanda surface on the internal flow dynamics, oscillation frequency, jet spreading, and pressure drop of fluidic oscillators were examined for all the variations in fluidic oscillators' geometries as presented in Table 4.1. As the jet enters the mixing chamber of the fluidic oscillator through the inlet nozzle, even a slight disturbance in the flow causes an uneven pressure distribution on the mixing chamber walls. This phenomenon causes the flow attachment to one side is known as the Coanda effect. The Coanda effect intensifies as the jet advances towards one of the walls, eventually attaching itself there completely. The phase angle $\phi = 0°$ signifies this moment and the jet entering the oscillator and leaving it are in phase and the jet at the exit throat remains undeflected as shown in Fig. 4.2.

A segment of the jet stream diverts into the feedback loop and travels back to the fluidic oscillator's main flow. The flow from feedback inserts itself between the primary jet and the wall, pushing the main jet away from the wall until it attaches to the opposite side which represents the phase angle $\phi = 180°$. The phase angles 0°, 45°, 90°, 135° and 180° cover half an oscillation period of the sweeping jet. This cycle repeats on the opposite side, creating a self-sustained jet oscillation. Meanwhile, the ejecting angle of the jet at the exit nozzle leads to its deflection within the external flow field. After the internal deflection, the jet starts sweeping in the external flow field.

The streamline plots for Case ARribs=0, Case ARribs=0.64, Case ARribs=1, and Case ARribs =1.56 are presented in Fig. 4.2. It is shown in Fig. 4.2 that initially at phase angle $\phi = 0°$ when the jet flows into the mixing chamber and attaches

FIGURE 4.2: Streamline plots highlighting the effect of ribs on the formation of separation bubbles at different phase angles for different aspect ratios of ribs placed over the Coanda surface

to one side of the Coanda surface, a primary separation bubble is formed in the mixing chamber near the opposite Coanda surface in all cases. For Case ARribs=0 the size of the bubble is very large as compared to all the oscillators with ribs. It covers more than half of the area of the mixing chamber. The jet has a very narrow passage to flow through the mixing chamber. For phase angle $\phi = 0°$ the size of the primary bubble is the smallest for the highest aspect ratio Case ARribs=1.56. The placement of ribs on the Coanda surface impacts the size of the primary separation bubble.

As the jet enters the mixing chamber and hits the first rib, the jet is deflected and is not allowed to stick to the Coanda surface as in the oscillator with no ribs Case

ARribs=0. This deflected jet squeezes the primary separation bubble and forces it to reduce in size.

As the aspect ratio of the ribs increases, the height of the ribs also increases and thus the jet entering the mixing chamber is deflected at a higher angle and the primary bubble experiences greater squeezing resulting in a smaller bubble for Case ARribs=1.56. As the size of the ribs increases, the passage in the mixing chamber concurrently decreases. This results in an escalation of the jet velocity, where the higher velocity of the jet forces the bubble to compress and reduce in size. In Fig. 4.2 at phase angle $\phi = 45°$, the primary bubble still covers almost half of the area of the mixing chamber for Case ARribs=0. However, at phase angle $\phi = 45°$, the size of the separation bubble becomes significantly small in ribbed oscillators. The smallest size of the separation bubble is for the highest aspect ratio ribs Case ARribs=1.56. The location of the bubble is also lower than the Coanda surface and its width is also small. The main jet also finds a smooth bigger passage in the mixing chamber. The switching of the jet to the opposite side faces minimal resistance. Hence a higher frequency is attained with the highest aspect ratio. At higher phase angles $\phi = 90°$ and $\phi = 135°$, it can be observed that a separation bubble of the same size for all cases starts forming on the opposite side. This formation of the same size separation bubble on the opposite side is completed at phase angle $\phi = 180°$ for all cases. The flow also attaches itself to the opposite side i.e., half oscillation cycle is completed.

Fig. 4.3 (a) shows the pressure contours for phase angle of 0° for various geometries used in the study. For Case ARribs=0 at phase angle $\phi = 0°$ it can be observed that the low-pressure zone which represents the separation bubble in the mixing chamber is very large. At phase angle $\phi = 0°$ as the aspect ratio is increased i.e. Case ARribs=0.64, Case AR-ribs=1, and Case AR-ribs=1.56 the low-pressure zone representing the separation bubble inside the mixing chamber is squeezed. It can be observed for Case AR-ribs=1.56 the low-pressure zone becomes very small. It also shows that increasing the height of the ribs helps in reducing the bubble size. Fig. 4.3 (b) shows the difference in the characteristics of separation bubbles through vorticity contours at phase angle 0° for different aspect ratios of ribs installed over the Coanda surface. The jet is guided by high vorticity flow around the main jet on both sides. The high vorticity flow around the jet is pushed more in the direction of the mixing chamber's center as the aspect ratio of the ribs is increased from Case ARribs =0 to Case ARribs=1.56. For the oscillator Case ARribs=1.56 the high vorticity flow is detached from the lower half of the ribs thus pushing the jet farther towards the mixing chamber's center. This behavior of flow helps in the faster switching of the jet from one side of the Coanda surface to the other as the aspect ratio of the ribs is increased.

4.3.2 Assessment of the Influence of Ribs on Jet Oscillating Performance Enhancement

The influence of Coanda surface ribs on fluidic oscillator characteristics is thoroughly evaluated by utilizing a range of performance parameters in the subsequent sections.

4.3.2.1 Exit Velocity of the Jet and Pressure Drop

The effect of different aspect ratios of ribs on the exit velocity of the jet is assessed by employing the jet velocity ratio (F_{VR}), and non-dimensional pressure drop (F_{f}). The results in Fig. 4.4(a) show that an increase in the aspect the ratio of ribs decreases the jet velocity ratio. According to Pandey and Kim [155] with the increase in jet velocity ratio, the jet transmits higher momentum to the crossflow, and hence the effectiveness of the fluidic oscillator is increased. Therefore, in terms of jet velocity ratio, Case ARribs=0 (no ribs) is the most effective among the oscillators with the different aspect ratio ribs, Case ARribs=0.64 (the lowest aspect ratio) oscillator is the most effective. Fig. 4.4(b) shows the results of variations of dimensionless pressure drop, for various aspect ratios of the ribs placed over the Coanda surface of the oscillator.

The results show a decreasing trend in dimensionless pressure drops as the aspect ratio of the ribs increases. As the aspect ratio increases, the height of the ribs increases which leads to a detachment of the jet from the lower half of the ribs

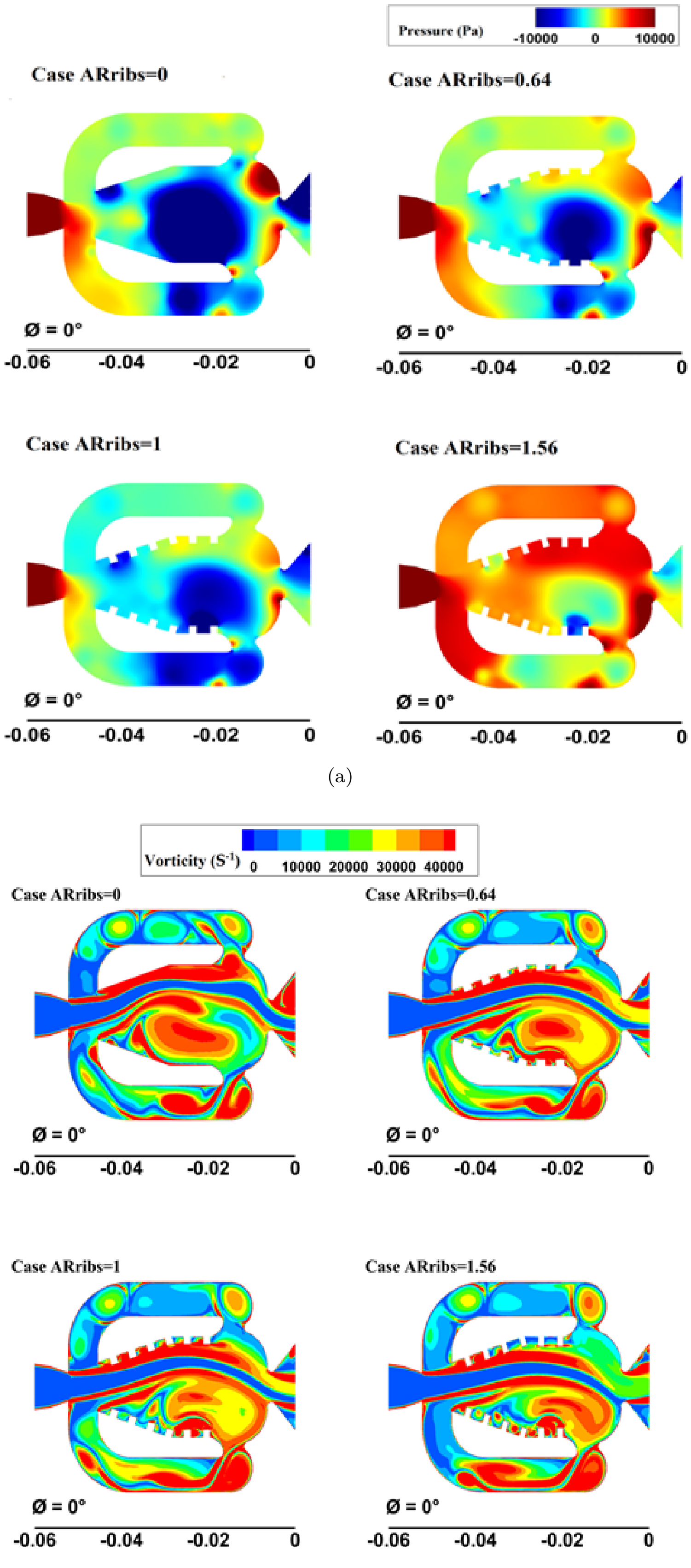

(a)

(b)

FIGURE 4.3: Plots at a phase angle of 0° for different aspect ratios of ribs placed over the Coanda surface (a) Pressure Contours (b) Vorticity contours

due to the formation of a secondary vortex over the ribs. Consequently, there is a reduction in surface contact between the jet and the Coanda surface. This reduction in surface contact reduces the friction experienced by the flow along the Coanda surface. It appears to influence the pressure drop and the increase in aspect ratio reduces the pressure drop. In terms of pressure drop Case ARribs=1.56 having the highest aspect ratio of the ribs is the most effective oscillator among all the oscillators investigated in the present study. It achieves a 22% reduction in pressure drop as compared to the smooth case.

4.3.2.2 Jet Oscillation Frequency and Frequency-Pressure Ratio

Fig. 4.5(a) shows the jet oscillation frequency results for different aspect ratios of the ribs placed over the Coanda surface at a constant jet inlet velocity. It also shows the frequency for the fluidic oscillator with a smooth Coanda surface (no ribs case). It can be observed that there is a significant increase in frequency when ribs are placed over the Coanda surface. The frequency initially remains constant at 740 Hz as the aspect ratio increases from Case ARribs=0.64 to Case ARribs=1. Higher frequencies are obtained as the aspect ratio goes above 1 i.e. for Case ARribs=1.23 frequency becomes 760 Hz, for Case ARribs=1.56 the frequency is increased to 820 Hz. Beyond the square ribs case (Case ARribs=1), the increase in aspect ratio further increases the oscillating frequency of the jet.

The introduction of ribs on the Coanda surface distorts the bubble formed in the mixing chamber of the fluidic oscillator for all cases as in Fig. 4.2. The distortion of the bubble helps the jet move faster towards the other side and hence the jet starts oscillating faster with a higher oscillation frequency. The highest aspect ratio Case ARribs=1.56 has the highest oscillation frequency and it can be observed from the streamlines plot of phase angle $\phi = 0°$ for Case ARribs=1.56 in Fig. 4.2 that the bubble in the mixing chamber is most distorted.

Another reason for the increase in frequency is the reduction in the width of the mixing chamber (distance between the side walls) which enables the jet to move from one side of the mixing chamber to the other side quickly hence the oscillation

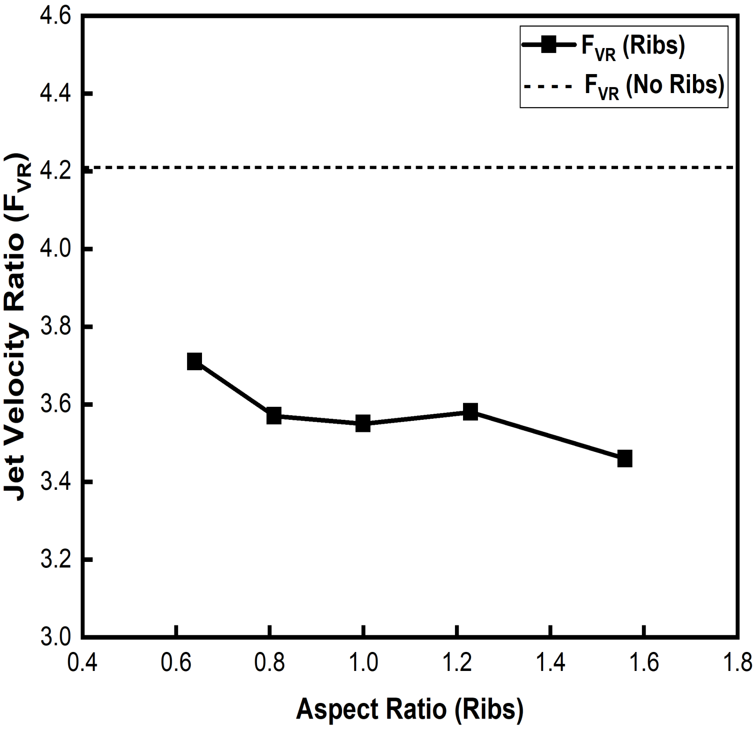

(a)

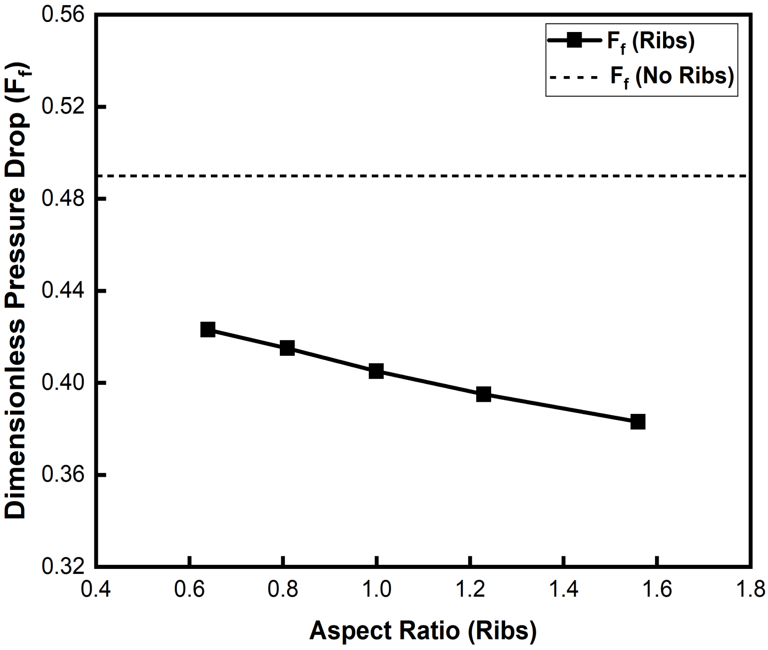

(b)

FIGURE 4.4: (a) Peak velocity ratio variations (b) Dimensionless pressure drop variations, for different aspect ratios of ribs placed over the Coanda surface

frequency is increased. Among the 5 cases studied in detail the Case ARribs =1.56 has the highest dimension of the ribs' height and the lowest width of the mixing chamber and consequently the highest oscillation frequency.

The variations of frequency-pressure ratio (FPR) for different aspect ratios of the ribs placed over the Coanda surface of the fluidic oscillator are presented in Fig. 4.5(b). The frequency-pressure ratio (FPR) presents how the pressure losses through the oscillator and the oscillation frequency of the jet leaving the oscillator are related. The results show that as the aspect ratio of the ribs placed over the Coanda surface is increased, the frequency-pressure ratio (FPR) also increases. The jet starts oscillating faster when the aspect ratio of the ribs is increased. Case ARribs=1.56 is found to be the most effective fluidic oscillator in terms of performance parameter frequency-pressure ratio (FPR).

For each oscillator, the time history of velocity magnitude for a time period of 0.05 sec – 0.1 sec is shown in Fig. 4.6. The velocity magnitude data sample is attained at the centreline of the vertical axis oscillator, 6mm downstream of the exit nozzle. It can be observed from the velocity magnitude temporal plots that multiple high and low-velocity regions of square waves following each other are generated. The maximum velocity peaks for Case ARribs=0.64, Case ARribs =0.81, Case ARribs=1, and Case ARribs=1.23 are very similar. However, the maximum velocity peaks for Case ARribs=1.56 are higher than all other cases. The minimum velocity peaks show a similar trend and the lowest velocity peaks are recorded for the highest aspect ratio Case ARribs=1.56. The highest aspect ratio Case ARribs=1.56 not only increases the maximum and minimum peaks of velocity magnitude but also decreases its period. The period between peaks is highest for the smooth Case ARribs=0. The period between the peaks of the velocity magnitude represents the oscillation frequency. A shorter period corresponds to a higher oscillation frequency and vice versa.

FFT analysis is performed for recorded velocity data obtained for 0.05 sec to quantify the jet oscillation frequencies. Fig. 4.7 illustrates the fast Fourier transform (FFT) results of the measured velocity data of all the ribbed cases. It shows the velocity

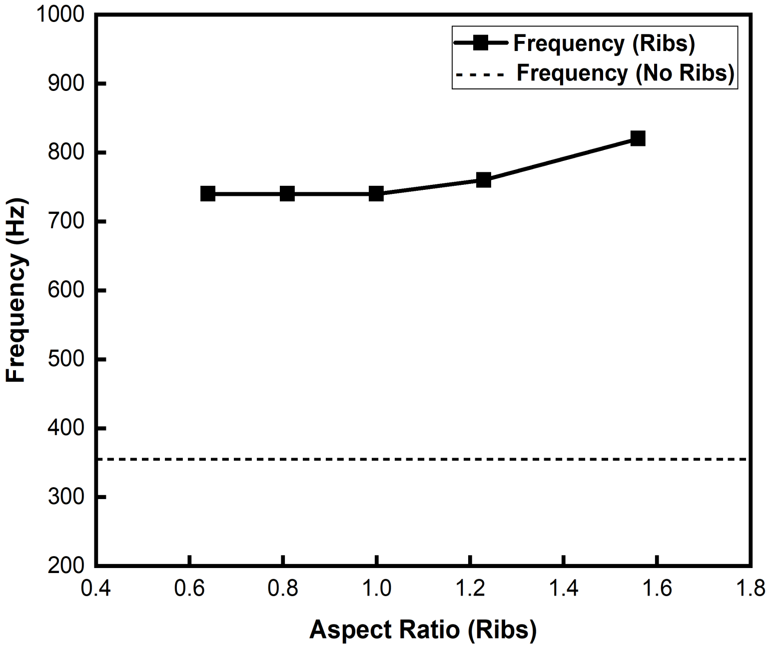

(a)

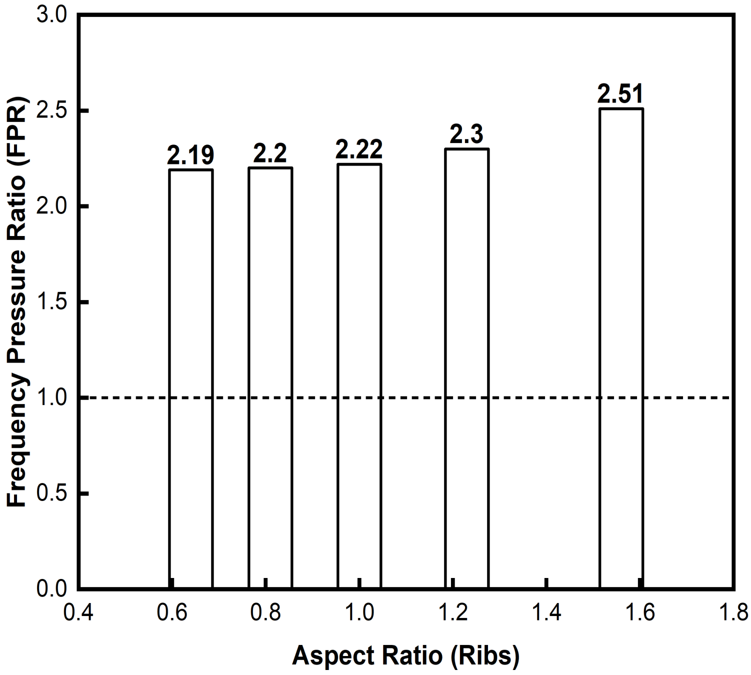

(b)

Figure 4.5: (a) Frequency variations (b) Frequency-pressure ratio variations, for different aspect ratios of ribs placed over the Coanda surface

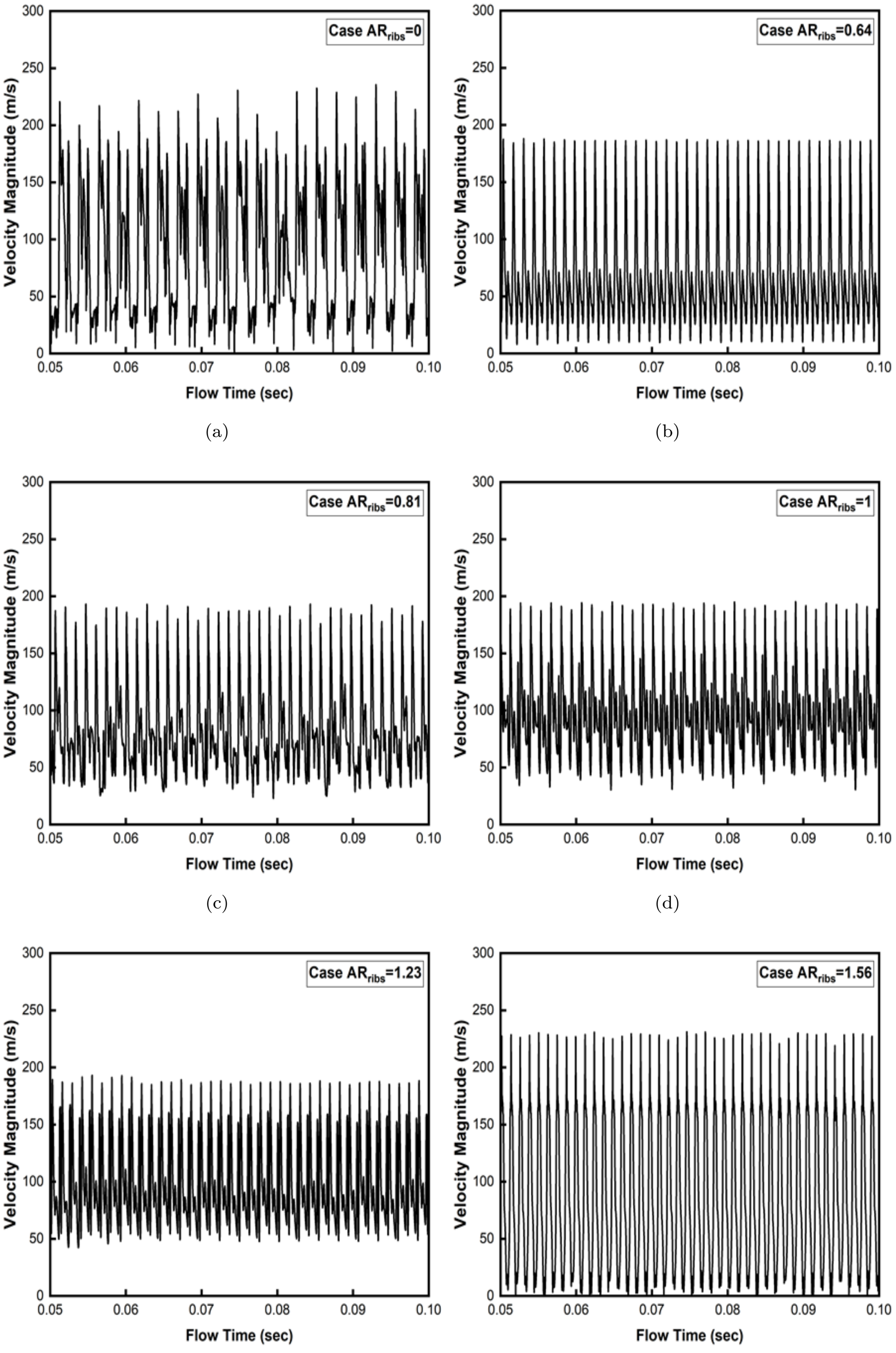

(a) (b) (c) (d) (e) (f)

Figure 4.6: Temporal velocity magnitude data sampled 6mm downstream of the nozzle exit at the centerline of the oscillator for different aspect ratios of ribs placed over the Coanda surface

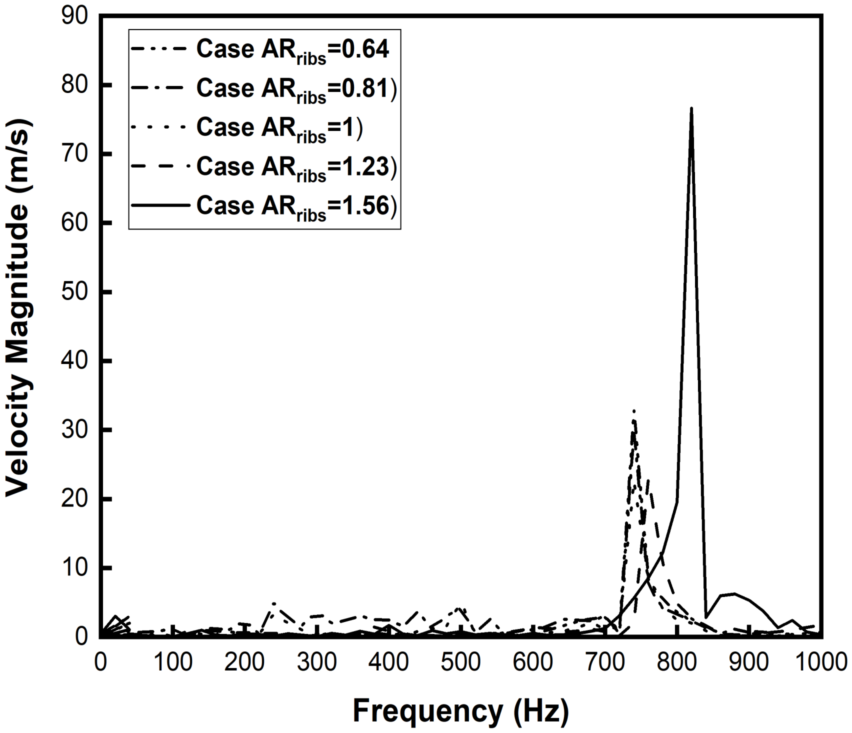

FIGURE 4.7: FFT analysis of temporal velocity magnitude data for various aspect ratios of ribs placed over the Coanda surface

magnitude peaks representing the dominant frequencies for each variation of fluidic oscillators. Specifically, for Cases with rib aspect ratios (ARribs) of 0.64, 0.81, and 1, the oscillation frequencies were found to be 740 Hz. Case ARribs=1.23 exhibited a slightly higher frequency of 760 Hz, while the highest frequency, 820 Hz, was recorded for Case ARribs=1.56. The velocity magnitude or amplitude associated with each peak reflects the strength of the corresponding frequency. A higher amplitude implies a more robust oscillation at that frequency, indicating larger variations in jet velocity. This, in turn, signifies a greater amount of energy available to drive the oscillation. Notably, Case ARribs=1.56 demonstrated the highest amplitude among the cases analyzed, suggesting it has the most substantial oscillation strength.

Fig. 4.8 presents the results of the Strouhal number of jet oscillations for different aspect ratios of ribs placed over the Coanda surface of the fluidic oscillator. The Strouhal number shows a similar behavior to the oscillation frequency. The

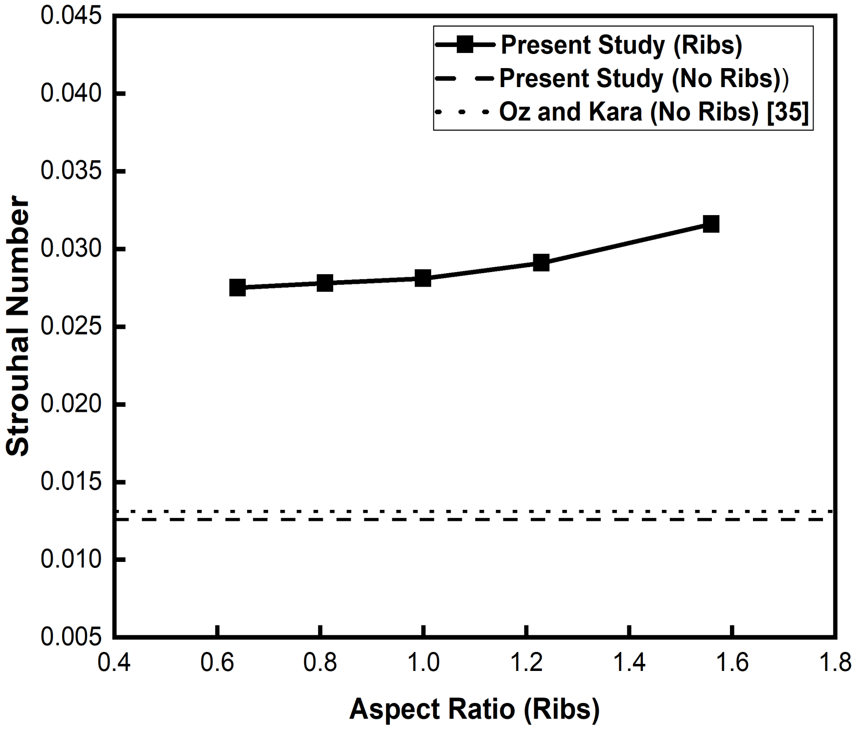

FIGURE 4.8: Strouhal Number variations for different aspect ratios of ribs placed over Coanda surface

Strouhal number for the ribbed Coanda surface oscillators is higher than the smooth oscillators. The average Strouhal number for different mass flow rates through the 2-D compressible flow simulations was found to be 0.0131 by Oz and Kara [83] for the smooth case. In the current study, the Strouhal number for the smooth case is 0.0126, and it increases with the rise in rib aspect ratio, peaking at 0.0316 for Case ARribs=1.56. The Strouhal number demonstrates an overall increase of more than 150% in the jet oscillations for the highest aspect ratio of the ribs as compared to the case with a smooth Coanda surface.

4.3.2.3 Jet Deflection Angle and Jet Deflection-Pressure Ratio

For calculating jet deflection angle θ as shown in Fig. 4.9, first the jet half width δ is quantified. The jet half width is the measurement of the distance between y = 0 and y = where the U_{avg} (y)=0.5 Umax [81]. Table 4.2 presents the jet half-width values for all the cases used in the present study.

Table 4.2: Jet half-width for different cases used in the study

Case	**Aspect ratio**	**Jet half-width δ (mm)**
Case $\mathrm{AR_{ribs}}$=0	0.00	0.03156
Case $\mathrm{AR_{ribs}}$=0.64	0.64	0.01313
Case $\mathrm{AR_{ribs}}$=0.81	0.81	0.01002
Case $\mathrm{AR_{ribs}}$=1.00	1.00	0.00880
Case $\mathrm{AR_{ribs}}$=1.23	1.23	0.00982
Case $\mathrm{AR_{ribs}}$=1.56	1.56	0.01122

From the jet half-width value the jet deflection/spreading angle is calculated

$$\theta = \tan^{-1}\left(\frac{\delta}{x}\right) \tag{4.1}$$

Where x = 3D (0.01905mm) is the distance in the direction of the flow from the exit of the fluidic oscillator.

Fig. 4.10(a) shows the jet deflection angle variation results for the cases with different aspect ratios of ribs embedded on the Coanda surface. The jet deflection angle is highest for the smooth Coanda surface case. The introduction of ribs over the Coanda surface reduces the jet deflection angle as compared to no ribs case. From Fig. 4.10(a) it is evident that the increase in aspect ratio from Case ARribs=0.64 to Case ARribs=1 reduces the jet deflection angle from 34.2° to 24.7°. When the square ribs Case ARribs=1 is again switched to rectangular ribs Case ARribs=1.23 and Case ARribs=1.56 (although now the aspect ratio $>$ 1), the jet deflection angle again starts increasing from 24.7° to 27.2° and 30.3° respectively. The breaking of the separation bubble within the mixing chamber lets the jet move away from the Coanda surface and the jet spreading angles at the exit of the oscillators of cases with ribs are lower than the Case ARribs=0 (no ribs).

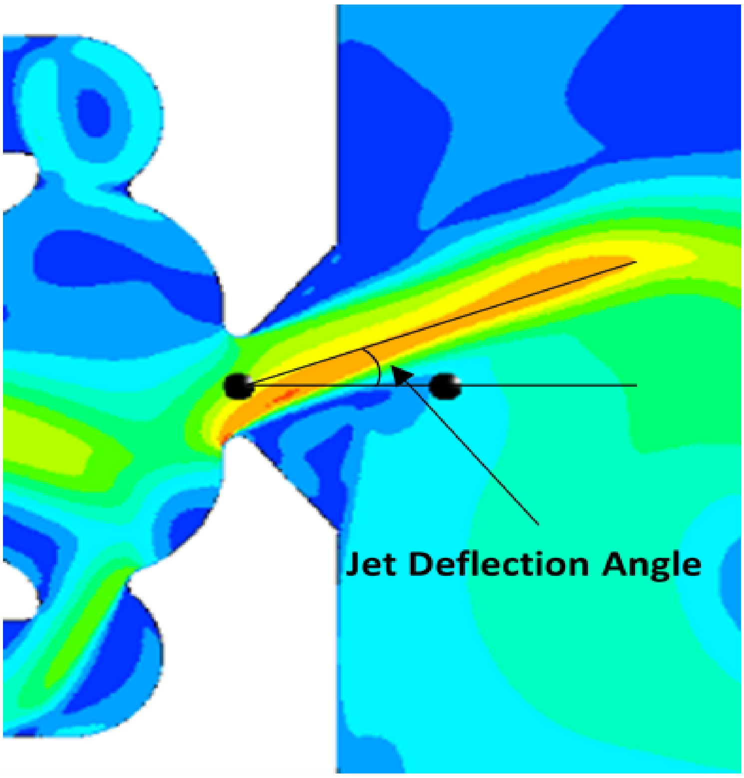

FIGURE 4.9: Jet Deflection Angle measurement detail

The spreading angle is the lowest for the square ribs Case ARribs=1 and rectangular ribs cases send the jet out from the oscillator at a higher jet deflection angle.

The huge size of the primary bubble inside the mixing chamber for no ribs Case ARribs=0 pushes the jet towards the Coanda surface and hence it leaves the oscillator with a greater spreading angle as compared to the oscillators having ribs as shown in Fig. 4.2.

The width of the primary bubble becomes smaller at phase angle $\phi = 90°$ in square ribs oscillator and it appears to be the reason behind the jet leaving with a smaller deflection. It doesn't have any significant effect on the oscillation frequency because it is below the Coanda surface and about to dissipate into the feedback channel.

Fig. 4.10(b) shows the jet deflection-pressure ratio (JDPR), results for different aspect ratios of the ribs on the Coanda surface. The jet deflection-pressure ratio (JDPR) represents the jet spreading angle of the leaving jet as compared to the pressure loss across the oscillator.

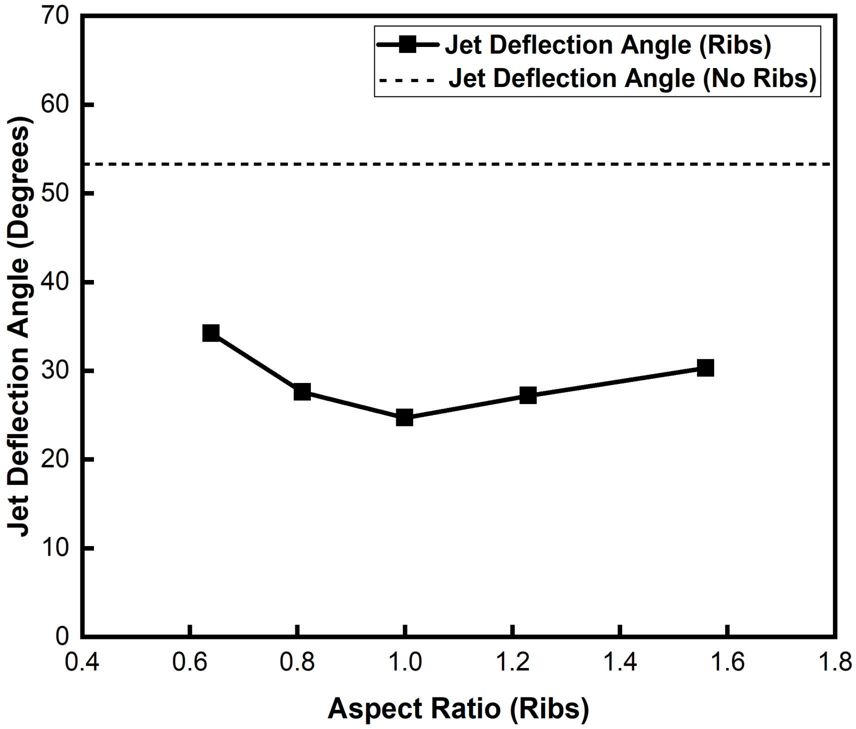

(a)

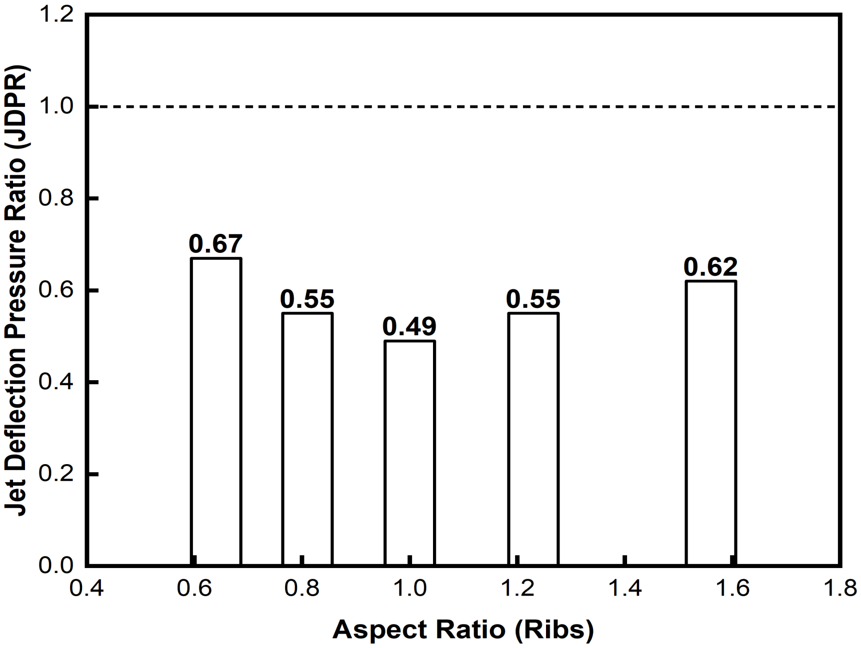

(b)

FIGURE 4.10: (a) Jet deflection angle variations (b) Jet deflection angle-pressure ratio variations, for different aspect ratios of ribs placed over the Coanda surface

The larger the jet deflection-pressure ratio (JDPR), the larger will be the jet spreading angle as compared to the pressure loss. The jet deflection-pressure ratio (JDPR) for the cases with ribs is lower than the smooth Coanda surface case.

The jet deflects at a higher angle when there are no ribs on the Coanda surface of the fluidic oscillator.

As far as the trend of cases with ribs is concerned, the jet deflection-pressure ratio (JDPR) first decreases with the increase in ribs' aspect ratio till the square ribs Case ARribs=1 is reached. Beyond the square ribs Case ARribs=1, the jet deflection-pressure ratio (JDPR) starts increasing with an increase in aspect ratio.

The most effective oscillator in terms of jet deflection-pressure ratio (JDPR) is the no ribs oscillator Case ARribs=0. Among the oscillators with ribs, Case ARribs=0.64 having the lowest aspect ratio is the most impactful oscillator.

4.3.2.4 Jet Frequency-Deflection-Pressure Ratio

Fig. 4.11 shows the variation of Jet Frequency-Deflection-Pressure Ratio (FDPR), for different aspect ratios of ribs placed over the Coanda surface of the fluidic oscillator. The FDPR represents the combined effect of the oscillator in terms of the oscillating frequency of the jet exiting the oscillator and the area that the jet will cover when it leaves the oscillator. The higher the FDPR, the faster the jet leaving the oscillator will oscillate and it will cover a larger area while oscillating.

As discussed previously, the oscillation frequency and jet spreading are the two significant output parameters when oscillators are used in flow control and cooling hot surfaces. Deflection angle in Fig. 4.10 (a) and FDPR in Fig. 4.11 exhibit similar variations to aspect ratio. This means that the qualitative variation of FDPR is dominated by the deflection angle change. The performance parameter FDPR helps identify the oscillator that has a higher combined effect of oscillation frequency and jet spreading with lower pressure loss. The Case ARribs=1.56 is the most effective oscillator in terms of the performance parameter FDPR among all the cases studied presently as shown in Fig. 4.11. The square ribs Case ARribs=1

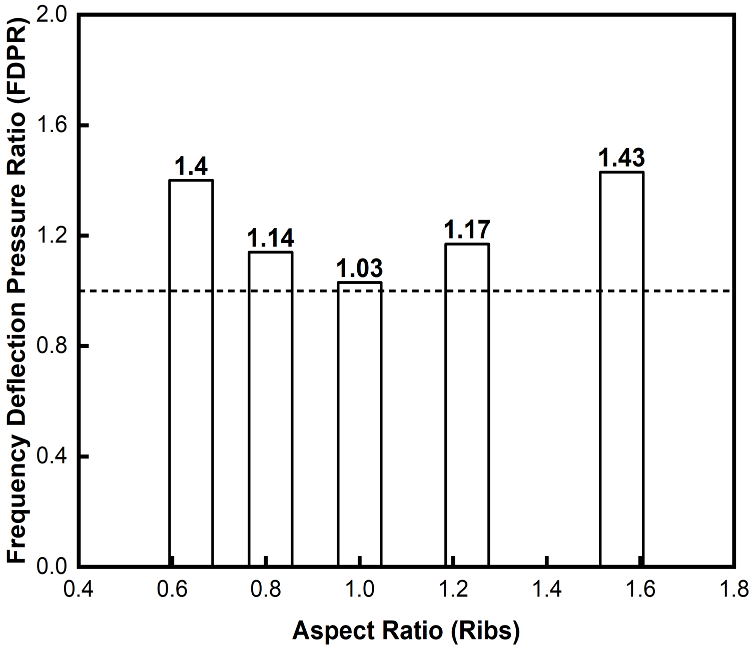

Figure 4.11: Frequency jet deflection angle-pressure ratio variations for different aspect ratios

is the least effective and provides similar performance to the smooth Coanda surface case.

It can also be observed that both extreme rectangular ribs cases having the largest height Case ARribs=1.56 and largest base Case ARribs=0.64 show almost similar values of FDPR. Hence, fluidic oscillators with rectangular ribs show an enhanced overall effect of oscillation frequency and coverage area with minimal pressure losses. It can be noted that, in comparison to the reference case with no ribs, the FDPR exhibited a substantial increase of 43% for the aspect ratio of 1.56.

4.4 Conclusion

The current study numerically investigated the effect of various aspect ratios integrated on the Coanda surface on the performance of the fluidic oscillator. The aspect ratios were varied between 0.64-1.56 and the following new geometries were analyzed; Case ARribs=0.64, Case ARribs=0.81, Case ARribs=1, Case ARribs=1.23 and Case ARribs=1.56. The main conclusions are outlined below.

The internal flow dynamics of the fluidic oscillator revealed that the oscillation frequency and jet deflection angle were strongly affected by the size of the recirculation bubble generated in the mixing chamber of the oscillator. The bubble size was extensive, spanning over half of the mixing chamber in the absence of ribs. Conversely, in the case of the highest aspect ratio, the bubble was notably small. Consequently, the resistance for the flow to switch from one wall to the other was minimized, thereby contributing to an increase in oscillation frequency.

The results indicated that an increase in the aspect ratio of ribs positioned on the Coanda surface of the oscillator leads to a rise in the oscillation frequency. The highest oscillation frequency of 820 Hz was recorded for the highest aspect ratio ribs Case ARribs=1.56. It was also noted that the rectangular-shaped ribs, specifically those with the lowest and highest aspect ratios (Case ARribs=0.64 and Case ARribs=1.56), exhibit a greater jet deflection angle, whereas square ribs (Case ARribs=1) display a lower deflection angle. A 22% decrease in pressure drop was experienced for the ribbed case with the highest aspect ratio when compared to the smooth case.

The study examined the performance of oscillators across six parameters: peak jet velocity ratio, dimensionless pressure drop, frequency-pressure ratio, Strouhal number, jet deflection angle-pressure ratio, and frequency jet deflection-pressure ratio. Following are the conclusions from analyzing these performance parameters: In case of peak jet velocity ratio, higher rib aspect ratios decrease the jet velocity ratio, enhancing oscillator effectiveness. Case ARribs=0 (no ribs) exhibits the highest performance in terms of jet velocity ratio, while Case ARribs=0.64 (lowest aspect ratio) stands out among ribbed oscillators.

The dimensionless pressure drop decreases with increasing rib aspect ratio due to reduced frictional losses. Case ARribs=1.56, featuring the highest rib aspect ratio, demonstrates the highest effectiveness, achieving a 22% reduction in pressure drop compared to the smooth case.

The FPR indicates the relationship between oscillation frequency and pressure losses. Results demonstrate that as the aspect ratio of the ribs increases, so does the FPR, implying faster jet oscillation. Case ARribs=1.56 emerges as the most effective fluidic oscillator, achieving the highest performance in terms of FPR. The Strouhal number, indicating jet oscillations in fluidic oscillators with ribs placed on the Coanda surface, exhibits a behavior mirroring oscillation frequency trends. Notably, ribbed oscillators show higher Strouhal numbers compared to smooth case. The Strouhal number peaks at 0.0316 for Case ARribs=1.56, marking a significant increase of over 150% in jet oscillations compared to the smooth case, thus demonstrating the superior performance of oscillators with higher aspect ratios of ribs.

The JDPR, indicative of jet spreading angle versus pressure loss across the oscillator, varies with different aspect ratios of ribs on the Coanda surface. Notably, the absence of ribs yields the highest JDPR. Among ribbed oscillators, the most effective performance is observed in Case ARribs=0.64, characterized by the lowest aspect ratio, suggesting significant impact on jet deflection as compared to pressure loss. The FDPR reflects the combined influence of the frequency of the oscillating jet and the spreading of the jet. It was noted that the FDPR was 43% greater for the Case ARribs=1.56 compared to the reference Case ARribs=0. Although both extreme rectangular rib cases (ARribs = 0.64 and 1.56) show a significantly enhanced overall effect, Case ARribs = 1.56 exhibits the highest FDPR value and is therefore identified as the most effective configuration among those studied. As Case ARribs=1.56 exhibits the highest value of FDPR, it is consequently more effective in situations where a greater combined impact of frequency and jet spreading is needed.

Chapter 5

Flow Performance in Fluidic Oscillators: Influence of Number of Ribs

5.1 Introduction

The previous chapter presented the results of the role of rib aspect ratio in enhancing the flow performance of a double-feedback fluidic oscillator. Extending this analysis, the present chapter systematically evaluates the influence of the number of ribs placed over the Coanda surface to improve the fluidic oscillator performance. Through controlled parametric variation, this study quantifies the effects of number of ribs on critical flow parameters, including oscillation frequency, spreading angle of the jet and pressure loss. The results establish design guidelines for rib configuration, advancing the development of efficient fluidic oscillators for active flow control applications. The present research investigates the influence of changing the ribs count on the fluidic oscillator's Coanda surface. The main objective is to evaluate the impact of these modifications on important performance measures such as pressure distribution, oscillation frequency and flow stability in order to enhance the oscillator's efficiency. An analysis is carried on different fluidic oscillator designs, each of which incorporates a different number of ribs over the Coanda surface. The study evaluates the impact of variations in the rib count on six nondimensional performance parameters. These parameters include the FPR (Frequency-Pressure Ratio), the non-dimensional pressure drop through the oscillator, the Strouhal number, and JDPR (Jet Deflection-Pressure Ratio) and FDPR (Frequency-Deflection-Pressure Ratio), which represent the ratios of the jet deflection angle and the combined frequency-deflection angle respectively to the pressure loss. The analysis of the combined effect of frequency and jet spreading angle of the fluidic oscillator is conducted using the SST turbulence model.

5.2 Problem Formulation

In the current research work, the effect of changing the number of ribs on the Coanda surface of the fluidic oscillator is explored. Six different geometries of the fluidic oscillator are designed, each with a different number of ribs, ranging from 1 to 6, while keeping the rib aspect ratio constant at 1.56. Fig. 5.1 and Table 5.1 illustrate these six geometries.

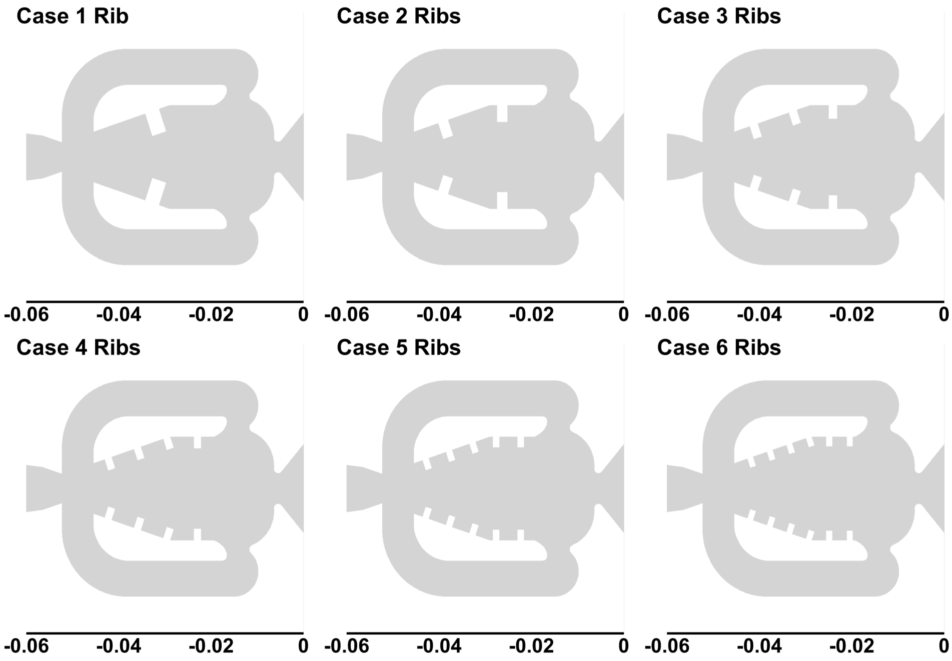

FIGURE 5.1: Different oscillators used in the present study

The aspect ratio of the rib, defined as the ratio of the rib's height (Rh) to its base (Rb), was kept at 1.56, and a single rib to the Coanda surface is added initially. As the number of ribs increased, the dimensions of each rib decreased, and the gap between ribs was adjusted accordingly. The dimensions and gap were larger for a single rib design, whereas in the designs with more ribs, each rib became smaller, and the gap between ribs narrowed. Despite these variations, the total rib area remained constant across all configurations.

TABLE 5.1: Details of geometric parameters of different configurations used in the present study

Case	**No. of ribs**	**Aspect ratio**	**Height (mm)**	**Width (mm)**	**Gap (mm)**	**Area (mm^2)**	**Total area (mm^2)**
Case 1 Rib	1	1.56	4.900	3.135	23.595	15.360	15.36
Case 2 Ribs	2	1.56	3.465	2.217	11.148	7.680	15.36
Case 3 Ribs	3	1.56	2.829	1.810	7.100	5.120	15.36
Case 4 Ribs	4	1.56	2.450	1.570	5.113	3.840	15.36
Case 5 Ribs	5	1.56	2.191	1.402	3.944	3.072	15.36
Case 6 Ribs	6	1.56	2.000	1.280	3.175	2.560	15.36

5.3 Results and Discussions

5.3.1 Influence of Number of Coanda Surface Ribs on Internal Flow Dynamics of the Oscillator

As discussed in previous chapter, when the jet enters the mixing region of double feedback fluidic oscillator through the supply nozzle, even small perturbations in the flow result in pressure imbalance along the mixing region walls. This pressure differential induces the phenomenon known as the Coanda effect, where the jet attaches to one of the mixing region walls. As the jet progresses closer to the wall, the Coanda effect strengthens, ultimately causing full attachment. This complete attachment corresponds to a phase angle of ϕ=0°, indicating that the jet at the inlet and outlet are in phase, with no deflection observed at the exit throat. A part of the jet enters into the feedback channel, where it flows back to interact with the main jet in the mixing channel. The flow reentering from the feedback channel tends to detach the main jet from the wall, displacing the jet toward the opposite wall. The full switch of the main jet to the opposite wall signifies a phase angle of 180°. Phase angles such as 0°, 45°, 90°, 135°, and 180° cover one-half of the oscillation cycle for the jet. This process is repeated symmetrically, producing a self-sustained oscillating jet. Following the internal switching, the jet initiates a sweeping motion in the external domain.

Streamline plots for the oscillator configurations Case 1 Rib through Case 6 Ribs are shown in Fig. 5.2. It is evident from the streamline plots for all cases that at the phase angle ϕ=0°, the jet entering the mixing chamber attaches to one side of the Coanda surface and generates a primary separation bubble near the opposing Coanda surface within the mixing chamber. In the oscillator Case 1 Rib, the separation bubble exhibits the smallest size compared to all other oscillators. An increase in the ribs count results in a progressive enlargement in the size of the separation bubble. The size of the single rib on the Coanda surface in each oscillator case significantly influences the size of the primary separation bubble. The jet flows across a narrow path within the mixing chamber, in the Case 1 Rib oscillator with the largest size of the single rib. While in the oscillator Case 6 Ribs, the jet flows across the widest path. The increase in the rib size within each configuration restricts the passage within the mixing chamber, thereby elevating jet velocity. The intensified jet velocity compresses the separation bubble, as observed in Case 1 Rib. Furthermore, upon entering the mixing chamber, the jet encounters the first rib, causing deflection from the Coanda surface and preventing attachment to it. This deflection compresses the primary separation bubble, reducing its size. However, as the number of ribs increases, the extent of jet deflection becomes smaller, leading to the creation of a larger separation bubble on the opposite side.

At a phase angle of ϕ=45°, the separation bubble in Case 1 Rib is observed to be pushed furthest towards the entrance of the feedback channel, with a notable reduction in its size. As the number of ribs increases, the separation bubble remains confined within the mixing chamber and grows larger respectively. At a phase angle of ϕ=135°, the separation bubble in Case 1 Rib nearly disappears into the

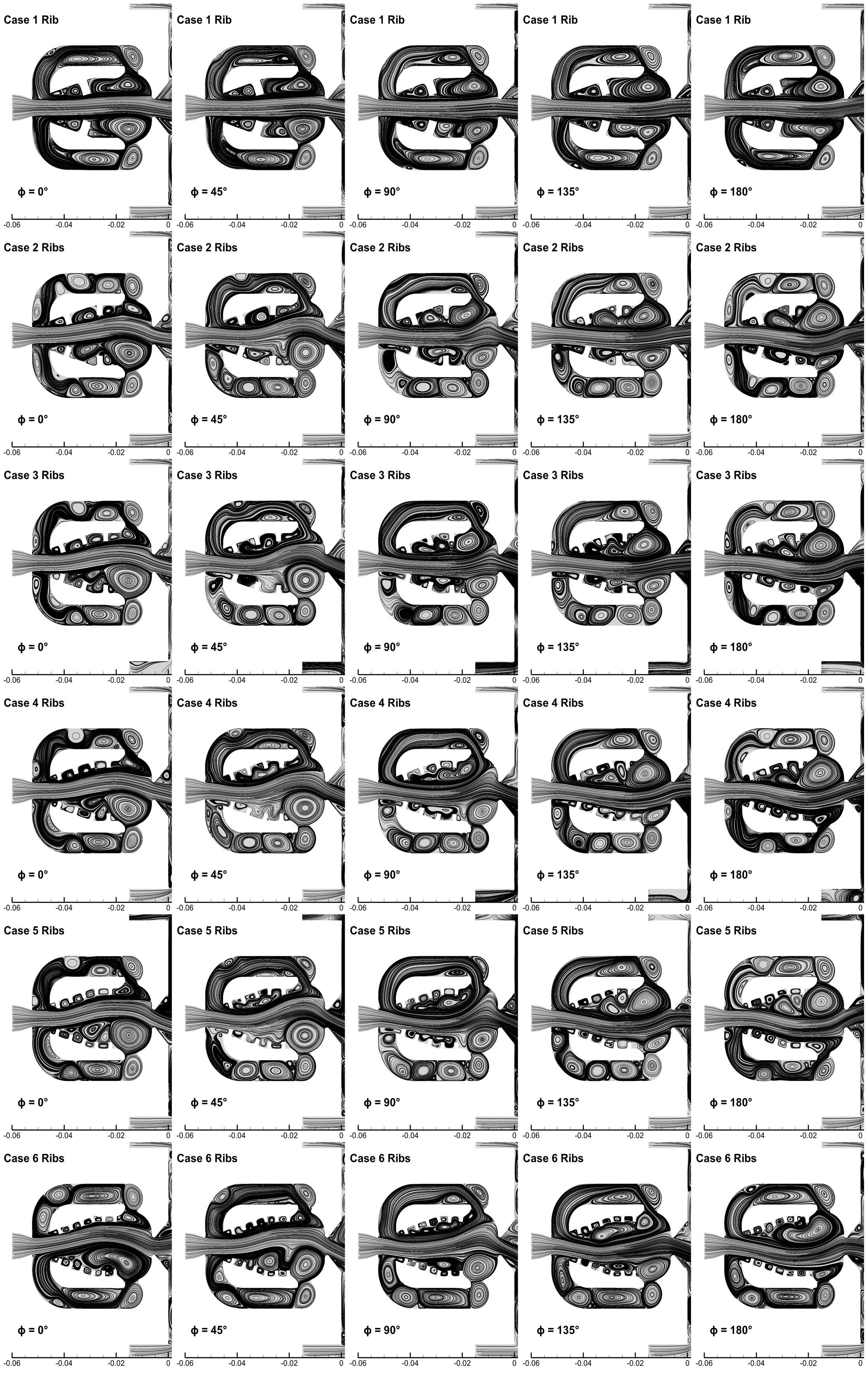

FIGURE 5.2: Streamline plots for oscillators of different numbers of ribs at various phase angles

feedback channel, whereas in other cases, it remains present. Remarkably, in Case 4 Ribs, the separation bubble is the smallest among the multi-rib configurations and nearly vanishes, resembling the behavior observed in Case 1 Rib. At phase angles of ϕ=90° and ϕ=135°, a separation bubble of similar shape begins to develop on the opposite side across all configurations. By the phase angle of ϕ=180°, the formation of this identical-sized separation bubble is finalized for every case. At this stage, the flow transitions and attaches to the opposite side, marking the completion of half of the jet oscillation cycle.

Fig. 5.3 shows the pressure contours at a phase angle ϕ=0°, for different oscillator geometries Case 1 Ribs up to Case 6 Ribs. The overall pressure range in the fluidic oscillator for Case 1 Rib is low, and the oscillator's mixing chamber and feedback channel form a large low-pressure region. As the rib count increases, a rise in the overall pressure within the oscillator system can be observed. However, Case 4 Ribs shows a different behavior, where the overall pressure in the mixing chamber and feedback channel does not follow the rising trend.

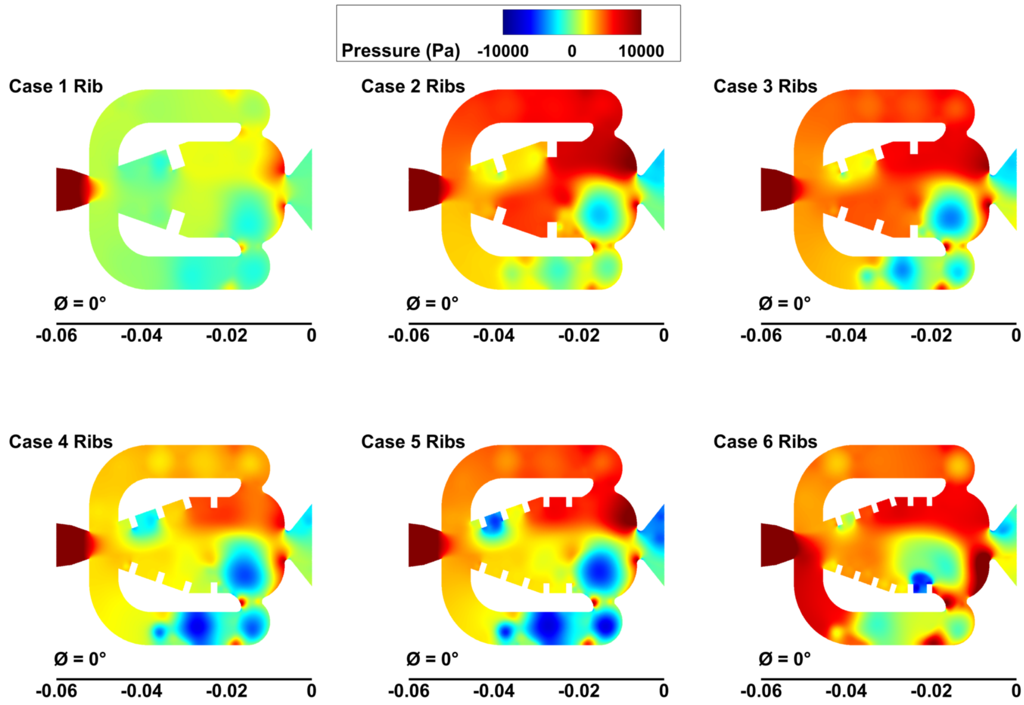

FIGURE 5.3: Pressure contours for oscillators of different numbers of ribs at phase angle ϕ=0°

In Case 1 Rib, the pressure differential in the mixing chamber is not significant, and the large size of the rib prevents the creation of a substantial bubble in the mixing chamber, as also shown in the streamline plots. For oscillators Case 2 Ribs to Case 6 Ribs, a prominent pressure differential and a distinct low-pressure zone are observed in the mixing chamber, which promotes the creation of the separation bubble. A larger size separation bubble appears due to progressive low-pressure zone enlargement with increase in rib count, as depicted in the streamline plots. The low-pressure zone in the mixing chamber directly determines the size of the separation bubble, which significantly affects the flow dynamics.

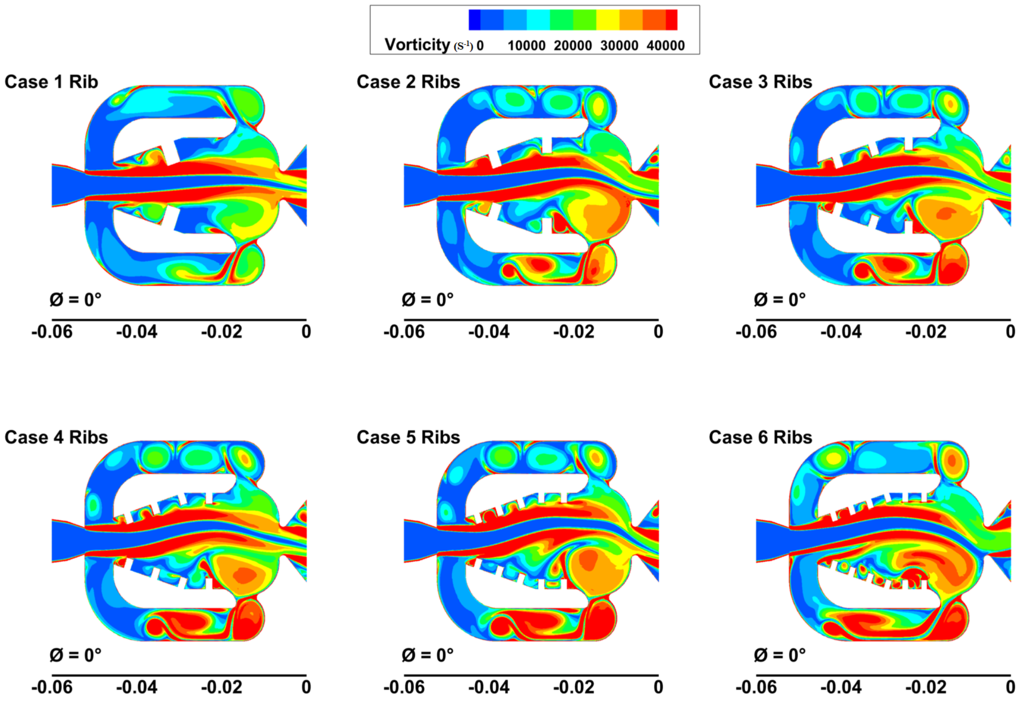

Figure 5.4: Vorticity contours for oscillators of different numbers of ribs at phase angle ϕ=0°

The jet oscillation is strongly influenced by the separation bubble and flow dynamics in the chamber. In Case 1 Rib, the small separation bubble leads to rapid alternating flow within the mixing chamber. As the number of ribs increases, the enlargement of the separation bubble dampens the rapid alternations, causing a general decrease in jet oscillation. However, in Case 4 Ribs, the oscillation shows a slight increase compared to the trend. This deviation could be attributed to optimal rib spacing or specific flow interactions that enhance the oscillatory behavior in this case. Overall, the pressure contours depict the complex interplay between oscillator designs with varying numbers of ribs and the resulting flow dynamics in these oscillators.

The Fig. 5.4 illustrates variations in the size of the separation bubbles formed in the mixing chamber using vorticity contours at a phase angle of 0°. These vorticity contours correspond to different oscillator configurations with ribs installed along the Coanda surface. It can be observed that the jet is influenced by regions of high vorticity surrounding it on both sides. In Case 1 Rib, the high-vorticity zones are directed more toward the center of the mixing chamber due to the rib's larger size. As the rib count increases from 2 to 6, the high-vorticity regions on either side of the jet are gradually shifted closer to the one side of the Coanda surface in the lower section of the chamber. This deflection of jet towards the center of the mixing chamber facilitates faster jet switching between sides of the Coanda surface in Case 1 Rib. However, with more ribs, the jet is progressively pushed away from the chamber's center, allowing larger separation bubbles to form on the opposite side, which results in slower switching dynamics.

5.3.2 Influence of Number of Ribs on Coanda Surface Over Flow Performance Improvement of Oscillator

The subsequent sections present a comprehensive analysis of how varying the number of Coanda surface ribs affects the characteristics of a fluidic oscillator, using a diverse set of performance parameters.

5.3.2.1 Influence over Jet Oscillating Frequency

Fig. 5.5 (a) presents the results of jet oscillation frequency for various oscillator designs, where different numbers of ribs are placed on the Coanda surface. These results are compared with the frequency observed in a fluidic oscillator that has a smooth Coanda surface (no ribs). The results clearly show that placing the ribs on Coanda surface significantly enhanced the frequency of oscillating jet. The variation in frequency for different number of ribs oscillators can be linked to the size of the separation bubble observed in the streamline plots in Fig. 5.2. The distortion and compression of the separation bubble enable the jet to move quickly toward the opposite Coanda surface, resulting in faster jet oscillations and a higher oscillation frequency. In Case 1 Rib, the smallest separation bubble leads to faster jet switching, and hence the highest frequency of 1160 Hz is achieved. As the number of ribs increases (Case 2 Ribs to Case 6 Ribs), the separation bubble grows larger in size due to reduced jet deflection and a wider path within the mixing chamber. This enlargement in the size of the separation bubble increases the resistance to jet flow switching and hence frequency is reduced. As for Case 2 Ribs, the frequency decreased to 886 Hz. This downward trend in frequencies persists, with the frequency dropping to 857 Hz when Case 3 Ribs is used.

Interestingly, in Case 4 Ribs, the separation bubble momentarily reduced in size, and caused a minor frequency recovery to 875 Hz. Further addition of ribs continued to reduce the frequency, with the Case 5 Ribs showing a drop to 843 Hz, and the Case 6 Ribs further decreased it to 820 Hz. Notably, the Smooth Case (no ribs) resulted in the lowest frequency of 355 Hz.

These results clearly show the significant role that the placement of ribs plays in enhancing the oscillation frequency. Overall, the interplay between rib-induced jet deflection and separation bubble size governs the observed frequency variations.

The oscillation frequency observed in the six oscillator configurations can be explained through the analysis of the underlying fluid dynamic mechanisms and the influence of rib structures on flow behavior. The ribs installed over the Coanda surface act as geometric features that perturb the jet flow, generating vortical structures and modifying the pressure field within the oscillator's mixing chamber.

These perturbations directly impact the flow in feedback loop, responsible for sustaining oscillations. The pressure contour plots, as provided in Fig. 5.3, highlight distinct zones of high and low pressure, which are instrumental in characterizing the flow dynamics. These gradients not only govern the fluid motion but also play an important role in maintaining oscillatory behavior, while the vortices induced by the ribs can either reinforce or impede the feedback process.

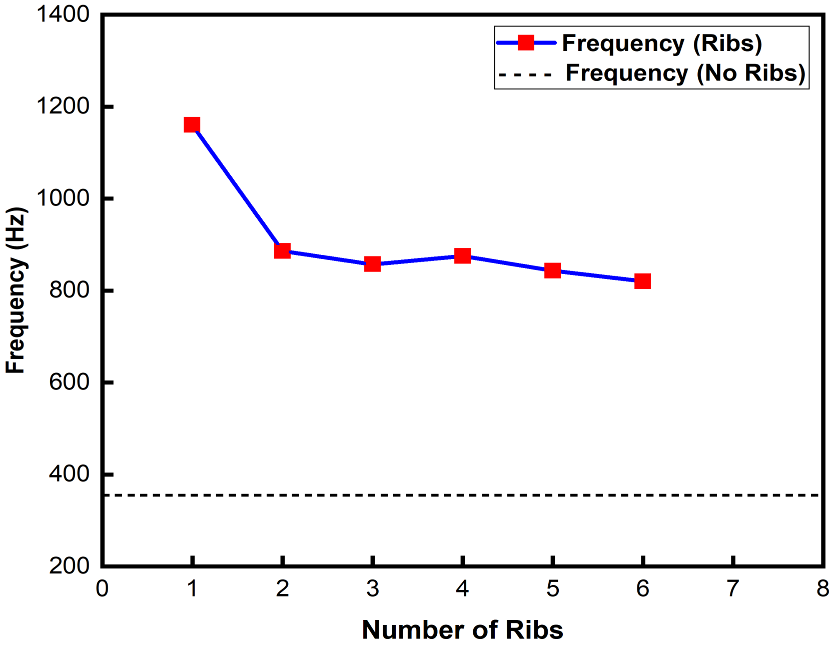

(a)

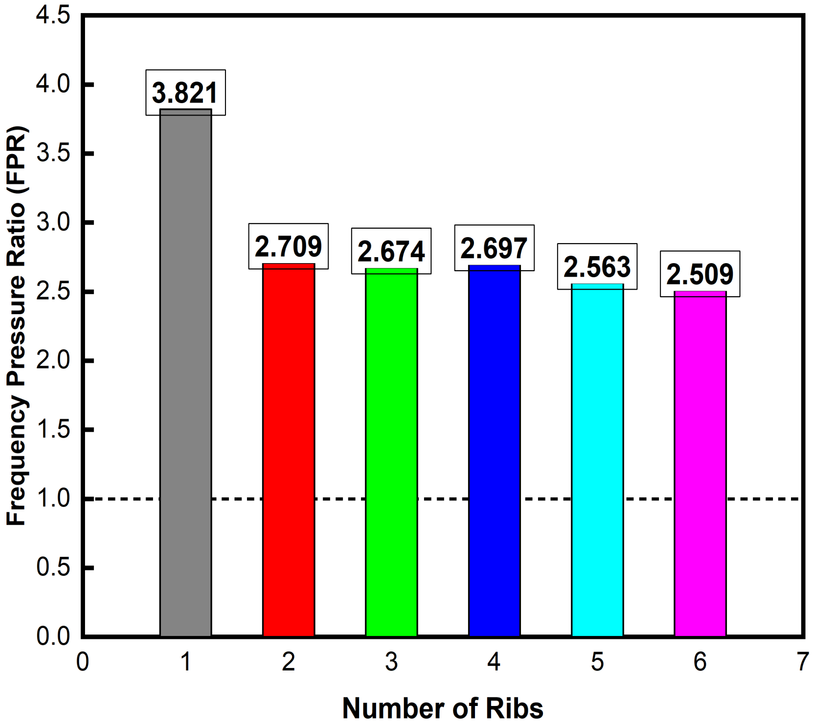

(b)

FIGURE 5.5: (a) Frequency variations and (b) frequency–pressure ratio variations, for oscillators with different number of ribs over the Coanda surface

In Case 1 Rib, the flow remains relatively undisturbed, as evidenced by the pressure and vorticity contour plots in Fig. 5.3 and Fig. 5.4 respectively, which show minimal flow separation and weaker vortical structures. This simplicity in the flow field allows for a more efficient feedback mechanism, resulting in faster feedback cycles and the highest observed oscillation frequency. The pressure contours reveal smoother gradients, and the vorticity plots indicate limited vortex formation, both of which contribute to the efficient propagation of the feedback signal. As the number of ribs increases to two and three (Case 2 Ribs and Case 3 Ribs), the flow field becomes more complex.

The pressure contours show stronger pressure gradients, while the vorticity plots reveal intensified vortical activity. These disturbances disrupt the feedback mechanism, slowing down the feedback cycles and reducing the oscillation frequency. The additional ribs introduce more flow resistance and create multiple vortices, which interfere with the pressure recovery and feedback propagation. At Case 4 Ribs, the flow field again shows relatively undisturbed characteristics compared to the higher rib counts, as shown in the pressure contour plots. The pressure gradients are less severe, and the vorticity plots display relatively more organized flow pattern with smaller disruptive vortices. This allows for a slight improvement in the feedback mechanism, leading to a small increase in oscillation frequency. However, with five and six ribs (Case 5 Ribs and Case 6 Ribs), the flow resistance and energy dissipation become dominant. The pressure contours reveal relatively irregular gradients, while the vorticity plots show relatively chaotic vortical structures. These factors dampen the feedback mechanism, causing the oscillation frequency to decrease again. The increased flow complexity and energy dissipation hinder the efficient propagation of the feedback signal, resulting in reduced oscillatory performance. The underlying mechanisms driving these frequency variations are closely linked to the temporal characteristics of the feedback loop and the energy dissipation within the system. The presence of ribs modifies the flow path and pressure distribution, thereby altering the feedback loop timing. Furthermore, the energy dissipation attributable to frictional effects and vortex shedding becomes more pronounced with additional ribs, which can lessen the oscillations and lower the frequency.

Fig. 5.5(b) presents the results of FPR, for different numbers of ribs installation on Coanda surface of oscillator. FPR represents the relationship between the pressure losses within the oscillator and the oscillating frequency of the exiting jet from the fluidic oscillator. The results indicate that increasing the number of ribs on the Coanda surface decreased the FPR value. The smooth case, which has no ribs, demonstrated the lowest FPR, highlighting the prominent influence of ribs in increasing the FPR in fluidic oscillators. Among all oscillator configurations studied, Case 1 Ribs demonstrated the highest FPR, making it the most effective fluidic oscillator in terms of the FPR performance parameter.

5.3.2.2 Influence over Jet Deflection Angle Performance

The Fig. 5.6(a) shows the influence of the ribs count over the jet deflection angle of the oscillator. Additionally, it compares the results of the deflection angle of the ribbed oscillators to the smooth oscillator. The results provide insight into how the Coanda surface ribs count affect the jet spreading angle of oscillator. For ribbed oscillators, the jet deflection angle shows a distinct pattern. With the increase in number of ribs from Case 1 Rib to Case 4 Ribs, the deflection angle increased, peaking at 37.1° for Case 4 Ribs oscillator. The result shows that introducing more ribs initially enhanced the jet deflection angle. It is likely due to the geometrical structure of the oscillators, the size of the separation bubble and the tilting of the jet in the direction of the lower part of Coanda surface creating increased jet exit angle. However, beyond four ribs, the deflection angle decrease, stabilizing around 29° for Case 5 Ribs and Case 6 Ribs. This suggests that while ribs initially improved the jet deflection angle, excessive ribbing, led to a reduction in the jet deflection angle. It also indicates that the Case 4 Ribs oscillator design represents the optimal configuration in terms of producing higher jet deflection angle. This comparison for oscillators with different number of ribs shows that placement of ribs offered enhanced control over the jet spreading initially but lost effectiveness over an optimal number i.e. 4 ribs. The smooth surface configuration unlike ribbed oscillators, exhibited a higher deflection angle of 53.3°.

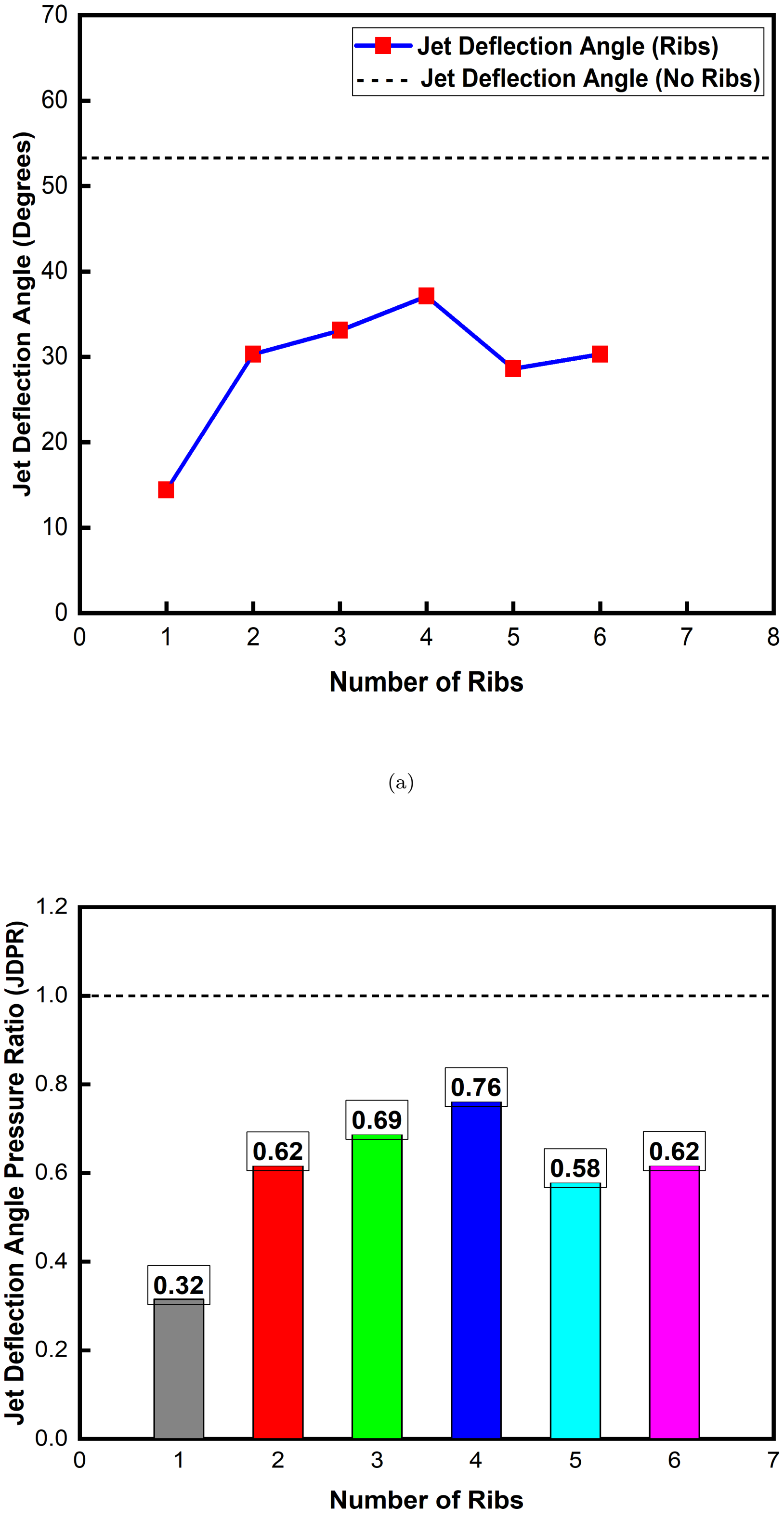

(a)

(b)

Figure 5.6: (a) Jet deflection angle variations and (b) jet deflection angle pressure ratio variations, for oscillators with different number of ribs over the Coanda surface

For the Case 1 Rib, the single rib on either side of the Coanda surface has a larger height, creating a narrower passage for the jet. This narrowing increases the flow velocity and momentum. The pressure distribution remains relatively uniform in whole oscillator, and the vorticity plots reveal weaker vortical structures due to the limited disturbance from a single rib. The combination of high momentum and minimal vortical interference results in a lower jet deflection angle, as the jet tends to follow a more direct path with less lateral deviation. As the number of ribs increases to 2, 3, and 4 ribs, the rib heights are reduced, creating a more open flow passage. The pressure contours show localized regions of high and low pressure, while the vorticity plots reveal intensified vortical activity. These disturbances create asymmetric pressure distributions and stronger vortices, which enhance the feedback mechanism and increase the jet deflection angle. The jet is pushed more significantly to one side due to the amplified pressure imbalances and vortical forces, with the deflection angle peaking at Case 4 Ribs, where the flow achieves an optimal balance between disturbance and feedback efficiency. For the Case 5 Ribs and Case 6 Ribs, the individual rib heights are the smallest, but the cumulative effect of multiple ribs introduces significant flow resistance and energy dissipation. The pressure contours show irregular gradients and pressure losses, while the vorticity plots display highly chaotic vortical structures. This excessive flow complexity disrupts the feedback mechanism, causing the jet deflection angle to decrease slightly compared to the Case 4 Ribs. The jet is less consistently deflected due to the overwhelming flow resistance and disorganized vortices, despite the smaller rib heights. Fig. 5.6(b) presents the JDPR, for various numbers of ribs installed on the Coanda surface. The JDPR quantifies the ratio of jet spreading angle to pressure loss across the oscillator. A higher JDPR indicates a greater jet spreading angle relative to the pressure loss. The results show that the JDPR value for Smooth Case is higher than ribbed oscillator configurations. This is because the smooth Coanda surface oscillator allows the jet to deflect at a higher angle compared to ribbed oscillators. Among the ribbed cases, the JDPR initially increased with the number of ribs, reaching its peak at Case 4 Ribs. However, further increasing the number of ribs to Case 5 Ribs and Case 6 Ribs resulted in a decline in JDPR. Overall, the smooth Coanda surface oscillator demonstrated the best JDPR performance, while Case 4 Ribs is the most effective oscillator among the ribbed designs.

5.3.2.3 Influence over Pressure Drop and Strouhal Number

The results of dimensionless pressure drop, are shown in Fig. 5.7(a) for different oscillator configurations involving various numbers of ribs installed on the Coanda surface. These oscillator designs are compared with a smooth case oscillator. The results indicate that the placement of ribs generally reduces the dimensionless pressure drop when compared to the smooth case oscillator.

The oscillator without ribs has the highest dimensionless pressure drop, emphasizing that the absence of ribs shows greater resistance to flow. When a single rib is installed on the Coanda surface of oscillator Case 1 Rib, the pressure drop significantly decreases, representing the lowest value among all oscillators. As the number of ribs increased, the pressure drop generally increased. However, the three-rib case showed a slight reduction, with the pressure drop decreasing.

Further increasing the number of ribs continues to impact the pressure drop. Overall, the results suggest that higher number of ribs increased the pressure drop. This behavior highlights the complex interaction between rib geometry and fluid dynamics in influencing the pressure loss across the oscillator. With an increase in the number of ribs on the Coanda surface, the rib height decreases. This reduction in rib height influenced greater jet attachment to both the ribs and the Coanda surface. This extension in jet attachment is driven by the extended separation bubble length near the ribs on the opposite side, as presented in the streamline plots for Case 6 Ribs in Fig. 5.2. When the number of ribs is lower, the jet has less contact with the Coanda surface. This reduced interaction minimizes friction along the Coanda surface, influencing the overall pressure drop. A lower number of ribs correlates with a reduced pressure drop. Among all the oscillator designs studied, the Case 1 Rib oscillator demonstrated the highest efficiency in minimizing pressure drop, achieving a 56.3% reduction compared to the smooth oscillator.

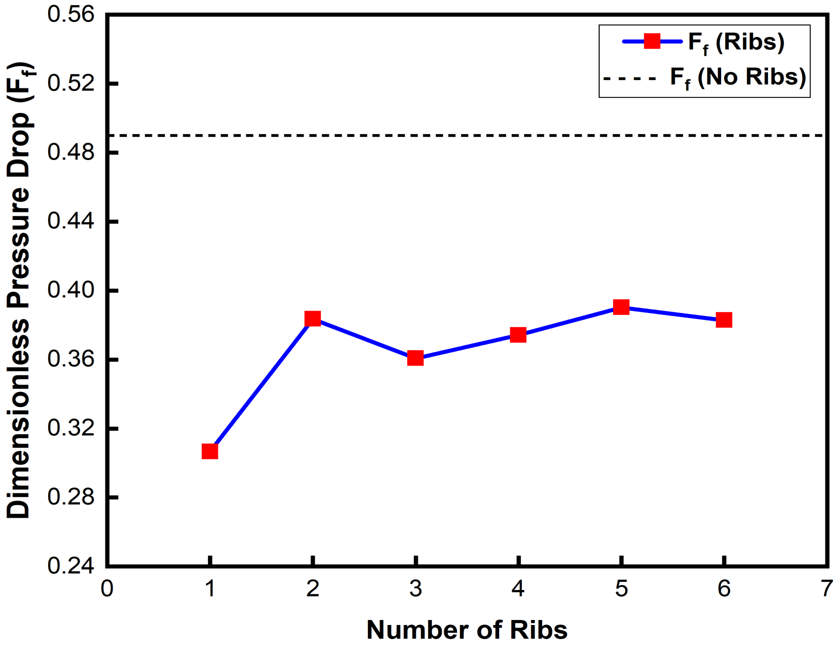

(a)

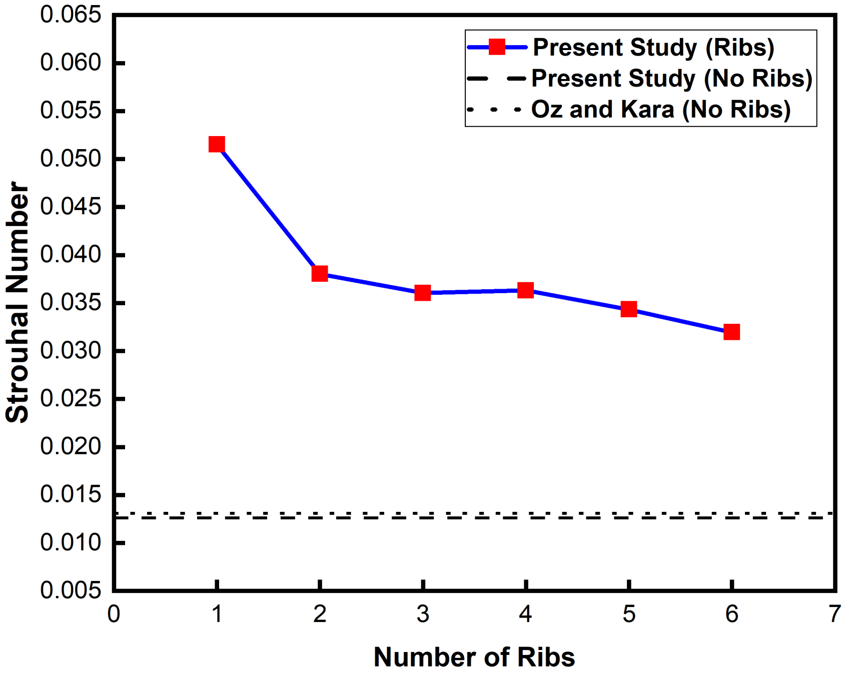

(b)

FIGURE 5.7: (a) Dimensionless pressure and (b) Strouhal number results, for oscillators with different number of ribs over the Coanda surface

For the Case 1 Rib, the pressure drop is the lowest because the single rib, despite its larger height, creates minimal flow disturbance. The pressure contours show relatively uniform pressure distribution, and the vorticity plots reveal weaker vortical structures. This results in lesser pressure drag, as the flow encounters fewer obstructions and experiences lower energy losses. The streamlined flow path and reduced vortical activity contribute to the minimal pressure drop. As the number of ribs increases to 2, 3, 4, 5, and 6 ribs, the pressure drop rises gradually.

The pressure contours begin to show localized regions of high and low pressure, while the vorticity plots indicate stronger vortical activity. These disturbances increase flow resistance and pressure drag, as the ribs introduce more obstructions and energy dissipation. The growing complexity of the flow field leads to higher pressure losses. Fig. 5.7(b) shows the Strouhal number, for jet oscillations across various numbers of rib configurations on the Coanda surface of the oscillator.

The behavior of the Strouhal number closely resembles with that of the oscillation frequency but contrasts with the trend observed for the dimensionless pressure drop. For ribbed oscillators, the Strouhal number is greater compared to the smooth oscillator.

In a previous study of Oz and Kara [83], an average Strouhal number of 0.0131 was obtained for smooth configurations under 2D compressible flow simulations across different mass flow rates. In the current study, the smooth case resulted in a slightly lower Strouhal number of 0.0126, which increased as the number of ribs decreased. Notably, the highest Strouhal number is achieved in Case 1 Rib.

5.3.2.4 Influence over Integrated Frequency and Deflection Angle Performance

The FDPR quantifies the integrated performance of the oscillator in terms of the frequency of the oscillating jet and the area it covers during oscillation. The results for jet performance parameter FDPR, are presented in Fig. 5.8 for different rectangular rib counts over the Coanda surface of the oscillator.

A higher FDPR value indicates a faster oscillation rate of the jet and a greater area covered while it is oscillating. As previously discussed, oscillation frequency and jet spreading are critical output parameters for oscillators used in flow control and thermal applications on heated surfaces. This performance parameter serves as an effective tool for identifying oscillators that achieve a higher combined effect of jet oscillation frequency and spreading with minimal pressure loss.

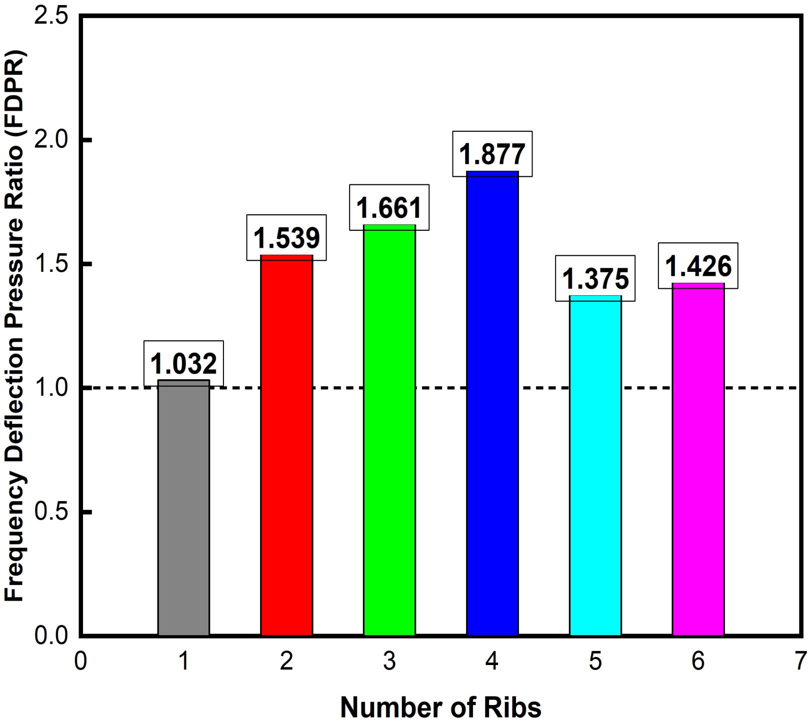

Figure 5.8: Frequency deflection angle-pressure ratio (FDPR) variations, for oscillators with various number of ribs on the Coanda surface

Among the cases of the oscillators examined, the configuration with Case 4 Ribs exhibited the highest FDPR, making it the most efficient oscillator in terms of flow performance. In contrast, Case 1 Rib is the least efficient configuration, exhibiting FDPR performance comparable to the smooth oscillator without ribs. It is important to note, however, that the lower FDPR in Case 1 Rib is attributed to its minimal jet deflection angle, whereas the smooth case's reduced FDPR is primarily driven by its lower oscillation frequency. The FDPR results aligned closely with the trends observed in jet deflection angle, showing an increase from

Case 1 Rib to Case 4 Ribs, followed by a decline. This observation shows the dominance of the jet deflection angle in governing the qualitative changes in FDPR. Additionally, compared to the reference smooth case with no ribs, Case 4 Ribs achieved a significant enhancement in FDPR, demonstrating an increase of 87.7%. The choice of rib configurations in fluidic oscillators depends on balancing key performance parameters like oscillation frequency, jet deflection angle, and pressure drop. Among the designs under consideration, the Case 4 Ribs has the highest FDPR value, showing the best balance of frequency, deflection angle and pressure performance. The Case 1 Rib design has the lowest pressure drop and highest oscillation frequency, making it energy efficient and suitable for applications like low power flow control or high frequency systems. For example, Woszidlo et al. [40] employed fluidic oscillators as sweeping jets for airfoil flow control, where rapid oscillations (critical for effective separation control) demonstrated significant potential for aerospace applications. However, its lower FDPR value means it may not perform as well in tasks requiring wider jet deflection or mixing. Designs with two to four ribs achieve an optimal balance between flow complexity and performance. The Case 4 Ribs oscillator, with the highest FDPR, is particularly effective for turbine blade cooling via sweeping jet impingement, where higher oscillation frequency combined with greater jet deflection enhances heat transfer performance and uniformity in cooling. As demonstrated by Joulaei et al. [141], such configurations successfully improved turbine cooling performance through precisely these mechanisms of enhanced oscillation frequency and jet deflection angle. For applications requiring strong vortical structures and mixing, the Case 5 Ribs and Case 6 Ribs oscillators are ideal. However, their lower FDPR values compared to the Case 4 Ribs indicate a trade-off between mixing performance and overall efficiency. Khalde et al. [157] utilized fluidic oscillator requiring vortex enhanced mixing and internal recirculation with design insights for optimization for their potential application in chemical and pharmaceutical industries. Using the FDPR performance parameter, the best rib configuration can be selected for their specific needs. The Case 4 Ribs design, with its highest FDPR, stands out as the most versatile option, offering a well-balanced performance across all key parameters.

5.4 Conclusion

The present research study is numerically conducted to investigate the impact of varying the number of Coanda surface ribs on the performance of a double feedback fluidic oscillator. The configurations included rib counts ranging from 1 to 6, introducing new geometries for evaluation. The internal flow behavior within the fluidic oscillator demonstrated that both the jet oscillating frequency and deflection angle were significantly influenced by the size of the recirculation bubble formed in the mixing chamber. For the Case 1 Rib oscillator, the recirculation bubble was considerably smaller.

As the number of ribs increased, the bubble size progressively grew. A smaller separation bubble reduced the resistance to the jet's transition between walls, thereby enhancing the oscillation frequency. Moreover, this study alongside frequency and jet deflection angle, evaluated the performance of oscillators using several key parameters, including the frequency to pressure drop ratio (FPR), jet deflection angle to pressure drop ratio (JDPR), dimensionless pressure drop, Strouhal number, and frequency deflection to pressure drop ratio (FDPR). Case 1 Rib, with the smallest separation bubble, achieves the highest frequency of 1160 Hz due to rapid jet switching. However, as the number of ribs increases, the separation bubble grows larger, slowing jet oscillations and reducing frequency. The smooth case results in the lowest frequency of 355 Hz. For FPR, Case 1 Rib performs the best, achieving the highest value, while the smooth case exhibits the lowest, underscoring the effectiveness of ribs in optimizing fluidic oscillator performance. Meanwhile, Case 4 Ribs provides the optimal ribbed configuration for maximizing the jet deflection angle at 37.1°, while excessive ribbing reduces effectiveness.

The smooth case, however, achieves the highest deflection angle of 53.3°, outperforming all ribbed configurations. The JDPR reflects the balance between jet spreading and pressure losses. The smooth Coanda surface achieves the highest JDPR due to its greater jet deflection angle. Among ribbed designs, Case 4 Ribs offers the best JDPR, though adding more ribs beyond this point reduces performance. The placement of ribs effectively reduces pressure drop compared to the smooth Coanda surface. Among all configurations, Case 1 Rib exhibited the lowest pressure drop, achieving a significant 56.3% reduction relative to the smooth oscillator. As the rib count increased, the pressure drop generally increased, highlighting the influence of rib geometry on flow resistance. Case 1 Rib emerged as the most efficient design for minimizing pressure drop. The Strouhal number is higher for ribbed oscillators (Case 1 Rib achieved the maximum), compared to the smooth case, reflecting enhanced jet oscillation dynamics. The FDPR reflects the combined impact of jet oscillating frequency and the area covered during oscillation. A higher FDPR indicates faster jet oscillation and a larger area affected. Among the oscillators studied, Case 4 Ribs outperformed all others, achieving the highest FDPR. It was 87.7% higher than the smooth oscillator, making it the most effective in terms of flow performance. On the other hand, Case 1 Rib showed the lowest FDPR, similar to the smooth surface oscillator, due to its reduced jet deflection angle. Case 4 Ribs demonstrated superior flow performance with the highest FDPR, highlighting its effectiveness in enhancing jet oscillation and coverage. This also indicates that an optimal rib configuration exists, consisting of 4 ribs for flow performance enhancement.

Chapter 6

Design Optimization of Ribbed Fluidic Oscillator Using Integrated CFD-Taguchi-GRA Method

6.1 Introduction

The previous chapters have demonstrated that the ribbed Coanda surface influence the flow performance of the double feedback oscillator. It was observed that he aspect ratio of the rib variations studied in Chapter 4 and the number of ribs variations studied in Chapter 5, enhanced the flow performance of the oscillator. In this chapter, the rib angle on the Coanda surface, along with the aspect ratio and the number of ribs, is optimized using a combination of CFD-Taguchi-Grey relational analysis.

The CFD-Taguchi-Grey relational analysis is a comprehensive and efficient optimization technique widely used for the optimization of single-objective functions. The main advantage of this approach is its capacity to generate robust and reliable designs while minimizing the number of required simulation-runs. This characteristic enhances its efficiency, making it a versatile, economical, and simple method for identifying optimal solutions in engineering applications. This study focuses on enhancing the Coanda surface by systematically altering three key geometrical parameters: the rib aspect ratio, the number of ribs, and the angle of ribs.

The objective is to advance the understanding of fluidic oscillator behavior by maximizing the oscillatory jet frequency and its lateral spreading. Improvements in these jet characteristics are anticipated to contribute significantly to increased heat transfer rates and an expanded effective cooling area in applications involving sweeping jet impingement.

To achieve this, a combined methodology incorporating Computational Fluid Dynamics, the Taguchi method, and Grey Relational Analysis is employed.

This hybrid approach facilitates the simultaneous optimization of multiple design variables and objectives. A notable strength of this technique lies in its ability to deliver consistent and high-performance design outcomes while significantly reducing the number of simulations required. Hence it is a cost-effective, efficient, and adaptable strategy for complex engineering optimization problems.

6.2 Taguchi Control Factors and Levels

To facilitate a comparative analysis of each design parameter, the levels of the three parameters are outlined in Table 6.1.

Additionally, we have chosen the orthogonal array L9 (3^3) for our trial simulation runs, as presented in Table 6.2, and the corresponding parameter matrix for these runs can be found in Table 6.3.

TABLE 6.1: Design factors and their levels for Taguchi design of experiment

Code	**Control factors**	**Level 1**	**Level 2**	**Level 3**
A	Aspect ratio	0.64	1	1.56
B	Number of ribs	4	6	8
C	Angle of ribs (°)	0	-18.5	18.5

Table 6.2: Taguchi orthogonal array (L9)

No. of simulation runs	**A**	**B**	**C**
1	1	1	1
2	1	2	2
3	1	3	3
4	2	1	2
5	2	2	3
6	2	3	1
7	3	1	3
8	3	2	1
9	3	3	2

Table 6.3: Taguchi orthogonal array geometries (L9) for the present study

No. of simulations	**Aspect ratio**	**Number of ribs**	**Angle of ribs (°)**
1	0.64	4	0
2	0.64	6	−18.5
3	0.64	8	18.5
4	1.00	4	−18.5
5	1.00	6	18.5
6	1.00	8	0
7	1.56	4	18.5
8	1.56	6	0
9	1.56	8	−18.5

6.3 Optimization of Design Parameters

6.3.1 Single Response Optimization

In this section, we will determine the optimal values for the three specified geometric parameters to compute the highest value of the output parameters; frequency, jet deflection angle, and pressure drop.

6.3.1.1 Optimization of Oscillation Frequency

The oscillation frequency results computed through Ansys Fluent and the related S/N ratios are presented in Table 6.4. The frequencies increase from a minimum of 730 Hz to a maximum of 845 Hz. The response table results for design factors aspect ratio, number of ribs, and angle of ribs, are presented in Table 6.5. The greater S/N ratio value in the response table corresponds to comparatively better oscillation frequency performance. The order of the contribution of design factors in optimizing the oscillation frequency of the fluidic oscillator designs is $numberofribs > aspectratio > angleofribs$.

It is evident from frequency S/N ratios results in Fig. 6.1, that the optimum design is with aspect ratio = 1.56, number of ribs = 4 and angle of ribs = 0°.

TABLE 6.4: Frequency results and corresponding S/N ratios obtained by numerical study and Taguchi method

Aspect ratio	**Number of ribs**	**Angle of ribs (°)**	**Frequency (Hz)**	**S/N ratio (dB)**
0.64	4	0	835	58.43
0.64	6	−18.5	790	57.95
0.64	8	18.5	730	57.27
1.00	4	−18.5	835	58.43
1.00	6	18.5	790	57.95
1.00	8	0	785	57.90
1.56	4	18.5	845	58.37
1.56	6	0	825	58.33
1.56	8	−18.5	800	58.06

The influence of the design factors; aspect ratio, number of ribs and angle of ribs, on oscillation frequency are analyzed by using ANOVA as shown in Table 6.6. ANOVA calculates the percentage contribution of design factors by examining

TABLE 6.5: Response table for frequency S/N ratios

Level	**Aspect Ratio**	**Number of Ribs**	**Angle of Ribs**
1	57.88	58.47	58.15
2	58.09	58.08	58.22
3	58.31	57.74	57.97
Delta	0.43	0.73	0.30
Rank	2	1	3

FIGURE 6.1: Graphical representation of Taguchi analysis main effects plot for S/N ratios of frequency results

factor variation, and using Taguchi analysis it confirms the reliability of the results. DF (Degrees of Freedom) denotes the independent comparisons that can be used to estimate variability in an ANOVA table. While Seq SS (Sequential Sum of Squares) displays the variation explained by each factor in sequence and Adj SS (Adjusted Sum of Squares) accounts for the variation after taking into account all factors. Contribution is the percentage of total variation that a design factor explains. Adj MS (Adjusted Mean Square) is the average variation per degree of freedom. The F-value compares its variation to error, while the P-value indicates the significance of a factor. The percentage of total variation described by the model is displayed as R-Sq (R-squared). The findings demonstrate that, with a 65.01% contribution and a p-value of 0.034 (less than 0.05), the number of ribs becomes the most important parameter to influence the oscillation frequency. The aspect ratio comes in second on the contribution list with 21.44% contribution, whereas the angle of the ribs claims minimal contribution and is not significant. The R-sq value indicates that the model is highly reliable, as it explains 97.68% of the total variation in the response variable. This suggests the model accurately represents the data, with minimal unexplained variability.

TABLE 6.6: Oscillation frequency – analysis of variance

Source	**DF**	**Seq SS**	**Contribution**	**Adj SS**	**Adj MS**	**F-value**	**P-value**
Aspect ratio	2	2205.6	21.44%	2205.6	1102.8	9.23	0.098
Number of ribs	2	6688.9	65.01%	6688.9	3344.4	28.00	0.034
Angle of ribs	2	1155.6	11.23%	1155.6	577.8	4.84	0.171
Error	2	238.9	2.32%	238.9	119.4	–	–
Total	8	10288.9	100.00%	–			

R-Sq = 97.68%

6.3.1.2 Optimization of Jet Deflection Angle

Table 6.7 displays the results of the jet deflection angle calculations made using Ansys Fluent along with the associated S/N ratios. The range of the jet deflection angle is 25.5° to 42.3°. Table 6.8 displays the findings of the response table for the design elements' aspect ratio, number of ribs, and angle of ribs of jet deflection angle. Comparatively superior jet deflection angle performance is indicated by a higher S/N ratio value in the response table. The sequence of the design parameters' contributions to the fluidic oscillator designs' optimization of the jet deflection angle is $angleofribs > aspectratio > numberofribs$ as shown in Table 6.8. Aspect ratio = 0.64, number of ribs = 6, and angle of ribs = -18.5° are the optimum values of the design factors, as can be seen from S/N ratios plots of jet deflection angle data displayed in Fig. 6.2. The optimum design for jet deflection angle is present in the Taguchi L9 array as simulation run 2.

Table 6.7: Jet deflection angle results and corresponding S/N ratios obtained by numerical study and Taguchi method

Aspect ratio	**Number of ribs**	**Angle of ribs (°)**	**Jet deflection angle (°)**	**S/N ratio**
0.64	4	0	33.2	30.42
0.64	6	-18.5	42.3	32.53
0.64	8	18.5	32.4	30.21
1.00	4	-18.5	39.5	31.93
1.00	6	18.5	26.2	28.37
1.00	8	0	28.8	29.19
1.56	4	18.5	25.5	28.13
1.56	6	0	30.3	29.63
1.56	8	-18.5	35.7	31.05

Table 6.8: Response table for jet deflection angle S/N ratios

Level	**Aspect ratio**	**Number of ribs**	**Angle of ribs**
1	31.05	30.16	31.84
2	29.83	30.17	29.75
3	29.60	30.15	28.90
Delta	1.45	0.02	2.93
Rank	2	3	1

Table 6.9: Jet deflection angle – analysis of variance

Source	**DF**	**Seq SS**	**Contribution** (%)	**Adj SS**	**Adj MS**	**F-value**	**P-value**
Aspect ratio	2	50.836	19.35	50.836	25.418	5.45	0.155
Number of ribs	2	0.629	0.24	0.629	0.314	0.07	0.937
Angle of ribs	2	201.982	76.86	201.982	100.991	21.64	0.044
Error	2	9.336	3.55	9.336	4.668	–	–
Total	8	262.782	100.00	–			

R-sq = 96.45%

ANOVA results for the effects of design factors on jet oscillation angle are presented in Table 6.9. The results show that the angle of ribs with 76.86% contribution and p-value of 0.044 has the most influence over the jet deflection angle variation and indicates statistical significance. Aspect ratio has 19.35% contribution and the influence of number of ribs is almost negligible. The reliability of the model is demonstrated by the 96.45% value of R-sq.

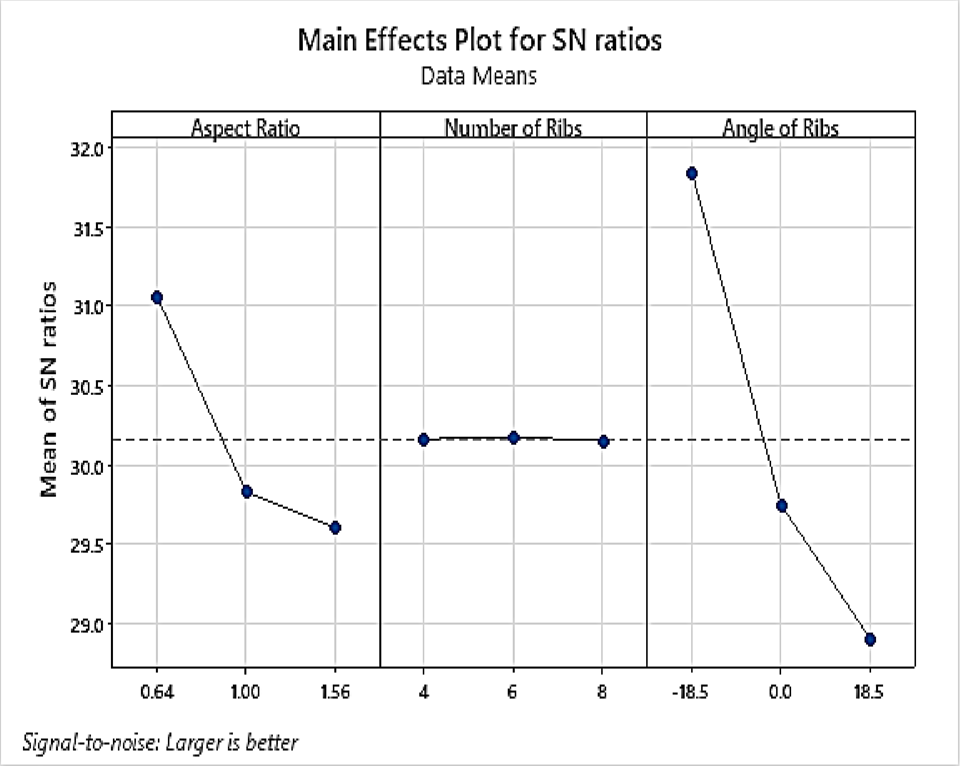

FIGURE 6.2: Graphical representation of Taguchi analysis Main effects plot for S/N ratios of jet deflection angle results

6.3.1.3 Optimization of Pressure Drop

The results for pressure drop across the oscillator computed through simulations and their corresponding S/N ratios calculated through Taguchi analysis are presented in Table 6.10. The results show that the minimum pressure drop is 20,609 Pa and the maximum pressure drop is 25,217 Pa. The response table having pressure drop S/N ratios of different design factors used in the study is presented in Table 6.11. The design factor aspect ratio has the most influence in optimizing the pressure drop, followed by number of ribs and angle of ribs respectively as per ranking in the response table. The pressure drop S/N ratios plot as shown in Fig. 6.3 demonstrates that the optimum levels of the design factors are aspect ratio = 1.56, number of ribs = 4 and angle ribs = 18.5°. The oscillator design with optimum levels of design factors falls inside the Taguchi L9 array as simulation run 7.

The ANOVA results analyzing the effect of design factors on the pressure drop are summarized in Table 6.12. These results show that the aspect ratio is the most

Table 6.10: Pressure drop results and corresponding S/N ratios obtained by numerical study and Taguchi method

Aspect ratio	**Number of ribs**	**Angle of ribs**	**Pressure drop (Pa)**	**S/N ratios**
0.64	4	0	24150	-87.66
0.64	6	-18.5	24675	-87.84
0.64	8	18.5	25217	-88.03
1.00	4	-18.5	23332	-87.36
1.00	6	18.5	23423	-87.39
1.00	8	0	24275	-87.70
1.56	4	18.5	20609	-86.28
1.56	6	0	21508	-86.65
1.56	8	-18.5	23660	-87.48

Table 6.11: Response table for pressure drop S/N ratios

Level	**Aspect ratio**	**Number of ribs**	**Angle of ribs**
1	-87.85	-87.10	-87.56
2	-87.49	-87.30	-87.34
3	-86.80	-87.74	-87.24
Delta	1.04	0.64	0.33
Rank	1	2	3

significant factor and contributes 65.93% to the change in pressure drop with a p-value of 0.041, indicating statistical significance. The number of ribs contributes for 25.43% of the variation, while the influence of the angle of ribs is very minimal. The model's high reliability is confirmed by an R-sq value of 97.22%, demonstrating its ability to effectively explain the observed variability.

Table 6.12: Pressure drop – analysis of variance

Source	**DF**	**Seq SS**	**Contribution** (%)	**Adj SS**	**Adj MS**	**F-value**	**P-value**
Aspect ratio	2	11664042	65.93	11664042	5832021	23.68	0.041
Number of ribs	2	4498118	25.43	4498118	2249059	9.13	0.099
Angle of ribs	2	1035704	5.85	1035704	517852	2.10	0.322
Error	2	492584	2.78	492584	246292	–	–
Total	8	17690448	100.00		–		

R-sq = 97.22%

FIGURE 6.3: Graphical representation of Taguchi analysis Main effects plot for S/N ratios of Pressure Drop results

6.3.2 Multiple Response Optimization Using the Weighted Grey Relational Grade

The responses achieved through CFD simulation results provided in Table 6.13(a):, including frequency, jet deflection angle, and pressure drop, followed by data pre-processing using GRA. Firstly, the responses are normalized as shown in Table 6.13(b) using Eq. 3.17 for frequency and jet deflection angle and Eq. 3.18 for pressure drop. The deviation sequences shown in Table 6.13(b) are then calculated. Next, the GRC for each response value is computed using Eq. 3.19 as presented in Table 6.13(b). Lastly, the GRG is obtained by averaging the GRC. The GRG data as shown in Table 6.16 served as the foundation for the overall assessment of the various performance parameters. The highest rank is given to the grade with the highest value.

Table 6.15 presents the geometric mean and normalized weights obtained through Eq. 3.23 and Eq. 3.24 from the pairwise matrix of Table 6.14. Eq. 3.25 is used

TABLE 6.13: Simulation results and GRC analysis for Taguchi L9 array

(a) Simulation results for all responses

Run	**Aspect ratio**	**Number of ribs**	**Angle of ribs**	**Frequency (Hz)**	**Jet deflection angle (°)**	**Pressure drop (Pa)**
Run 1	0.64	4	0	835	33.2	24150
Run 2	0.64	6	-18.5	790	42.3	24675
Run 3	0.64	8	18.5	730	32.4	25217
Run 4	1.00	4	-18.5	835	39.5	23332
Run 5	1.00	6	18.5	790	26.2	23423
Run 6	1.00	8	0	785	28.8	24275
Run 7	1.56	4	18.5	845	25.5	20769
Run 8	1.56	6	0	825	30.3	21508
Run 9	1.56	8	-18.5	800	35.7	23660

(b) Normalization, deviation, and grey relational coefficients (GRC)

Run	**Norm. freq**	**Norm. angle**	**Norm. press**	**Dev. freq**	**Dev. angle**	**Dev. press**	**GRC freq**	**GRC angle**	**GRC press**
Run 1	0.9130	0.4583	0.2399	0.0870	0.5417	0.7601	0.8519	0.4800	0.3968
Run 2	0.5217	1.0000	0.1219	0.4783	0.0000	0.8781	0.5111	1.0000	0.3628
Run 3	0.0000	0.4107	0.0000	1.0000	0.5893	1.0000	0.3333	0.4590	0.3333
Run 4	0.9130	0.8333	0.4238	0.0870	0.1667	0.5762	0.8519	0.7500	0.4646
Run 5	0.5217	0.0417	0.4033	0.4783	0.9583	0.5967	0.5111	0.3429	0.4559
Run 6	0.4783	0.1964	0.2118	0.5217	0.8036	0.7882	0.4894	0.3836	0.3881
Run 7	1.0000	0.0000	1.0000	0.0000	1.0000	0.0000	1.0000	0.3333	1.0000
Run 8	0.8261	0.2857	0.8339	0.1739	0.7143	0.1661	0.7419	0.4118	0.7506
Run 9	0.6087	0.6071	0.0578	0.3913	0.3929	0.9422	0.5610	0.5600	0.3467

to calculate the pairwise comparison matrix's consistency index. By adding up the relative scores column-wise, multiplying them by the appropriate normalized weights of the responses, and then adding up the results, the value of $\lambda_{\max}$ is determined.

The computed value of $\lambda_{\max}$ in this investigation is 3.0026, resulting in a CI of 0.0013. Eq. 3.26 is then used to calculate the matrix's consistency ratio. A random index (RI) of 0.52 for N = 3 for the three responses is used. For this study, the final CR value is 0.0025. The CR value obtained from the pairwise comparison matrix is used to evaluate the consistency of the judgments; a CR value of 0.1 or less is typically regarded as acceptable, suggesting that the judgments made in this study are dependable and consistent.

The normalized weights obtained using Pairwise matrix of Table 6.14 and from the AHP as indicated in Table 6.15 are used to compute the WGRG for each simulation run, which is displayed in Table 6.16. The following weighted sum of the GRCs is used to calculate the WGRGs

$$WGRG = 0.777\, GRC_{Frequency} + 0.111\, GRC_{Jet\, Deflection\, Angle} + 0.111\, GRC_{Pressure\, Drop}$$

Table 6.14: Pairwise matrix table obtained using Saaty scale

Responses	**Frequency**	**Jet deflection angle**	**Pressure drop**
Frequency	1	7	7
Jet deflection angle	1/7	1	1
Pressure drop	1/7	1	1

Table 6.15: AHP geometric means and normalized weights

Responses	**Geometric mean**	**Normalized weights**
Frequency	3.65	0.777
Jet deflection angle	0.52	0.111
Pressure drop	0.52	0.111

This method made it possible to quantify each simulation run's relative performance using the weighted contribution of each factor.

Table 6.17 presents the findings of the integrated creation of the WGRG response table for the factors, aspect ratio, number of ribs, and angle of ribs.

The WGRG level having the highest S/N ratio value is the optimum one. When it comes to optimizing oscillator flow performance, the WGRG ranks the design elements as follows: number of ribs > angle of ribs > aspect ratio. The optimum design is aspect ratio = 1.56; number of ribs = 4; and angle of ribs = 0° based on the examination of the S/N ratio of WGRG as shown in Fig. 6.4.

ANOVA results show that the WGRG is influenced by the factors aspect ratio, number of ribs, and angle of ribs by 17.77%, 78.84%, and 1.89%, respectively, as presented in Table 6.18. The ANOVA also demonstrated that the number of ribs contributed the greatest percentile to the WGRG. In accordance with the findings

Table 6.16: GRG and WGRG results for Taguchi L9 array

	Grey relational grade (GRG)		Weighted grey relational grade (WGRG)	
Run	**GRG**	**Rank**	**WGRG**	**Rank**
Run 1	0.5762	5	0.7592	3
Run 2	0.6246	4	0.5484	5
Run 3	0.3752	9	0.3470	9
Run 4	0.6888	2	0.7967	2
Run 5	0.4366	7	0.4858	7
Run 6	0.4204	8	0.4659	8
Run 7	0.7778	1	0.9250	1
Run 8	0.6348	3	0.7055	4
Run 9	0.4892	6	0.5365	6

Table 6.17: Response table for WGRG S/N ratios

Level	**Aspect ratio**	**Number of ribs**	**Angle of ribs**
1	-5.602	-1.681	-4.200
2	-4.960	-4.840	-4.019
3	-3.038	-7.079	-5.381
Delta	2.563	5.398	1.362
Rank	2	1	3

obtained from the Taguchi technique, the significance order of the studied design factors is established as number of ribs > angle of ribs > aspect ratio.

6.3.3 Confirmatory Test

The objective of the confirmatory test is to verify the conclusion reached through the Taguchi-GRA analysis stage. The results for the confirmation test are presented in Table 6.19. The optimal design for oscillation frequency as obtained in Section 6.3.1.1 is not present in the L9 array, so further simulation as simulation run 10 are performed for the design with optimum levels. The predicted value of the oscillation frequency at the optimum levels of the design factors is 868.9 Hz and

FIGURE 6.4: Graphical representation of Taguchi analysis main effects plot of S/N ratios for WGRG results

TABLE 6.18: WGRG – analysis of variance

Source	**DF**	**Seq SS**	**Contribution (%)**	**Adj SS**	**Adj MS**	**F-value**	**P-value**
Aspect ratio	2	0.049630	17.77	0.049630	0.024815	11.88	0.078
Number of ribs	2	0.220243	78.84	0.220243	0.110122	52.73	0.019
Angle of ribs	2	0.005292	1.89	0.005292	0.002646	1.27	0.441
Error	2	0.004176	1.50	0.004176	0.002088	–	–
Total	8	0.279341	100.00		–		

R-Sq = 98.50%

the actual value of oscillation frequency obtained through CFD simulation run 10 is 875 Hz. The error between the predicted and actual value for the optimum design is 0.69%.

Fig. 6.5 (a) shows the frequency results for the optimum simulation run 10 and all the Taguchi L9 array 9 simulation runs alongside simulation run 11. The frequency for the optimum run 10 is 3.55% higher than the second highest run 7 and 19.9% higher than run 3 with the lowest frequency. For the jet deflection angle presented

Table 6.19: Confirmation test results for optimum designs

Response	**Oscillator design**	**Sim. run**	**Predicted value**	**Actual value (CFD)**	**Diff. (%)**
Frequency (Hz)	Aspect ratio = 1.56, number of ribs = 4, angle of ribs = 0°	Run 10	868.9	875	0.69
Jet deflection angle (deg)	Aspect ratio = 0.64, number of ribs = 6, angle of ribs = −18.5°	Run 2	42.8	42.3	1.17
Pressure drop (Pa)	Aspect ratio = 1.56, number of ribs = 4, angle of ribs = 18.5°	Run 7	20,850	20,769	0.39
WGRG	Aspect ratio = 1.56, number of ribs = 4, angle of ribs = 0°	Run 10	0.955	0.945	1.05

in Section 6.3.1.2 and pressure drop presented in Section 6.3.1.3, the optimum levels already exist in the Taguchi L9 array as simulation run 2 and simulation run 7 respectively. The predicted jet deflection angle at the optimal levels of the design factors is 42.8°, while the actual jet deflection angle determined by CFD simulation is 42.3°. For the optimum design, there is a 1.17% discrepancy between the predicted and actual values. Fig. 6.5 (b) presents the jet deflection angle results for all the L9 array simulations and run 10. The jet deflection angle is 6.6% higher for the optimum run 2 as compared to run 4 with the second highest deflection angle and it achieves an increase of 39.7% of jet spreading when compared to the lowest jet deflection angle run 7.

The Taguchi analysis predicted the optimal value of pressure drop to be 20,850 Pa and the actual pressure drop value obtained through CFD simulations is 20,769 Pa giving a difference of 0.4%. Fig. 6.6 (a) shows the pressure drop results for all the simulation runs. The pressure drop for optimum run 7 experienced a reduction of 1.2% from the second lowest pressure drop of run 10 and a reduction of 17.6% from the highest pressure drop of run 3.

Since the L9 array does not contain the optimal design for multi-objective optimization response WGRG, but it's the same as the optimum frequency simulation run 10. The actual value of the WGRG, as determined by CFD simulation run 10, is 0.955, while the predicted value at the optimal levels of the design factors is 0.945. Fig. 6.6 (b) shows the highest WGRG value of simulation run 10 is 0.945 and it is higher than the Taguchi L9 array's highest WGRG value of 0.925 obtained in simulation 7.

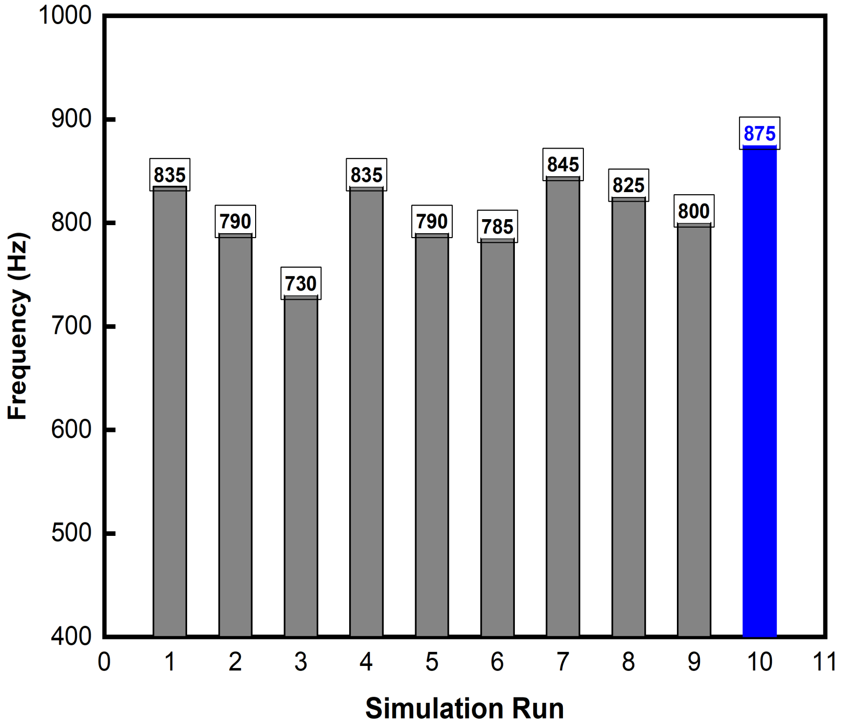

(a)

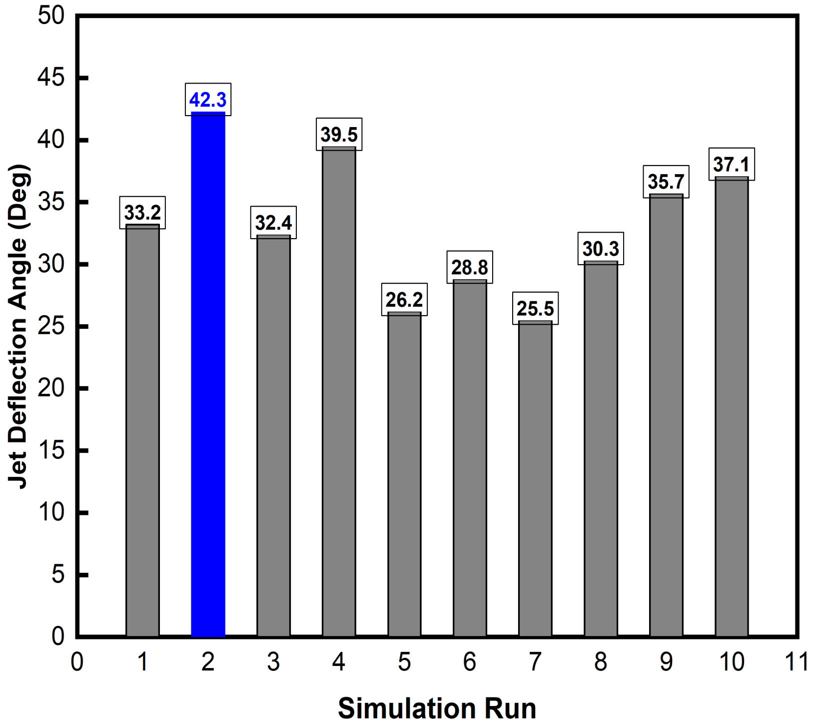

(b)

FIGURE 6.5: Frequency and deflection angle results for all simulation runs

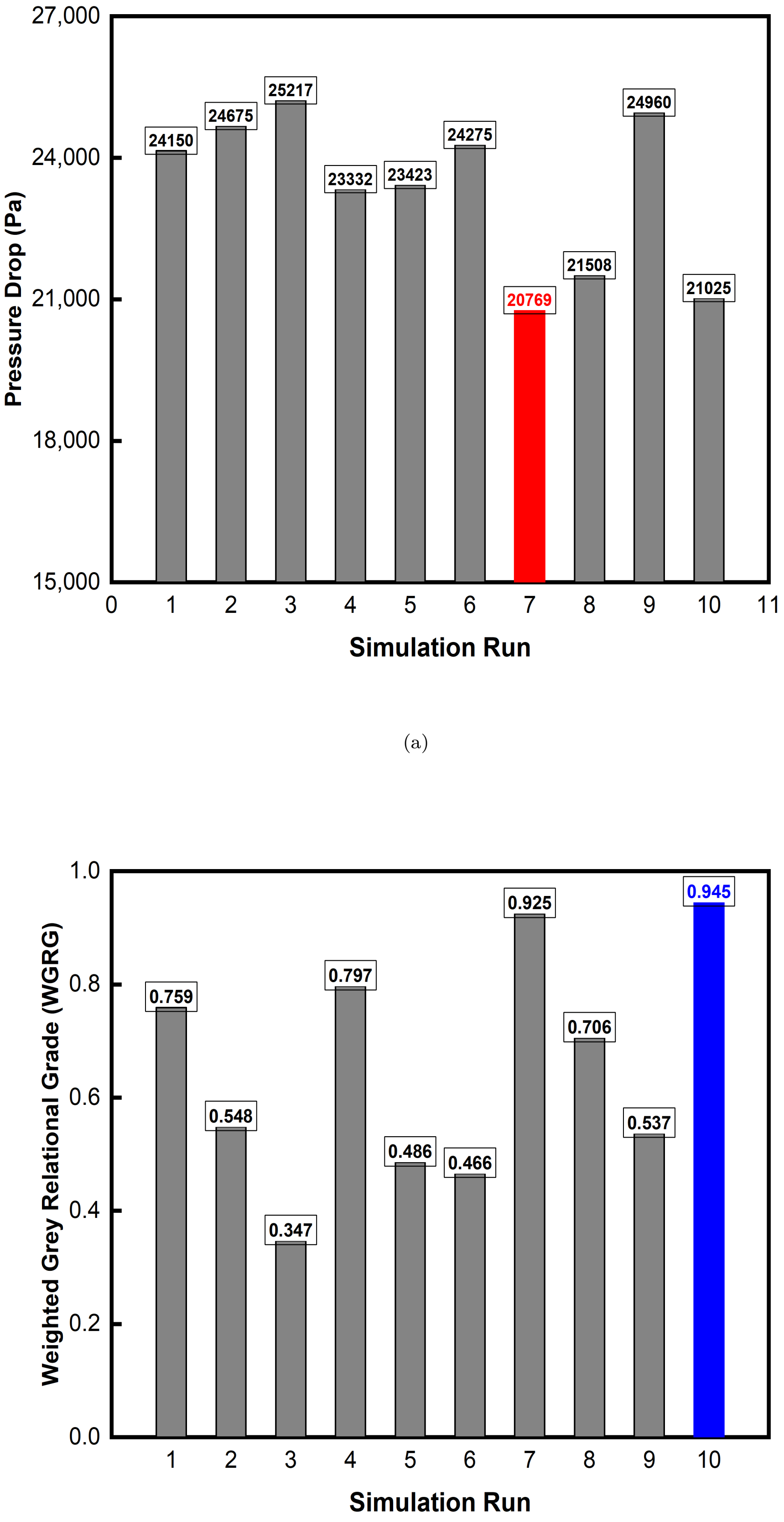

(a)

(b)

Figure 6.6: Pressure drop and WGRG results for all simulation runs

6.3.4 Internal Flow Dynamics of Fluidic Oscillators

In this section, the internal flow dynamics of the oscillators with optimized results will be discussed and compared to a reference oscillator with a smooth Coanda surface. As discussed in previous chapters, when the jet passes through the supply nozzle and enters the mixing region of a double-feedback fluidic oscillator, even minor flow disturbances generate a pressure difference along the walls of the mixing region.

This pressure difference triggers the Coanda effect, where the jet is drawn toward and attaches to one of the walls. As the jet moves progressively closer to the wall, the Coanda effect intensifies, eventually leading to full jet attachment. Complete attachment corresponds to a phase angle of $\phi = 0°$, indicating that both the inlet and outlet jets are in phase, resulting in zero deflection at the exit throat. Meanwhile, some part of the jet flows into the feedback channel. Moving through the feedback, it returns and interacts with the main jet entering through the supply nozzle. This interaction forces the main jet to detach from the initial wall, redirecting it toward the opposite wall. When the jet fully transitions to the opposite wall, it corresponds to a phase angle of 180°. The jet oscillates symmetrically, progressing through phase angles ϕ of 0°, 45°, 90°, 135°, and 180°, which represent half of the oscillation cycle. The cycle repeats in a symmetrical manner, ensuring a continuous oscillating motion of the jet. After the internal switching completes, the oscillating jet generates a sweeping action in the external domain.

Fig. 6.7 presents the streamline plots for both the reference smooth oscillator and the optimized oscillator designs, specifically for Simulation Run 2, Simulation Run 7, and Simulation Run 10. The streamline plots reveal that at $\phi = 0°$, the jet entering the mixing chamber attaches to one side of the Coanda surface, forming a primary separation bubble near the opposite Coanda surface. Among the examined designs, the smooth oscillator produces the largest separation bubble and lowest oscillation frequency (355 Hz), while Simulation Run 10 of the optimized design results in the smallest bubble and highest oscillation frequency (875 Hz). A smaller separation

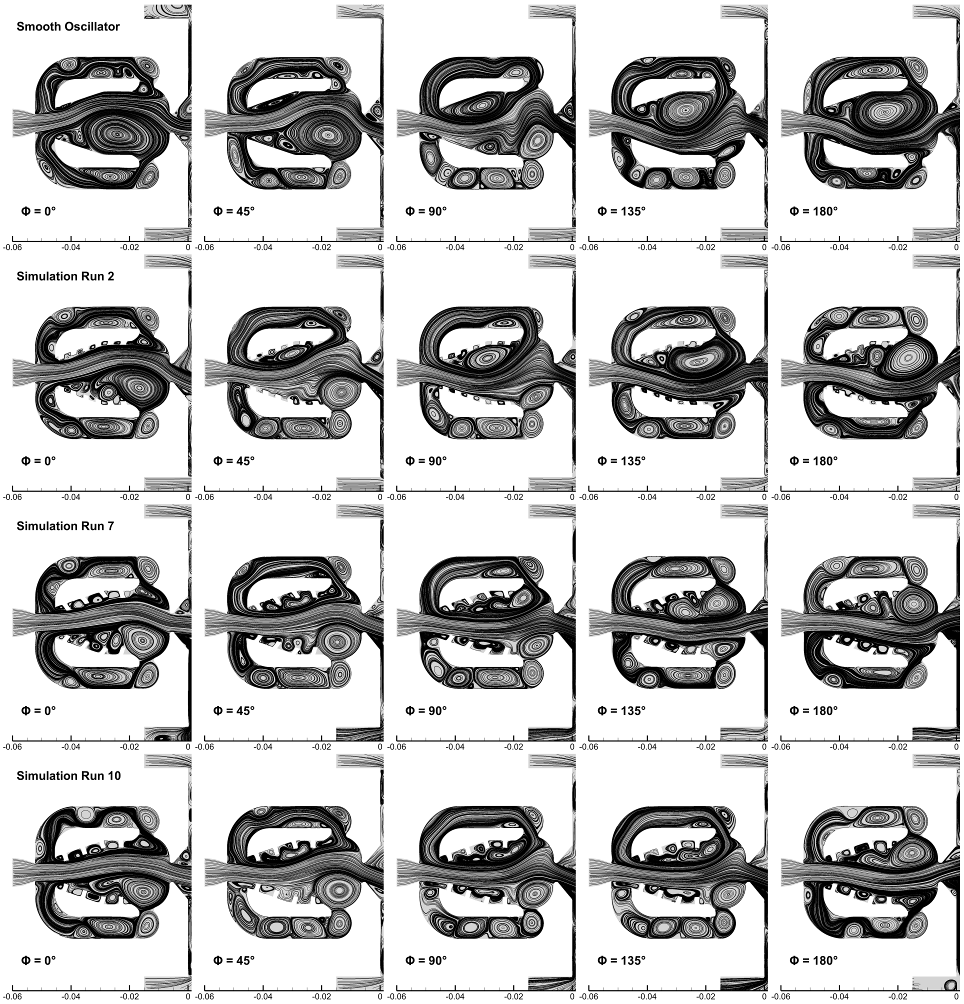

Figure 6.7: Streamline plots for optimum designs and smooth oscillator at different phase angles

bubble facilitates faster switching of the jet from one wall to the other, thereby enhancing the oscillation frequency. In this regard, Simulation Run 7 generates the second smallest bubble and consequently the second highest oscillation frequency, followed by Simulation Run 2 and then smooth oscillator. The size of the primary separation bubble is greatly influenced by the number of ribs and the aspect ratio. A lower number of ribs combined with a higher aspect ratio leads to a minimal separation bubble size. Conversely, introducing tilted ribs increases the bubble size. When the number of ribs is less and the aspect ratio is high without any rib tilt, the flow passage within the mixing chamber becomes more narrowed, resulting in an elevated jet velocity. This increase in velocity compresses the separation bubble, as depicted in Simulation Run 10. Additionally, the presence of ribs in the mixing chamber deflects the jet from the Coanda surface, preventing its attachment. This deflection further contributes to reducing the separation bubble size. On the other hand, as the number of ribs rises and the aspect ratio lowers, the jet deflection diminishes, leading to the creation of a larger separation bubble on the opposite side and consequently a lower oscillation frequency as shown by smooth oscillator design.

In Simulation Run 2, the jet experiences the highest jet deflection angle among the ribbed oscillators as it can be observed that the jet moves nearer the Coanda surface, exiting the oscillator at a higher spread angle. The closer movement toward the Coanda surface is supported by a higher number of ribs and a lower aspect ratio, making wider space for the jet but at the expense of creating a larger separation bubble on the opposite side. At a phase angle of $\phi = 45°$, the feedback channel jet flow rejoins the main flow and initiates a deflection of the main jet toward the opposite wall. As the phase angle advances to $\phi = 90°$ and $\phi = 135°$, a similarly shaped separation bubble starts to emerge on the opposite side across all designs. By $\phi = 180°$, the development of this identical separation bubble on the opposite side is complete for each design. At this point, the flow reattaches to the opposing side, signifying the half of the jet oscillation cycle.

Fig. 6.8 (a) illustrates pressure contours at a phase angle $\phi = 0°$ for the reference smooth oscillator and optimized designs; Simulation Run 2, Simulation Run 7 (optimized for minimal pressure drop), and Simulation Run 10.

The pressure distribution within the oscillators indicates varying flow behaviors based on the design variations. The smooth oscillator exhibits a relatively low overall pressure range, with a substantial low-pressure region formed in the mixing chamber and feedback channels. In contrast, simulation run 2, which has 6 number of ribs on each side, demonstrates a noticeable increase in overall pressure, accompanied by low-pressure region size squeezing. Simulation Run 7, optimized for pressure drop, presents an intermediate behavior where the balance between pressure rise and bubble formation leads to stable jet oscillations. Here, the low-pressure zone's size directly influences the separation bubble, which plays a critical role in governing the flow dynamics. Finally, Simulation Run 10 shows almost similar pressure

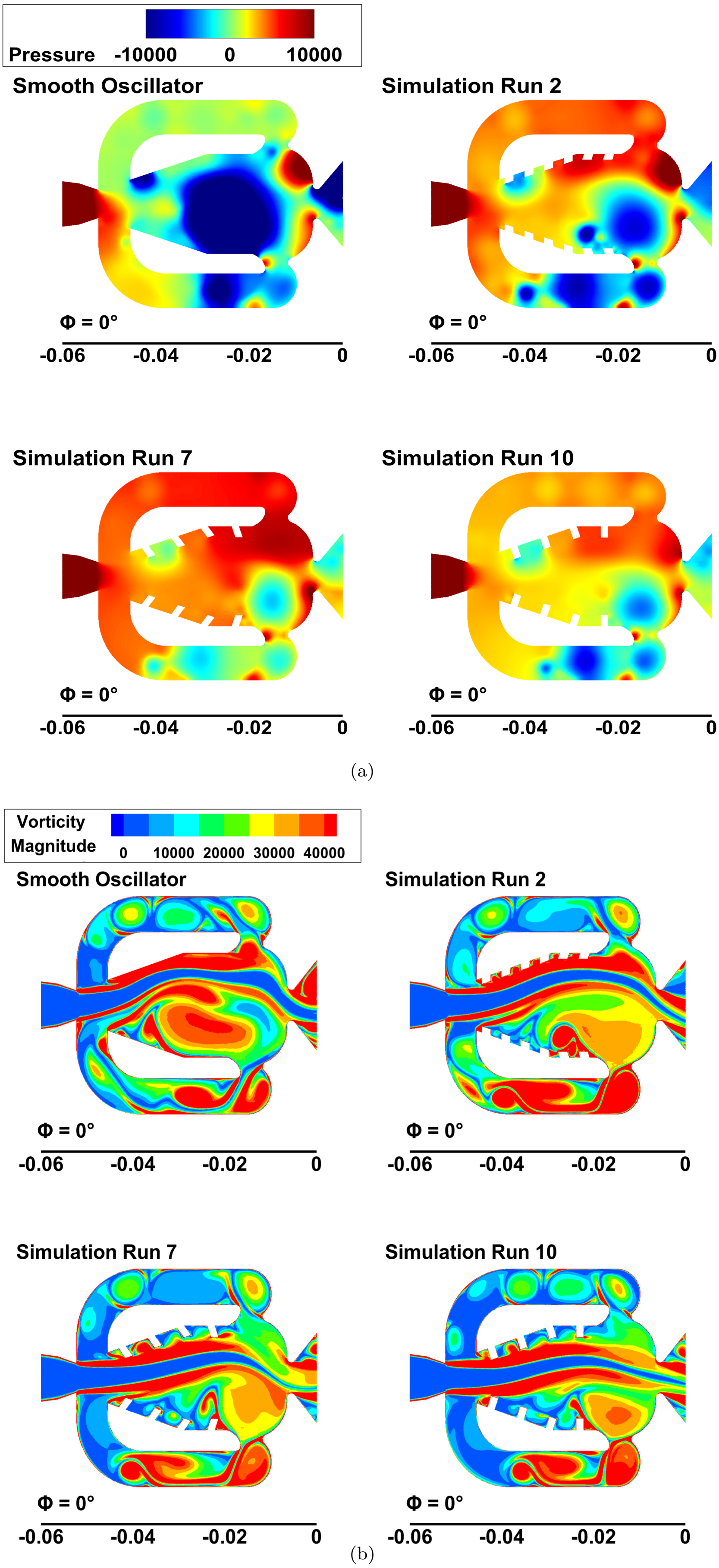

(a)

(b)

FIGURE 6.8: (a) Pressure contours (b) Vorticity magnitude contours plots; for optimum designs and smooth oscillator at $\Phi = 0°$

behavior across the system. Overall, these pressure contours highlight the intricate relationship between rib geometry and the resulting flow characteristics in different oscillator designs. The optimum pressure drop in Simulation Run 7 results from its lower number of ribs, higher aspect ratio, and rib geometry with an 18.5° tilt in the flow direction, which reduces jet attachment to the Coanda surface as depicted through streamline plots as well. The design promotes early flow detachment from the Coanda surface, decreasing pressure drag and overall pressure losses. Compared to the smooth oscillator, where stronger jet attachment to the Coanda surface causes higher pressure drag, the enhanced detachment in Run 7 ensures smoother jet switching and more efficient pressure recovery, leading to lower pressure drop.

Fig. 6.8 (b) shows vorticity magnitude contours at $\phi = 0^\circ$ for different oscillator designs. In Simulation Run 2, ribs along the Coanda surface create localized high-vorticity zones, causing jet deflection toward one side of the mixing chamber, forming the largest bubble size compared to other ribbed designs. Simulation Run 7, with tilted ribs, reduces bubble size as the jet is directed more towards the center by high vorticity guiding flow on both sides. Similarly, Simulation Run 10 displays the smallest separation bubble, as the jet is pushed further toward the center by the high vorticity guides on both sides. These results highlight how rib geometry influences vorticity distribution, separation bubble formation, and jet oscillation dynamics.

In Simulation Run 2, the pressure contours show a higher pressure gradient near the Coanda surface, indicating better flow attachment and control. This optimized pressure distribution helps steer the jet more effectively, resulting in the observed 39.7% improvement in jet deflection angle. The vorticity magnitude contours reveal stronger vortical structures near the Coanda surface, which enhance momentum exchange between the main jet and the feedback flows. The ribs on the Coanda surface create localized high-pressure regions and controlled vortices that maintain flow coherence and enhance jet steering. For Simulation Run 7, the pressure contours reveal a smoother and more uniform pressure distribution compared to the baseline design, indicating reduced pressure drag on Coanda surface and energy losses due to the tilted ribs in the direction of main jet flow. This contributes to the 17.6% reduction in pressure drop. The vorticity contours show a more uniform distribution of vorticity, further supporting the reduction in turbulence and energy dissipation. The ribs help streamline the flow, minimizing chaotic vortical structures and optimizing energy transfer within the oscillator. In Simulation Run 10, the pressure contours show distinct pressure differentials across the feedback channels, which are critical for driving the oscillation mechanism. The ribs enhance pressure recovery, leading to a more stable and rapid oscillation cycle. The vorticity contours exhibit well defined vortical patterns, particularly in the feedback channels, which promote faster switching of the jet between the channels. Additionally, the smaller separation bubble in the mixing chamber, as indicated by both pressure and vorticity distributions and streamline plots, reduces flow resistance and allows for quicker transitions, contributing to the 19.9% increase in oscillation frequency. The pressure and vorticity contours demonstrate that the ribbed Coanda surface improves performance by optimizing pressure distribution, generating controlled vortical structures, and reducing pressure drag. These mechanisms, along with the smaller separation bubble in the mixing chamber, collectively explain the significant improvements in oscillation frequency, jet deflection angle, and pressure drop observed in the optimized designs.

6.3.5 Conclusion

A comprehensive study is conducted to optimize the flow performance of a double-feedback fluidic oscillator by integrating computational fluid dynamics (CFD) modeling with the Taguchi-Grey relational analysis approach. The design factors aspect ratio, number of ribs, and angle of the rib are analyzed at three distinct levels: 0.64, 1.00, and 1.56; 4, 6, and 8; and $0°$, $-18.5°$ and $+18.5°$ respectively, to assess their influence on oscillation frequency, jet deflection angle, and pressure drop. The conclusions drawn from this research are summarized as follows:

The analysis of the Taguchi orthogonal array revealed that the number of ribs is the most significant factor affecting the oscillation frequency and overall oscillator performance. ANOVA results indicated a 65.01% contribution of the number of ribs in maximizing the frequency. The oscillation frequency of 875 Hz for the optimum design Simulation Run 10 is found to be higher by 19.9% as compared to other designs. The angle of the ribs exhibited a dominant influence on the jet deflection angle. According to the ANOVA table the angle of ribs contributed 76.86% in maximizing the jet spreading angle. The jet deflection angle is increased for the optimum Simulation Run 2 by 39.7%. The aspect ratio played a crucial role in minimizing the pressure drop. The contribution of the aspect ratio in minimizing the pressure drop is 65.93% as per ANOVA results. The pressure drop for the optimum design Simulation Run 7 is reduced by 17.6%. The Grey Relational Analysis, coupled with the Analytical Hierarchy Process for weight determination, confirmed these findings and provided a robust framework for achieving multi-objective optimization. Analysis of variance (ANOVA) highlighted the statistical significance of the design factors. The optimized design parameters successfully enhanced the flow performance of the fluidic oscillator, demonstrating the effectiveness of the proposed methodology in achieving multi-objective optimization for advanced fluidic systems. The analysis of internal flow dynamics in fluidic oscillators highlights significant differences between the optimized designs and a reference oscillator with a smooth Coanda surface. The comparison of streamline plots, which highlight separation bubble formation, demonstrates that optimized designs significantly enhance oscillatory performance by forming smaller separation bubbles. For instance, Simulation Run 10 achieves the highest oscillation frequency (875 Hz) and smallest separation bubble size, attributed to a low number of ribs and a high aspect ratio. These parameters narrow the flow passage, increasing jet velocity and compressing the separation bubble. Conversely, the smooth oscillator produces the largest bubble and lowest frequency (355 Hz), highlighting its lower efficiency. A higher rib count and reduced aspect ratio increase jet deflection but create larger bubbles on the opposite side, reducing oscillation frequency. Simulation Run 7, enhances performance by promoting early jet detachment and minimizing pressure losses through tilted ribs and a higher aspect ratio. These findings underscore the influence of geometric parameters, such as the number of ribs, aspect ratio, and angle of ribs, on jet dynamics and oscillation behavior in fluidic oscillator design.

Chapter 7

Taguchi-based Optimization of a Fluidic Oscillator for Enhanced Thermal-Hydraulic Performance of an Impinging Sweeping Jet

7.1 Introduction

Following the geometric optimization of Coanda surface ribs, where aspect ratio and number of ribs were first analyzed (Chapter 4 and Chapter 5) and subsequently refined through a combined CFD-Taguchi-Grey relational approach to optimize oscillation frequency and jet deflection angle (Chapter 6), this chapter presents the results of the thermal performance analysis of the two novel optimized ribbed designs.

A Taguchi-designed parametric study examines the interplay between rib configuration (frequency optimized and jet deflection optimized), jet to target surface distance, hot target surface length, and Reynolds number (Re) to quantify their collective impact on heat transfer enhancement. The thermal performance of each ribbed oscillator is benchmarked against a smooth surfaced baseline, utilizing heat

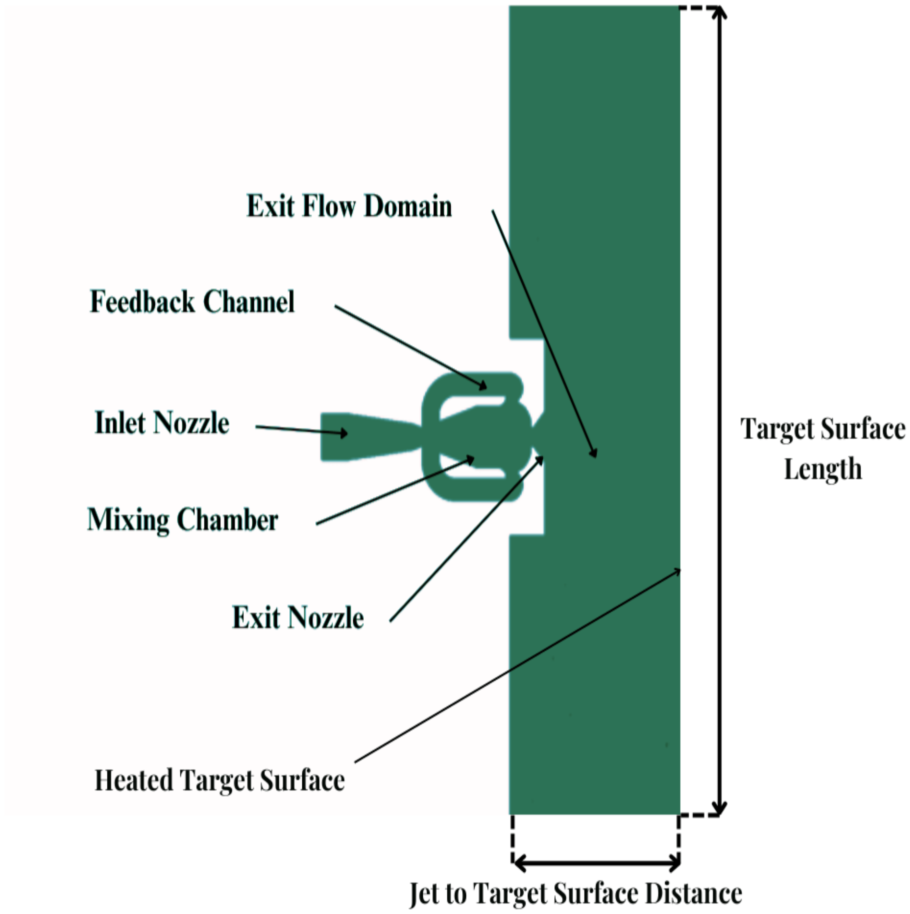

FIGURE 7.1: Computational domain for heat transfer analysis

transfer simulations to resolve Nusselt number distributions on the hot target surface. The throat sizes at the inlet and exit points are maintained uniformly in every configuration and the computational domain is presented in Fig. 7.1.

Furthermore, the investigation explores how changes in Reynolds number, the spacing between the jet and the target plate, and the length of the impingement hot surface affect thermal performance. The thermal efficiency outcomes of the newly developed oscillator configuration are evaluated against those obtained using a conventional smooth Coanda profile oscillator.

A Taguchi-based optimization technique is utilized to methodically enhance the thermal exchange characteristics of the fluidic oscillator setup under investigation. The outcomes seek to offer a deeper understanding of thermal optimization for oscillators with ribbed surfaces and to clarify the correlation between oscillation frequency and improvements in heat transfer.

7.2 Problem Formulation

7.2.1 Taguchi Factors and Levels for Heat Transfer Analysis

In heat transfer analysis, four parameters at three different levels, oscillator design group (OG1, OG2, and OG3), Reynolds number (85,500; 101,000; and 114,600), jet-to-target surface distance (2, 4, and 6), and the length of the target surface (20, 30, and 40) are studied as depicted in Table 7.1. The Reynolds number, defined as

$$\mathrm{Re} = \frac{V_e D}{\nu},$$

is calculated using the velocity and diameter of the exit throat. The oscillator design group comprises a smooth oscillator (HT0), an optimum design of oscillator based on jet deflection angle (HT1), and an optimum design of oscillator based on oscillation frequency (HT2).

These are grouped to assess the enhancement in heat transfer for each optimum design relative to the smooth oscillator across all simulation runs.

Specifically, oscillator design group OG1 includes HT0-HT1-HT2, OG2 includes HT0-HT2-HT1, and OG3 includes HT1-HT0-HT2 oscillators.

The Taguchi L9 orthogonal array, structured as a 3^4 (four factors, each at three levels) design, indicating the simulation runs for heat transfer analysis is presented in Table 7.2.

Table 7.1: Design factors and their levels for Taguchi design of experiment—heat transfer analysis

Control factors	**Level 1**	**Level 2**	**Level 3**
Oscillator design group	OG1	OG2	OG3
Jet-to-target distance (H/D)	2	4	6
Reynolds number	85,500	101,000	114,600
Target surface length (L/D)	20	30	40

Table 7.2: Taguchi orthogonal array geometries (L9) for heat transfer analysis

HT sim. run	**Oscillator design group**	**Jet-to-target distance (H/D)**	**Reynolds number**	**Target surface length (L/D)**
HT simulation 1	OG1	2	85,500	20
HT simulation 2	OG1	4	101,000	30
HT simulation 3	OG1	6	114,600	40
HT simulation 4	OG2	2	101,000	40
HT simulation 5	OG2	4	114,600	20
HT simulation 6	OG2	6	85,500	30
HT simulation 7	OG3	2	114,600	30
HT simulation 8	OG3	4	85,500	40
HT simulation 9	OG3	6	101,000	20

7.3 Heat Transfer Performance Optimization

7.3.1 Nusselt Number Optimization

In this section, the optimal Nu values will be identified for the three oscillator designs across various factors and levels specified in Table 7.2. Based on this analysis, the oscillator design with the highest Nu will be determined. The Nu results, along with their respective S/N ratios for the three design configurations HT0, HT1, and HT2, are compiled in Table 7.3. The Nu values span from a minimum of 105 to a maximum of 205. As depicted in Fig. 7.2, the S/N ratio analysis for Nu demonstrates that the optimal design parameters include OG3, H/D) = 2, Re = 114,600, and L/D = 20. A greater S/N ratio signifies enhanced heat transfer performance. As the heat transfer L9 orthogonal array did not encompass the optimal configuration for the Nu, a supplementary computational analysis, referred to as HT simulation 10, was performed to evaluate the design with optimal settings. The predicted Nu under these optimized conditions was calculated to be 224. However, the CFD analysis for HT simulation 10 produced an actual Nu of 231, leading to a discrepancy of 3.1% between the predicted and simulated results. This optimal Nu value was derived from the oscillator design HT2, which was obtained through the optimization of oscillation frequency. The influence of different design parameters on the Nu was evaluated through ANOVA, as presented in Table 7.4. The results indicate that the L/D plays the most dominant role in determining Nu, accounting for 44.71% of the contribution, with a p-value of 0.033, which is statistically significant at the 5% level. Furthermore, the model exhibits high reliability, as evidenced by an R-squared value of 98.48%.

TABLE 7.3: Nu results obtained by numerical study and Taguchi method for heat transfer analysis

HT simulation run	**Nu HT0**	**Nu HT1**	**Nu HT2**	**S/N ratio**
HT simulation 1	172	176	179	33.04
HT simulation 2	137	150	167	32.77
HT simulation 3	109	123	132	32.38
HT simulation 4	148	154	160	32.82
HT simulation 5	191	204	214	33.28
HT simulation 6	105	118	128	32.31
HT simulation 7	187	198	205	33.23
HT simulation 8	110	114	124	32.31
HT simulation 9	165	167	173	32.97

TABLE 7.4: Analysis of variance for Nu HT2

Source	**DF**	**Seq SS**	**Contr. (%)**	**Adj SS**	**Adj MS**	**F**	**P**
Jet-to-target (H/D)	2	2114.0	25.08	2114.0	1057.00	16.52	0.057
Reynolds number	2	2418.0	28.69	2418.0	1209.00	18.89	0.050
Target length (L/D)	2	3768.0	44.71	3768.0	1884.00	29.44	0.033
Error	2	128.0	1.52	128.0	64.00		
Total	8	8428.0	100.00				
$R^2 = 98.48\%$							

7.3.1.1 Relationship Between Oscillation Frequency and Nusselt Number Trends

As illustrated in Fig. 7.3, the cyclic oscillation frequency (f) of the HT2 oscillator design shows a consistent increase across all L9 array simulations when compared to the HT1 and HT0 oscillator designs. The cyclic oscillation frequency and the

FIGURE 7.2: Graphical representation of Taguchi analysis main effects plot for S/N ratios of Nu results

oscillation frequency (F) derived from FFT exhibit distinct characteristics due to the underlying physical phenomena they represent.

The cyclic oscillation frequency corresponds to the time taken for the jet to complete one full side-to-side oscillation cycle, similar to a pendulum completing a full swing. In contrast, the oscillation frequency obtained from FFT captures not only the primary oscillation but also the flapping of the jet around its longitudinal axis. Since the data point used for FFT analysis records this local fluctuation, it detects the additional motion caused by flapping.

In ribbed oscillator configurations, the presence of ribs induces additional flow disturbances, causing the jet to exhibit a flapping behavior. This flapping motion effectively doubles the frequency component observed in the FFT analysis.

As a result, the oscillation frequency measured via FFT is approximately twice the cyclic oscillation frequency. This difference arises because the FFT-based frequency accounts for both the primary oscillation and the superimposed flapping dynamics,

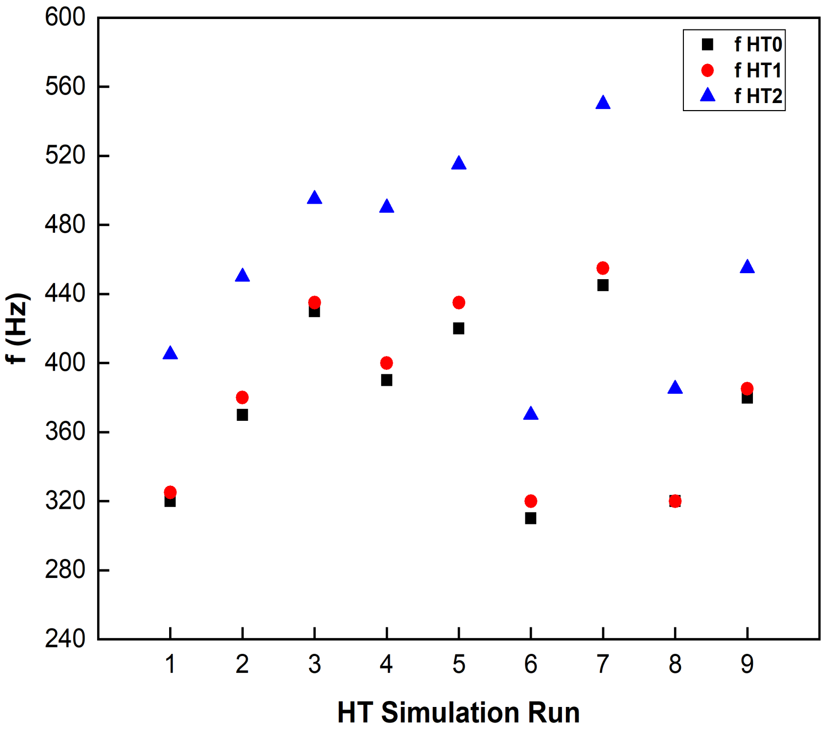

(a)

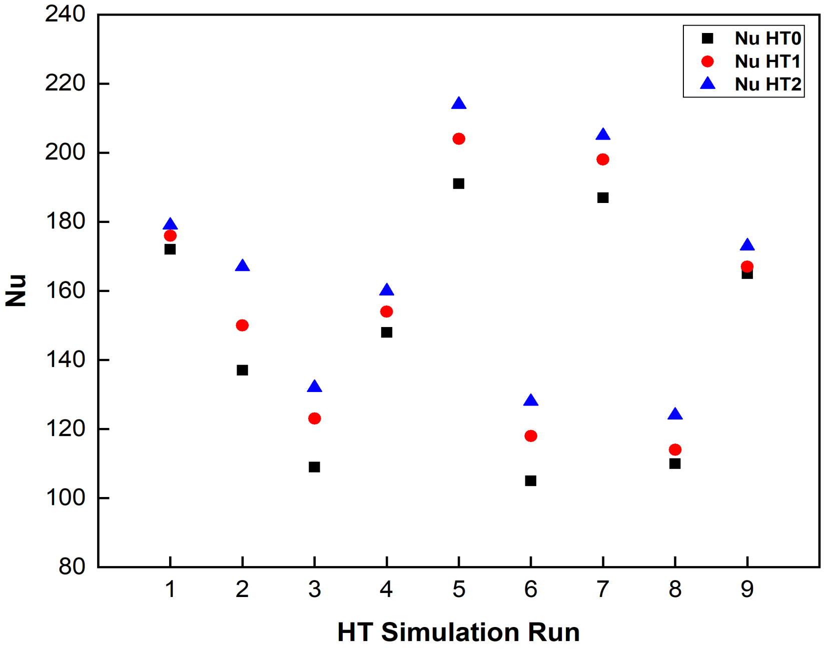

(b)

FIGURE 7.3: (a) Frequency and (b) Nu results; for all three heat transfer designs at all HT simulation runs

whereas the cyclic oscillation frequency solely reflects the fundamental oscillation cycle of the jet. This increasing trend of cyclic oscillation frequency, as shown in Fig. 7.3 (a), is particularly significant, as it highlights the effectiveness of the HT2 design in achieving higher frequencies. The HT1 oscillator design, while showing improvements over the baseline HT0 design, does not reach the same level of frequency as the HT2 design. The observed increase in frequency for the HT2 design is closely correlated with its enhanced heat transfer performance, as evidenced by the corresponding Nu results shown in Fig. 7.3 (b).

Specifically, the HT2 design, which exhibits the highest frequency, also achieves the highest Nu values across all test conditions. This relationship between frequency and Nu is consistent, indicating that higher frequencies contribute to a more effective heat transfer rate. The HT1 design, with its intermediate frequency, also shows elevated Nu values compared to the HT0 design but falls short of the performance achieved by the HT2 design. The HT0 design, with the lowest frequency, consistently exhibits the lowest Nu values. The influence of frequency on heat transfer enhancement can be attributed to several underlying mechanisms. Higher frequencies promote increased fluid mixing and turbulence, which in turn enhance the convective heat transfer process. These factors collectively contribute to the elevated Nu values observed in the HT2 design.

7.3.2 Performance Enhancement Criteria Optimization

Following the identification of the HT2 configuration as the design with the highest Nu value, an in-depth evaluation was conducted to quantify and optimize the performance enhancement criteria (PEC) values for the novel ribbed designs in contrast to the baseline smooth oscillator. PEC is obtained through the following Eq. (7.1):

$$\mathrm{PEC} = \frac{\mathrm{Nu}_e/\mathrm{Nu}_s}{(\Delta P_e/\Delta P_s)^{1/3}} \tag{7.1}$$

Here Nu_e is the Nusselt number of the new ribbed oscillator while Nu_s is the Nusselt number of the smooth oscillator. ΔP_e and ΔP_s are the pressure drops across the domain for the new ribbed oscillator and smooth oscillator, respectively. The $\mathrm{PEC}_{\mathrm{HT1}}$ and $\mathrm{PEC}_{\mathrm{HT2}}$ are calculated in comparison with the smooth oscillator which has a $\mathrm{PEC}_{\mathrm{HT0}} = 1$. A value of $\mathrm{PEC} > 1$ indicates an overall enhancement in performance relative to the smooth baseline configuration, whereas a value of $\mathrm{PEC} < 1$ signifies a reduction in performance.

The PEC values, derived from computational simulations, along with their associated S/N ratios for oscillator configurations HT1 and HT2, are presented in Table 7.5. The calculated PEC values vary from 1.011 to 1.229. Fig. 7.4 depicts the S/N ratio analysis for PEC, revealing that the optimal design parameters for both oscillator designs HT1 and HT2 are OG1, H/D = 6, Re = 114,600, and L/D = 30. In this context, a higher S/N ratio corresponds to an enhanced PEC. As the L9 orthogonal array did not include the optimal parameter combination for maximizing PEC, an additional computational investigation, referred to as HT simulation 11, was performed to evaluate performance under ideal conditions. The predicted PEC value under these optimized settings was calculated as 1.258. However, the actual PEC derived from CFD-based analysis for HT simulation 11 was 1.252, resulting in a 2.3% discrepancy between the predicted and simulated outcomes.

Table 7.5: PEC results and corresponding S/N ratios obtained by Taguchi method for heat transfer analysis

HT simulation run	**PEC HT1**	**S/N ratio**	**PEC HT2**	**S/N ratio**
HT simulation 1	1.025	0.212	1.049	0.416
HT simulation 2	1.097	0.805	1.229	1.792
HT simulation 3	1.131	1.066	1.221	1.730
HT simulation 4	1.042	0.361	1.091	0.760
HT simulation 5	1.070	0.588	1.128	1.048
HT simulation 6	1.122	0.999	1.224	1.758
HT simulation 7	1.060	0.509	1.107	0.879
HT simulation 8	1.038	0.325	1.136	1.108
HT simulation 9	1.011	0.099	1.056	0.473

The highest PEC value was attained with the HT2 oscillator design, which was identified as the most efficient configuration through frequency-based optimization.

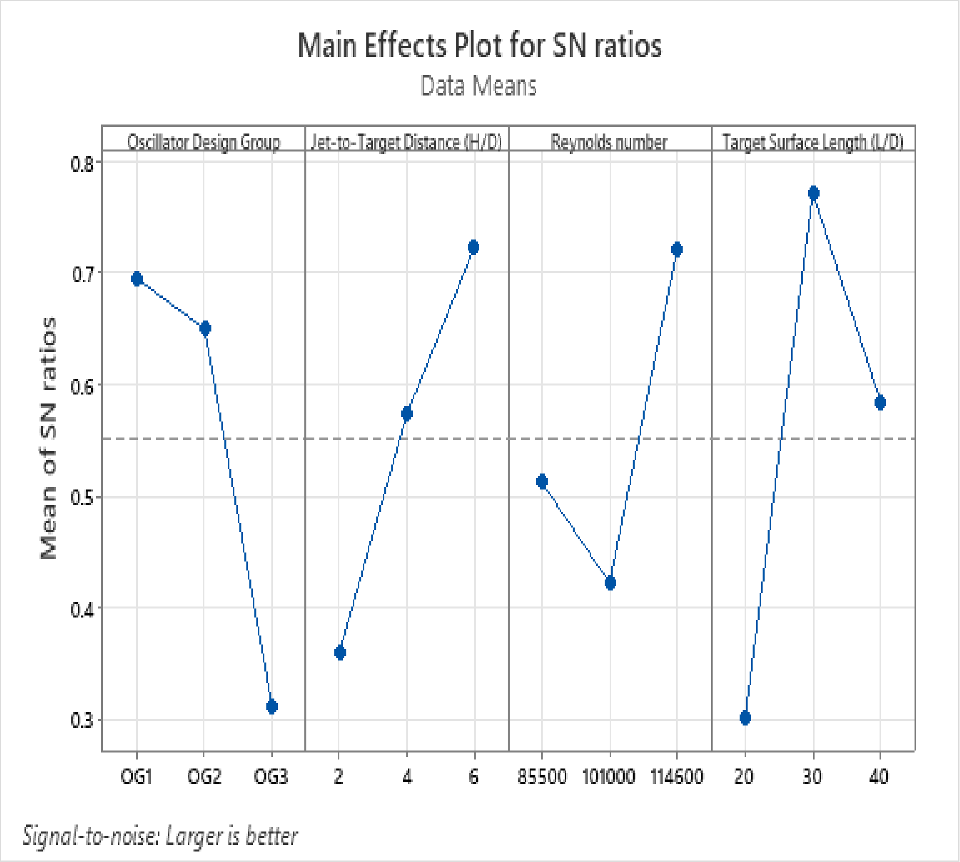

(a)

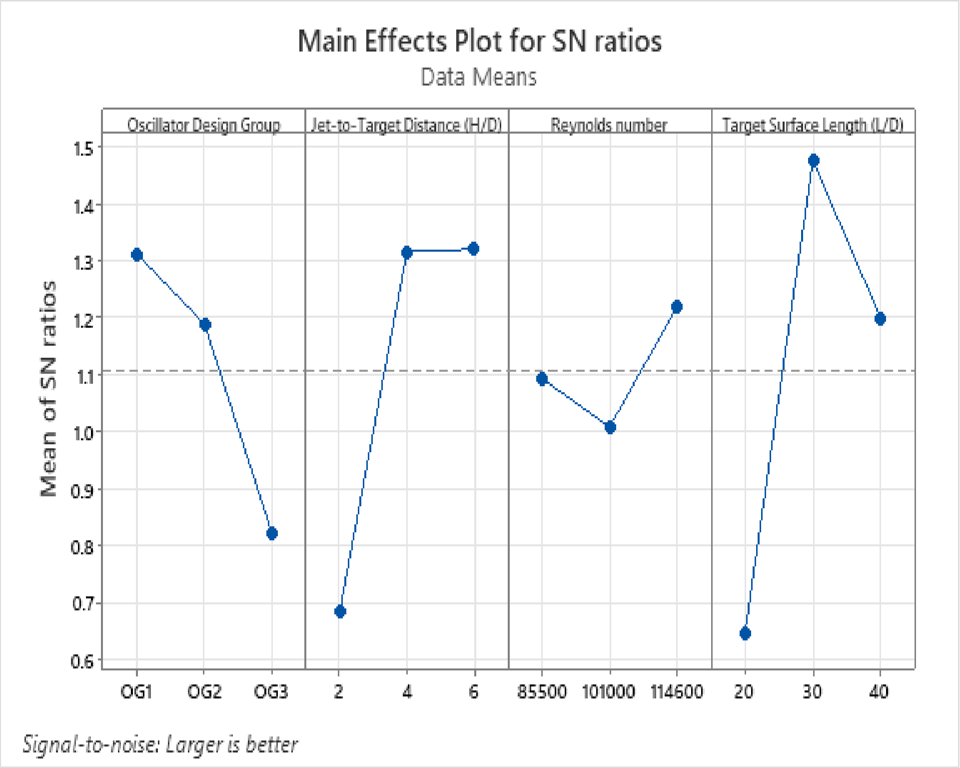

(b)

FIGURE 7.4: Graphical representation of Taguchi analysis main effects plot for S/N ratios of (a) PEC HT1 (b) PEC HT2, results

Under the same optimum setting, the PEC value of the HT1 oscillator design was computed to be 1.156. The corresponding Nu at these optimum conditions were found to be 136 for HT0, 157 for HT1, and 169 for HT2. An increase of 15.4% in Nu for HT1 and an increase of 24.3% for HT2 were obtained as compared to the smooth oscillator. The influence of various design parameters on PEC was further examined using ANOVA. The analysis indicates that the L/D is the most significant factor, accounting for 45.43% of the variation in PEC.

As previously discussed, the HT2 oscillator design, which focuses on optimizing the oscillation frequency, demonstrated the most significant enhancement in the performance of the oscillator system under investigation. This design achieved a PEC value of 1.252, indicating superior thermal and hydraulic performance.

In comparison, the HT1 oscillator design, optimized for the jet deflection angle, attained a PEC value of 1.156. Although it was lower than that of the HT2 design, it still surpassed the performance of the baseline smooth oscillator design. These results highlight the effectiveness of targeted design optimizations in improving oscillator performance.

Fig. 7.5 presents a comprehensive comparison of the frequency and Nu results for all three oscillator designs under optimum conditions. The results indicate that the HT2 oscillator design achieves the highest frequency and Nu values, reflecting its enhanced thermal and flow dynamic performance. Notably, a consistent and similar trend is observed between the frequency and Nu values across all three designs, suggesting a strong correlation between these parameters.

The HT2 oscillator operates at a frequency of 505 Hz, which is 18.8% higher than the frequency of the baseline HT0 smooth oscillator (425 Hz). This increase in frequency is accompanied by a 24.3% improvement in the Nu value, with the ribbed optimized HT2 oscillator design achieving a Nu of 169 compared to the baseline HT0 smooth oscillator's Nu of 136.

Similarly, the HT1 oscillator design, which focuses on optimizing the jet deflection angle, exhibits a frequency of 450 Hz, representing a 5.9% increase over the HT0 oscillator. Additionally, the Nu value for the HT1 design rises to 157, marking a 15.4% improvement compared to the HT0 oscillator. While the performance gains of the HT1 design are more modest than those of the HT2 design, they still demonstrate the benefits of optimizing geometric and flow parameters in oscillator systems.

7.3.2.1 Robustness Assessment of Optimized Designs Under Varying Re Conditions

The robustness of the optimized oscillator designs was evaluated across three different Reynolds numbers (Re = 85,500, 101,000, and 114,600). Fig. 7.6 demonstrates that both optimized designs maintain consistent performance advantages: the HT2 design delivers $> 21\%$ higher Nu values than HT0 across all tested Re conditions, while HT1 shows a $> 12\%$ improvement. Frequency performance follows similar trends, with HT2 maintaining $> 18\%$ higher frequencies versus HT0 and HT1 showing $> 1.5\%$ increases. Both optimized designs exhibit stable oscillation characteristics and predictable, near-linear scaling with Reynolds number. These results confirm reliable operation under flow variations, substantiating the designs' practical viability for applications like turbine blade cooling where operating conditions frequently deviate from nominal points. The consistent performance improvements across all tested Re values highlight the robustness of both optimization approaches.

7.3.3 Flow Dynamics Assessment for Oscillator Designs Performance Comparison

The performance of the three oscillator designs, HT0, HT1, and HT2 can be effectively analyzed through velocity contour plots shown in Fig. 7.7 and the variation of the Nu for L/D (target surface length normalized by the radial distance from the stagnation point). The velocity contour plots present distinct flow patterns for each oscillator design, particularly in terms of jet attachment to the target surface.

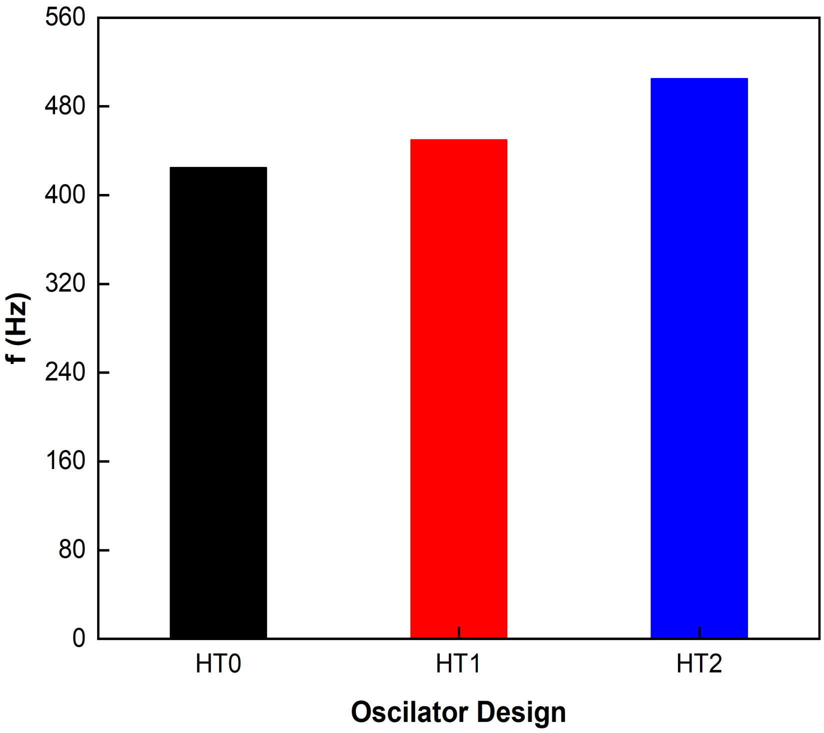

(a)

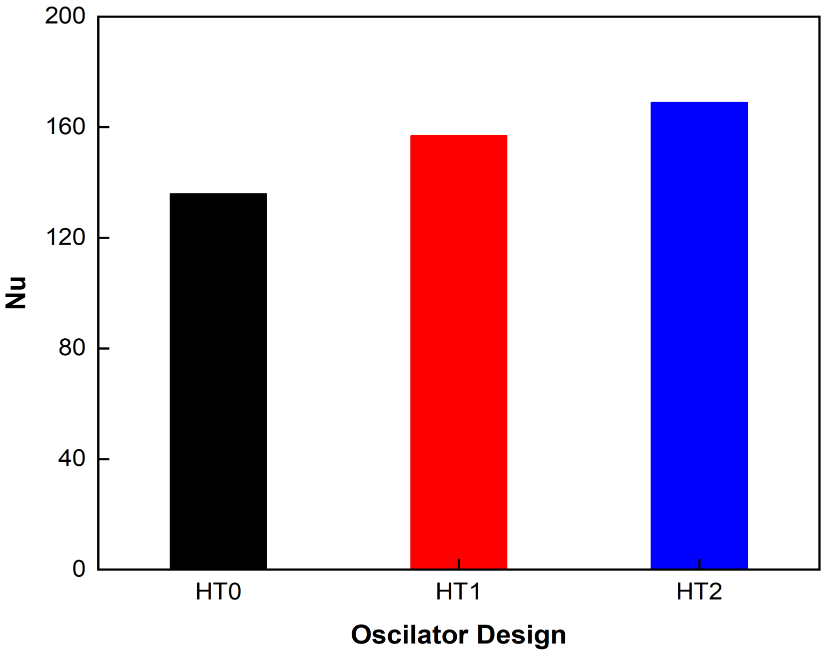

(b)

FIGURE 7.5: (a) Frequency and (b) Nu results; obtained for all three oscillator designs under optimum conditions

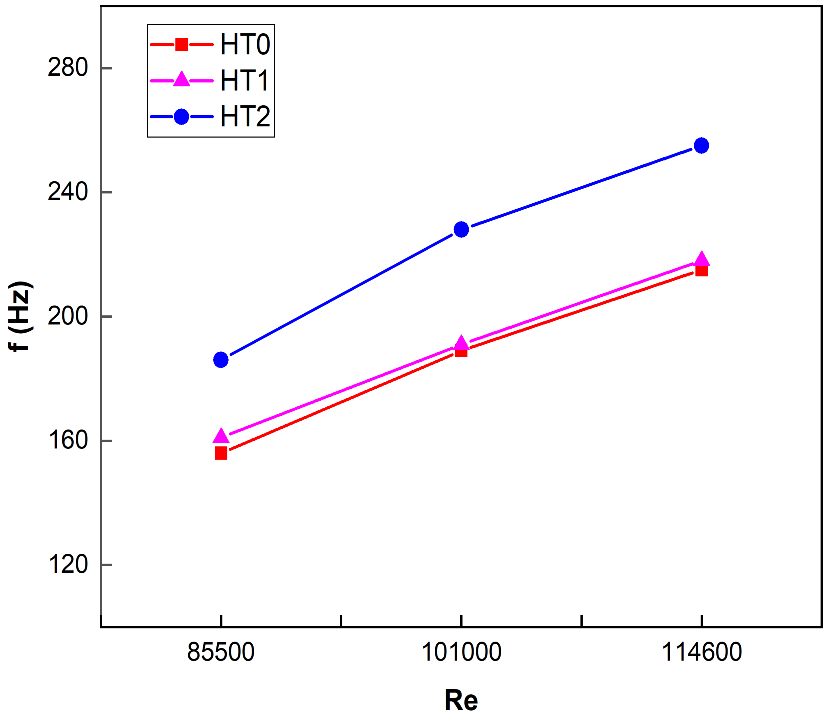

(a)

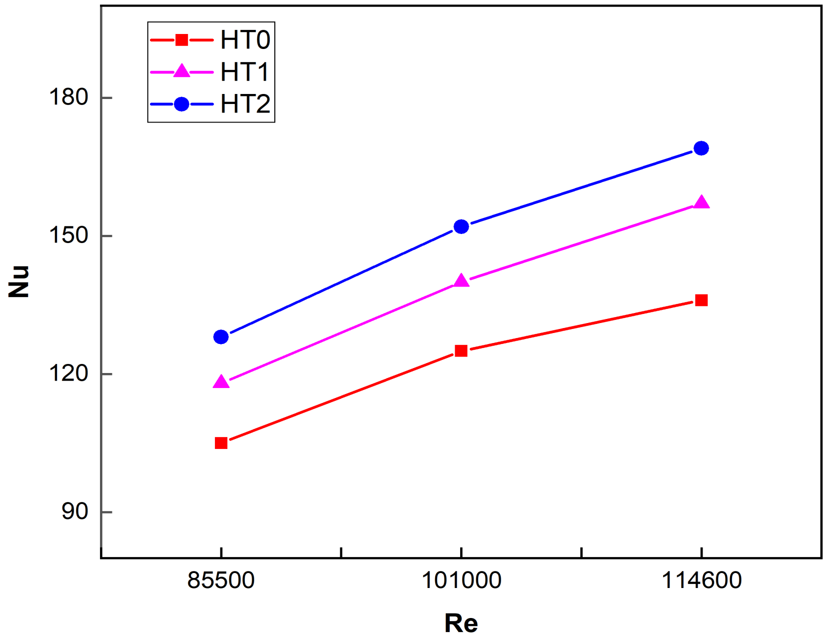

(b)

FIGURE 7.6: (a) Frequency and (b) Nu results; obtained for all three oscillator designs at three different Re conditions

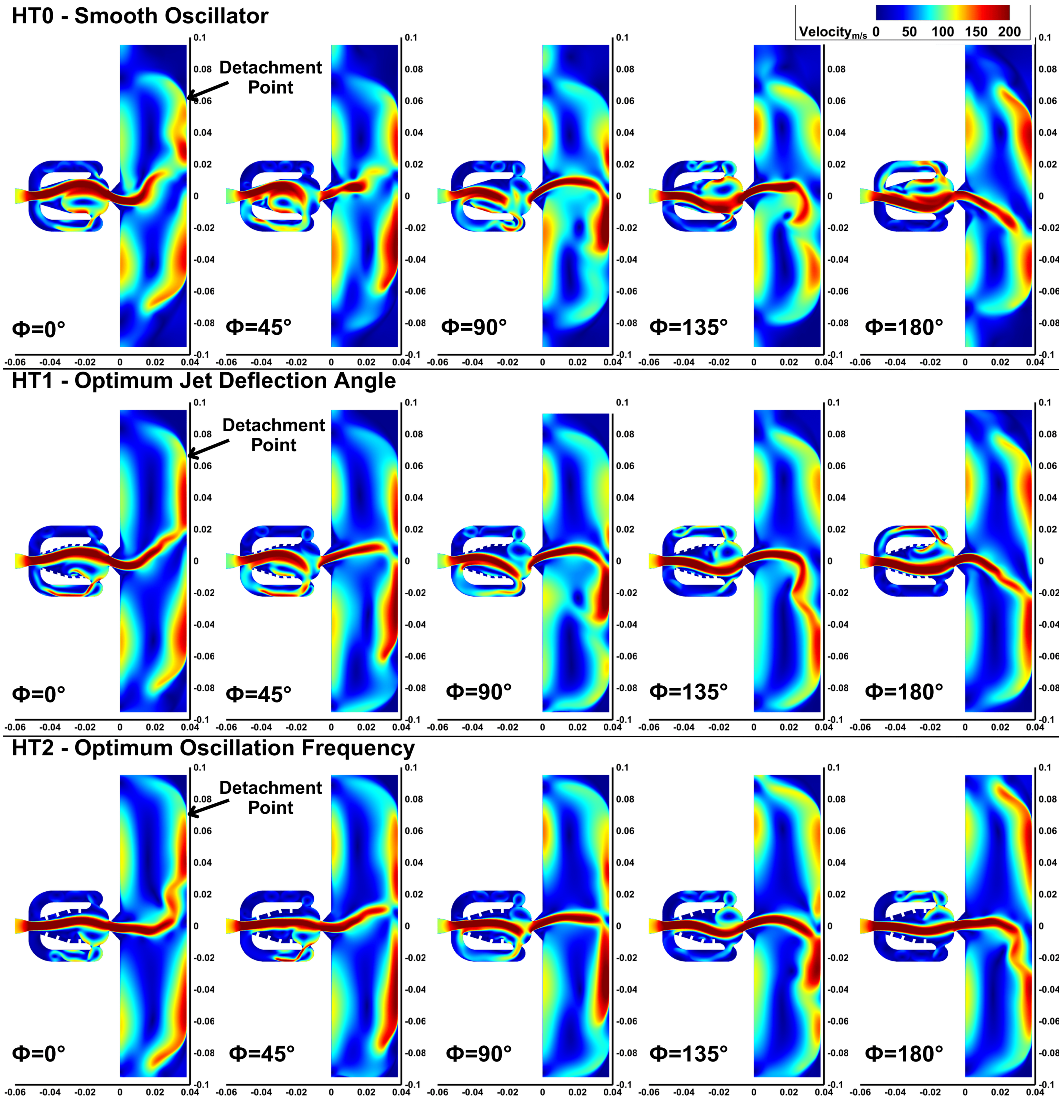

FIGURE 7.7: Velocity contour plots for jet impingement of all three oscillator designs under optimum conditions at different phase angles

The HT2 oscillator design demonstrates the most favorable flow characteristics, with the jet remaining attached to the target surface over a significantly longer length compared to the other designs.

This extended attachment length enhances the convective heat transfer process, as the cooling effect of the jet is sustained over a larger area of the target surface.

The HT1 oscillator design also shows improved jet attachment relative to the baseline HT0 design, though the attachment length is shorter than that of the HT2 design. In contrast, the HT0 design exhibits the earliest jet detachment, resulting in a reduced cooling effect and lower overall thermal performance.

Fig. 7.8 illustrates the underlying mechanisms responsible for the early jet detachment observed in the HT0 design and the delayed jet detachment from the heated surface in the HT2 design during jet impingement cooling. The momentum contour plots reveal distinct behavioral patterns in the jet dynamics across the three designs. In the HT0 configuration, the jet undergoes detachment at a phase angle of $\Phi = 45°$, remaining detached until $\Phi = 112.5°$, and subsequently partially reattaching at $\Phi = 135°$. A similar initial detachment is observed in the HT1 design at $\Phi = 45°$; however, partial reattachment occurs earlier at $\Phi = 112.5°$ and complete reattachment at $\Phi = 135°$, indicating a marginally improved behavior compared to HT0. In contrast, the HT2 design demonstrates a delayed jet breaking, with the break occurring at $\Phi = 90°$, followed by complete reattachment at $\Phi = 135°$. The analysis further highlights the spatial characteristics of the jet detachment. In the HT0 design, a significant gap is evident between the separated jet streams, which persists over a prolonged duration. This gap is comparatively smaller in the HT1 design, while in the HT2 configuration, the gap is minimal, facilitating a more rapid reattachment of the jet. The reduced gap and accelerated reattachment in the HT2 design enable the jet to maintain its structural integrity for an extended period. As a result, when the jet impinges on the target surface, detachment is delayed, allowing the jet to cover a larger surface area. This expanded area of jet impingement enhances the cooling coverage, leading to more efficient heat extraction from the hot surface. Consequently, the HT2 design exhibits superior heat transfer performance due to its ability to sustain jet stability and maximize the cooling surface area, thereby achieving higher thermal performance.

The variation of the Nu with L/D shown in Fig. 7.9 further corroborates the observations from the velocity and momentum contour plots. The HT2 oscillator design exhibits the highest Nu values across the target surface, indicating superior heat transfer performance. The Nu values for HT2 remain elevated up to approximately 13D, after which the curve begins to flatten.

This delayed flattening is consistent with the extended jet attachment observed in the velocity and momentum contours, as the sustained attachment allows for efficient heat transfer over a longer surface length. The HT1 oscillator design, while

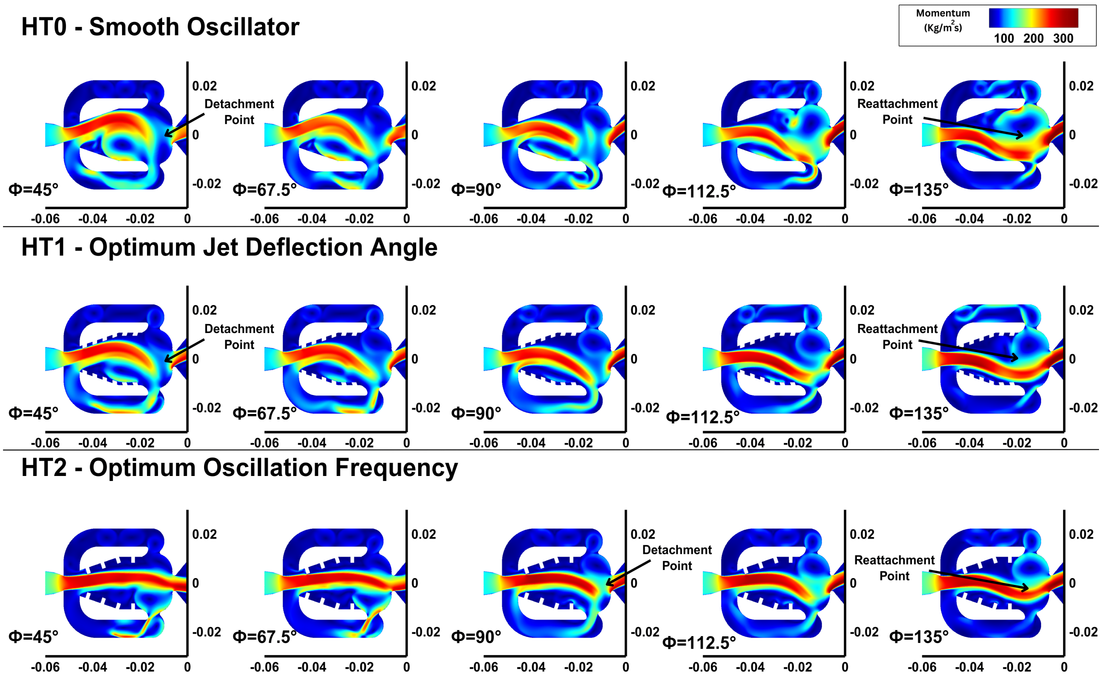

FIGURE 7.8: Momentum contour plots for all three oscillator designs under optimum conditions at different phase angles

outperforming the HT0 design, shows a slightly earlier flattening of the Nu curve at around 12D.

This corresponds to its intermediate jet attachment length, which is longer than that of HT0 but shorter than HT2. The HT0 design, on the other hand, exhibits the lowest Nu values and the earliest flattening of the curve at approximately 11D. This early flattening is indicative of premature jet detachment, which limits the cooling effectiveness and results in lower thermal performance.

The results highlight the critical role of jet attachment length in determining the heat transfer performance of oscillator designs. The HT2 design, with its optimized frequency, maximizes jet attachment and cooling performance, making it the most effective among the three designs. The HT1 design, optimized for jet deflection angle, also demonstrates significant improvements over the baseline HT0 design but falls short of the performance achieved by HT2. These findings show the importance of design optimization in enhancing the thermal and hydrodynamic performance of oscillator systems.

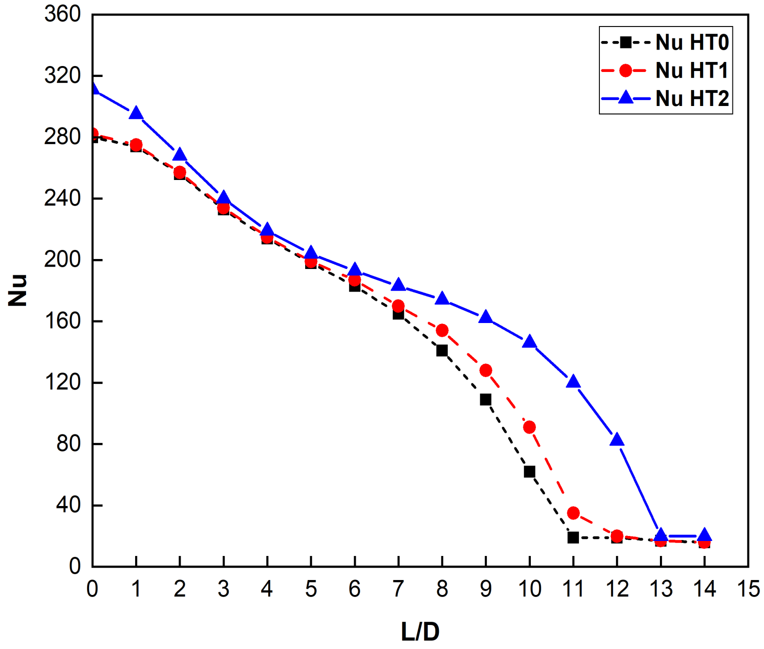

Figure 7.9: Nu results plotted at different L/D for all three oscillator designs under optimum conditions

The results demonstrate that ribbed Coanda surfaces offer better performance characteristics with direct relevance to engineering applications. For thermal management systems (e.g., turbine blade cooling), the ribbed geometry enhances heat transfer through two effects: (1) intensified cooling from improved jet impingement dynamics and (2) system wide efficiency gains via turbulent mixing. The 24.3% Nu enhancement achieved in present study demonstrates practical significance for turbine blade cooling applications, where such improvements can reduce cooling flow requirements, while improving temperature uniformity. These gains directly translate to extended component lifetimes and increased engine efficiency. In aerodynamic flow control, the ribbed design enables application-specific optimization, favoring high-frequency oscillations for separation control or strong jet deflection for flap attachment. The quantified performance enhancements establish that ribbed geometries provide a viable design approach for meeting the competing demands of thermal efficiency and flow control in practical engineering systems, particularly in turbomachinery and aerodynamic applications.

7.4 Conclusion

This study optimizes the hydrodynamic and thermal performance of a double-feedback fluidic oscillator by redesigning the Coanda surface geometry. Using the Taguchi method, we analyzed key design factors, including: Ribbed optimized oscillator designs, Reynolds number (85,400, 101,000, 114,600), jet-to-target distance (2, 4, 6), and target surface length (20, 30, 40) were systematically analyzed to achieve significant improvements.

Computational simulations employed the SST k-ω turbulence model, which effectively captures complex flow behaviors like separation and reattachment. Grid independence and model validation ensured reliable results. The initial analysis of the study exhibited the following key features:

i. In the thermal performance the optimal Nu values were identified for the three oscillator designs (HT0, HT1, HT2) across various factors and levels.

ii. Optimal design parameters achieved were design HT2, H/D = 2, Re = 114,600, and L/D = 20, achieving a peak Nu of 224.

iii. The key influence was by L/D having the strongest impact (44.71% contribution per ANOVA), with the HT2 design optimized for oscillation frequency.

iv. Primary separation bubble size in the mixing chamber directly controlled oscillation frequency, and the higher the oscillation frequency, the higher the Nu was observed.

Following the identification of the HT2 configuration as the most efficient in improving heat transfer performance, an in-depth evaluation was conducted to quantify and optimize the PEC values for the innovative ribbed designs in contrast to the baseline smooth oscillator.

i. The optimized design improved thermal performance, increasing the Nu by 24.3% with a PEC of 1.252. Key parameters were H/D = 6, Re = 114,600 and L/D = 30.

ii. This boost was mainly due to longer jet attachment on the hot surface, enhancing heat transfer.

iii. The ribbed Coanda surface also helped by improving flow mixing and energy distribution.

These findings highlight the effectiveness of the Taguchi optimization approach in refining fluidic oscillator performance and emphasize the critical role of higher oscillation frequencies, optimized flow dynamics, and geometric modifications in achieving superior thermal performance. This research provides valuable insights for advancing fluidic oscillator designs in applications requiring enhanced heat transfer and flow control, such as turbine blade cooling, electronic component cooling, energy-efficient heat exchangers, and other industrial fluidic systems. The findings pave the way for future studies involving experimental validation and exploration of advanced geometric variations such as dimpled or curved rib configurations to further optimize jet dynamics and improve the overall performance of fluidic oscillators in practical engineering applications. The outcomes of this work pave the way for further exploration of advanced geometric configurations and operating conditions to maximize the performance of fluidic oscillators in practical engineering applications.

Chapter 8

Conclusion and Future Work

This chapter summarizes the main findings of the present research in the form of key conclusions. It highlights the significant research contributions derived from the numerical and optimization studies.

Furthermore, it outlines future research directions aimed at extending and enhancing the current work.

8.1 Conclusion

This research has systematically investigated the design and optimization of fluidic oscillators with ribbed Coanda surfaces through an integrated computational and statistical approach.

Using advanced numerical simulations, the study evaluated the effects of key geometric parameters on oscillator performance.

This evaluation was conducted by combining the Taguchi design of experiments with Grey Relational Analysis.

The major findings reveal that rib modifications significantly enhance both hydrodynamic and thermal characteristics.

8.1.1 Hydrodynamic Performance

The rib aspect ratio (0.64–1.56) strongly influences jet oscillation by modifying the recirculation bubble in the mixing chamber. Higher aspect ratio ribs reduce the bubble size, lower flow resistance, and enable faster jet switching between walls, resulting in improved overall performance. For instance, the highest aspect ratio case ($\mathrm{AR}_{\mathrm{ribs}} = 1.56$) shows a 131% increase in oscillation frequency compared to the smooth configuration. In addition, higher aspect ratios enhance overall efficiency, as reflected by the FDPR, while slightly restricting jet deflection due to stronger flow confinement. Similarly, the number of ribs (1–6) affects the separation bubble dynamics and oscillator performance. Fewer ribs produce smaller bubbles and higher frequencies, but an intermediate configuration (four ribs) provides the best balance between frequency, jet deflection, and pressure drop. As an example, four ribs achieve a 146% increase in frequency while maintaining a reasonable deflection angle, and the FDPR is also significantly higher than for other configurations. This highlights that both rib aspect ratio and number of ribs can be optimized to enhance jet oscillation efficiency while controlling energy losses.

8.1.2 Multi-objective Optimization Insight

Through multi-objective optimization, the research identified that rib count has the dominant effect (65.01% contribution) on oscillation frequency, while rib angle most influences jet deflection (76.86% contribution) and aspect ratio primarily affects pressure drop reduction (65.93% contribution). The optimized oscillator design achieved simultaneous improvements of 19.9% in frequency, 39.7% in jet deflection angle, and 17.6% reduction in pressure drop.

8.1.3 Thermal Performance

When applied to impinging jet cooling, the ribbed oscillator (HT2) outperformed the smooth design by 24.3% in Nu and achieved a PEC of 1.252 at Re=114,600, H/D=6, and L/D=30. This improvement stems from:

i. Extended jet attachment on the target surface, promoting sustained heat transfer.
ii. Improved flow mixing due to rib-induced vortices, which disrupt thermal boundary layers.
iii. Reduced pressure losses, allowing higher flow rates without compromising efficiency.
iv. ANOVA identified L/D (44.71% contribution) as the most critical factor, as shorter target surfaces concentrate impingement cooling.

8.2 Key Research Contributions

The key contributions of this work encompass significant advancements in fluidic oscillator design and optimization for enhanced sweeping jet impingement cooling applications.

i. First, we present a comprehensive review and critical analysis of double-feedback fluidic oscillators, establishing clear relationships between key design parameters (feedback channels, mixing chamber geometry, Coanda surface profiles, and nozzle configurations) and their impacts on flow control and thermal performance characteristics.

   Building on this foundation, we introduce an innovative ribbed Coanda surface design that demonstrates remarkable performance improvements.

ii. Our second major contribution involves the development of a novel multi-objective optimization framework that integrates CFD with Taguchi methods and Grey Relational Analysis.

   This robust approach systematically evaluates and optimizes three critical rib parameters: aspect ratio, number of ribs and angle of ribs. The framework successfully identifies optimal configurations that simultaneously maximize oscillation performance while minimizing pressure losses, providing a valuable tool for engineering design processes.

iii. The third significant contribution applies these optimized oscillator designs to practical jet impingement cooling systems. Through rigorous parametric studies employing Taguchi methods, we determine the optimal combination of operational parameters including jet-to-surface spacing, Reynolds number, and target surface length.

This systematic approach yields superior heat transfer performance, with demonstrated improvements in cooling efficiency particularly relevant for high-temperature applications such as electronics cooling and gas turbine blade thermal management.

Collectively, these contributions advance both the scientific understanding of ribbed oscillator dynamics and their practical implementation in industrial cooling applications, while providing a replicable methodology for future research in active flow control devices.

8.3 Future Research Direction

Based on these findings, several avenues for future research are proposed. Since the current study predicts significant performance improvements due to rib configurations, future work should extend these findings through experimental validation to confirm the numerical predictions and capture any overlooked effects. Experimental studies are important because they provide a direct measurement of the actual flow behavior and thermal performance, allowing verification of numerical predictions and identification of effects that may be overlooked in simulations.

Potential experimental setups could include flow visualization techniques, high-speed imaging, or particle image velocimetry (PIV) to capture jet oscillation behavior and measure deflection angles, frequency, and pressure variations, thereby providing a comprehensive understanding of the fluid dynamics in ribbed oscillators.

Given that 2D simulations cannot fully capture complex flow phenomena such as secondary vortices and spanwise jet flapping, future studies should employ 3D CFD simulations to better understand their influence on hydrodynamic and thermal performance. These simulations can provide deeper insights into how three-dimensional flow effects influence both hydrodynamic performance and heat transfer efficiency, enabling more accurate predictions and better-informed design decisions. Incorporating both experimental validation and 3D simulations will strengthen the reliability of the findings and guide the development of more effective fluidic oscillator designs for practical applications. Investigating alternative rib geometries, such as curved or tapered ribs, could further optimize performance. Studies may focus on quantifying the impact of rib shape, spacing, and orientation on flow behavior and frequency-deflection-pressure metrics. Considering the potential applications in turbine blade and electronics cooling, future research should investigate multiphase flows to evaluate performance under different heat transfer conditions. Extending the work to multiphase flows would broaden the applicability to scenarios involving condensation or boiling heat transfer, which is particularly relevant for advanced turbine blade cooling and electronics cooling applications.

Another promising direction is the integration of machine learning algorithms with CFD simulations to enhance the prediction of optimal rib configurations and operating conditions. Approaches such as surrogate modeling or neural networks can accelerate the design process by enabling rapid exploration of a wide parameter space while reducing computational cost. Specific research questions could focus on identifying configurations that maximize performance under varying flow and thermal conditions.

Collectively, these future directions build on the present findings and contribute to advancing active flow control strategies and energy-efficient thermal management in engineering applications such as electronics cooling, aerospace, and power generation systems.

Bibliography

[1] F. Grubišić-Čabo, S. Nižetić, I. M. Kragić, and D. Čoko, "Further progress in the research of fin-based passive cooling technique for the free-standing silicon photovoltaic panels," *International Journal of Energy Research*, vol. 43, pp. 3475–3495, 2019.

[2] Y. Xu, B. Sun, Y. Ling, Q. Fei, Z. Chen, X. Li, P. Guo, N. Jeon, S. Goswami, Y. Liao, S. Ding, Q. Yu, J. Lin, G. Huang, and Z. Yan, "Multiscale porous elastomer substrates for multifunctional on-skin electronics with passive-cooling capabilities," *Proceedings of the National Academy of Sciences of the United States of America*, vol. 117, pp. 205–213, 2020.

[3] Y. Zhou, S. Zheng, and G. Zhang, "Study on the energy performance enhancement of a new pcms integrated hybrid system with the active cooling and hybrid ventilations," *Energy*, vol. 179, pp. 111–128, 2019.

[4] W. Hackenhaar, J. A. Mazzaferro, F. Montevecchi, and G. Campatelli, "An experimental-numerical study of active cooling in wire arc additive manufacturing," *Journal of Manufacturing Processes*, vol. 52, pp. 58–65, 2020.

[5] H. M. Maghrabie, M. Attalla, H. E. Fawaz, and M. Khalil, "Impingement/effusion cooling of electronic components with cross-flow," *Applied Thermal Engineering*, vol. 151, pp. 199–213, 2019.

[6] S. Wiriyasart and P. Naphon, "Heat spreading of liquid jet impingement cooling of cold plate heat sink with different fin shapes," *Case Studies in Thermal Engineering*, vol. 20, p. 100638, 2020.

[7] A. R. Ali and I. Janajreh, "Numerical simulation of turbine blade cooling via jet impingement," *Energy Procedia*, vol. 75, pp. 3220–3229, 2015.

[8] H. Fawzy, Q. Zheng, Y. Jiang, A. Lin, and N. Ahmad, "Conjugate heat transfer of impingement cooling using conical nozzles with different schemes in a film-cooled blade leading-edge," *Applied Thermal Engineering*, vol. 177, 2020.

[9] M. M. Matheswaran, T. V. Arjunan, and D. Somasundaram, "Analytical investigation of solar air heater with jet impingement using energy and exergy analysis," *Solar Energy*, vol. 161, pp. 25–37, 2018.

[10] M. Awad, A. Radwan, O. Abdelrehim, M. Emam, A. N. Shmroukh, and M. Ahmed, "Performance evaluation of concentrator photovoltaic systems integrated with a new jet impingement-microchannel heat sink and heat spreader," *Solar Energy*, vol. 199, pp. 852–863, 2020.

[11] T. Huang, L. Yue, and X. Chang, "Numerical study of a fully confined supersonic slot impinging jet from bleed system," *Aerospace Science and Technology*, vol. 90, pp. 12–22, 2019.

[12] H. D. Lim, T. H. New, R. Mariani, and Y. D. Cui, "Effects of bevelled nozzles on standoff shocks in supersonic impinging jets," *Aerospace Science and Technology*, vol. 94, 2019.

[13] M. Wae-hayee, K. Yeranee, W. Suksuwan, A. Alimalbari, S. Sae-ung, and C. Nuntadusit, "Heat transfer enhancement in rotary drum dryer by incorporating jet impingement to accelerate drying rate," *Drying Technology*, pp. 1–11, 2020.

[14] B. Turkan, A. B. Etemoglu, and M. Can, "Analysis of evaporative drying of thin ink films using high-velocity hot-air impinging jets: A comprehensive review," *Surface Review and Letters*, vol. 27, pp. 1–21, 2020.

[15] N. M. Alkhudhiri, M. S. Gadala, and M. S. Khan, "Simulation of jet impingement cooling of a stationary hot steel plate," *2020 Advances in Science and Engineering Technology International Conferences, ASET 2020*, 2020.

[16] U. Ansu, S. C. Godi, A. Pattamatta, and C. Balaji, "Experimental investigation of the inlet condition on jet impingement heat transfer using liquid crystal thermography," *Experimental Thermal and Fluid Science*, vol. 80, pp. 363–375, 2017.

[17] C. S. Greco, G. Paolillo, A. Ianiro, G. Cardone, and L. de Luca, "Effects of the stroke length and nozzle-to-plate distance on synthetic jet impingement heat transfer," *International Journal of Heat and Mass Transfer*, vol. 117, pp. 1019–1031, 2018.

[18] A. W. Glaspell, V. J. Rouse, B. K. Friedrich, and K. Choo, "Heat transfer and hydrodynamics of air assisted free water jet impingement at low nozzle-to-surface distances," *International Journal of Heat and Mass Transfer*, vol. 132, pp. 138–142, 2019.

[19] B. Markal, M. Avci, and O. Aydin, "Conical coaxial impinging air jets: angle effect on the heat transfer performance," *Heat and Mass Transfer/Waerme- und Stoffuebertragung*, vol. 56, pp. 3135–3146, 2020.

[20] K. Jambunathan, E. Lai, M. A. Moss, and B. L. Button, "A review of heat transfer data for single circular jet impingement," *International Journal of Heat and Fluid Flow*, vol. 13, pp. 106–115, 1992.

[21] D. H. Wolf, F. P. Incropera, and R. Viskanta, "Jet impingement boiling," *Advances in Heat Transfer*, vol. 23, 1993.

[22] G. Krishan, K. C. Aw, and R. N. Sharma, "Synthetic jet impingement heat transfer enhancement – a review," *Applied Thermal Engineering*, vol. 149, pp. 1305–1323, 2019.

[23] J. Mohammadpour and A. Lee, "Investigation of nanoparticle effects on jet impingement heat transfer: A review," *Journal of Molecular Liquids*, vol. 316, p. 113819, 2020.

[24] L. Hussain, M. M. Khan, M. Masud, F. Ahmed, Z. Rehman, Łukasz Amanowicz, and K. Rajski, "Heat transfer augmentation through different jet impingement techniques: A state-of-the-art review," *Energies*, vol. 14, pp. 1–42, 2021.

[25] S. Dutta and P. Singh, "Opportunities in jet-impingement cooling for gas-turbine engines," *Energies*, vol. 14, pp. 1–29, 2021.

[26] R. Viskanta, "Heat transfer to impinging isothermal gas and flame jets," *Experimental Thermal and Fluid Science*, vol. 6, pp. 111–134, 1993.

[27] H. M. Maghrabie, "Heat transfer intensification of jet impingement using exciting jets - a comprehensive review," *Renewable and Sustainable Energy Reviews*, vol. 139, p. 110684, 2021.

[28] K. Wongcharee, K. Kunnarak, V. Chuwattanakul, and S. Eiamsa-Ard, "Heat transfer rate of swirling impinging jets issuing from a twisted tetra-lobed nozzle," *Case Studies in Thermal Engineering*, vol. 22, p. 100780, 2020.

[29] M. Fénot, E. Dorignac, and R. Lantier, "Heat transfer and flow structure of a hot annular impinging jet," *International Journal of Thermal Sciences*, vol. 170, p. 107091, 2021.

[30] P. Gil, J. Wilk, R. Smusz, and R. Gałek, "Centerline heat transfer coefficient distributions of synthetic jets impingement cooling," *International Journal of Heat and Mass Transfer*, vol. 160, 2020.

[31] C. Tang, J. Z. Zhang, Y. W. Lyu, and X. M. Tan, "Convective heat transfer on a flat target surface impinged by pulsating jet with an additional transmission chamber," *Heat and Mass Transfer/Waerme- und Stoffuebertragung*, vol. 56, pp. 183–205, 2020.

[32] L. Huang, T. Yeom, T. Simon, and T. Cui, "An experimental and numerical study on heat transfer enhancement of a heat sink fin by synthetic jet impingement," *Heat and Mass Transfer/Waerme- und Stoffuebertragung*, vol. 57, pp. 583–593, 2021.

[33] P. Li, X. Huang, and D. Guo, "Numerical analysis of dominant parameters in synthetic impinging jet heat transfer process," *International Journal of Heat and Mass Transfer*, vol. 150, p. 119280, 2020.

[34] Z. Travnicek and Z. Antosova, "Impingement heat transfer to the synthetic jet issuing from a nozzle with an oscillating cross section," *International Journal of Thermal Sciences*, vol. 153, p. 106349, 2020.

[35] Y. wei Lyu, J. zhou Zhang, J. wen Tan, and Y. Shan, "Impingement heat transfer on flat and concave surfaces by piston-driven synthetic jet from planar lobed orifice," *International Journal of Heat and Mass Transfer*, vol. 167, p. 120832, 2021.

[36] R. Talapati, V. Katti, and N. Hiremath, "Local heat transfer characteristics of synthetic air jet impinging on a smooth convex surface," *International Journal of Thermal Sciences*, vol. 170, p. 107143, 2021.

[37] S. Abishek and R. Narayanaswamy, "Low frequency pulsating jet impingement boiling and single phase heat transfer," *International Journal of Heat and Mass Transfer*, vol. 159, p. 120052, 2020.

[38] C. M. Hsu, W. C. Jhan, and Y. Y. Chang, "Flow and heat transfer characteristics of a pulsed jet impinging on a flat plate," *Heat and Mass Transfer/Waerme- und Stoffuebertragung*, vol. 56, pp. 143–160, 2020.

[39] S. Rakhsha, M. R. Zargarabadi, and S. Saedodin, "Experimental and numerical study of flow and heat transfer from a pulsed jet impinging on a pinned surface," *Experimental Heat Transfer*, vol. 34, pp. 376–391, 2021.

[40] J. M. Simmons and J. C. S. Laif, "Jet excitation by an oscillating vane," *AIAA Journal*, vol. 19, pp. 673–676, 1981.

[41] L. Tianshu and J. P. Sullivan, "Heat transfer and flow structures in an excited circular impinging jet," *International Journal of Heat and Mass Transfer*, vol. 39, pp. 3695–3706, 1996.

[42] B. Markal, “The effect of total flowrate on the cooling performance of swirling coaxial impinging jets,” *Heat and Mass Transfer/Waerme- und Stoffuebertragung*, vol. 55, pp. 3275–3288, 2019.

[43] P. Singh and S. Chander, “Heat transfer and fluid flow characteristics of a pair of interacting dual swirling flame jets impinging on a flat surface,” *International Journal of Heat and Mass Transfer*, vol. 124, pp. 90–108, 2018.

[44] L. Xu, X. Zhao, L. Xi, Y. Ma, J. Gao, and Y. Li, “Large-eddy simulation study of flow and heat transfer in swirling and non-swirling impinging jets on a semi-cylinder concave target,” *Applied Sciences (Switzerland)*, vol. 11, 2021.

[45] L. Xu, Y. Xiong, L. Xi, J. Gao, Y. Li, and Z. Zhao, “Numerical simulation of swirling impinging jet issuing from a threaded hole under inclined condition,” *Entropy*, vol. 22, p. 15, 2020.

[46] H. Fawzy, Q. Zheng, and N. Ahmad, “Effect of slot area ratio and slot angle on swirl cooling in a gas turbine blade leading edge,” *Journal of Aerospace Engineering*, vol. 33, p. 04020046, 2020.

[47] H. Fawzy, Q. Zheng, N. Ahmad, and Y. Jiang, “Optimization of a swirl with impingement compound cooling unit for a gas turbine blade leading edge,” *Energies*, vol. 13, 2020.

[48] F. Afroz and M. A. Sharif, “Numerical investigation of heat transfer from a plane surface due to turbulent annular swirling jet impingement,” *International Journal of Thermal Sciences*, vol. 151, p. 106257, 2020.

[49] C. Agrawal, O. F. Lyons, R. Kumar, A. Gupta, and D. B. Murray, “Rewetting of a hot horizontal surface through mist jet impingement cooling,” *International Journal of Heat and Mass Transfer*, vol. 58, pp. 188–196, 2013.

[50] C. Khangembam and D. Singh, “Experimental investigation of air-water mist jet impingement cooling over a heated cylinder,” *Journal of Heat Transfer*, vol. 141, pp. 1–12, 2019.

[51] C. Khangembam, D. Singh, J. Handique, and K. Singh, “Experimental and numerical study of air-water mist jet impingement cooling on a cylinder,” *International Journal of Heat and Mass Transfer*, vol. 150, 2020.

[52] P. Dutta and H. Chattopadhyay, “Computational analysis of heat transfer due to turbulent annular jet impingement,” *IOP Conference Series: Materials Science and Engineering*, vol. 1080, p. 012031, 2021.

[53] D. Greenblatt, E. A. Whalen, and I. J. Wygnanski, “Introduction to the flow control virtual collection,” *AIAA Journal*, vol. 57, pp. 3111–3114, 2019.

[54] X. Luo, B. Sun, and X. Wang, “Experimental investigation on a cavity-step-actuated supersonic oscillating jet,” *Chinese Journal of Aeronautics*, vol. 30, pp. 274–281, 2017.

[55] G. Raman and S. Raghu, “Cavity resonance suppression using miniature fluidic oscillators,” *AIAA Journal*, vol. 42, pp. 10–13, 2004.

[56] C. Cerretelli and K. Kirtley, “Boundary layer separation control with fluidic oscillators,” *Journal of Turbomachinery*, vol. 131, pp. 1–9, 2009.

[57] H. J. Schmidt, R. Woszidlo, C. N. Nayeri, and C. O. Paschereit, “Separation control with fluidic oscillators in water,” *Exp Fluids*, vol. 58, 2017.

[58] K. Kara, D. Kim, and P. J. Morris, “Flow-separation control using sweeping jet actuator,” *AIAA Journal*, vol. 56, pp. 4604–4613, 2018.

[59] A. Lacarelle and C. O. Paschereit, “Increasing the passive scalar mixing quality of jets in crossflow with fluidics actuators,” *Journal of Engineering for Gas Turbines and Power*, vol. 134, pp. 1–7, 2012.

[60] H. Madadkon, A. Fadaie, and M. Nili-Ahmadabadi, “Experimental and numerical investigation of unsteady turbulent flow in a fluidic oscillator flow meter with extraction of characteristics diagrams,” *Modares Journal of Mechanics Engineering*, vol. 12, pp. 30–42, 2012.

[61] J. S. Ten and T. Povey, "Self-excited fluidic oscillators for gas turbines cooling enhancement: Experimental and computational study," *Journal of Thermophysics and Heat Transfer*, vol. 33, pp. 536–547, 2019.

[62] J. Gregory and M. N. Tomac, "A review of fluidic oscillator development," *AIAA*, pp. 1–26, 2013.

[63] R. Abdelmaksoud and T. Wang, "A review on thermal-fluid behavior in sweeping jet fluidic oscillators," in *5th-6th Thermal and Fluids Engineering Conference (TFEC)*, pp. 979–1003, 2021.

[64] A. J. Amiri and M. Farhadi, "Numerical investigation of a single feedback loop oscillator with two outlet channels," *Chemical Engineering Research and Design*, vol. 150, pp. 206–217, 10 2019.

[65] B. C. Bobusch, R. Woszidlo, J. M. Bergada, C. N. Nayeri, and C. O. Paschereit, "Experimental study of the internal flow structures inside a fluidic oscillator," *Experiments in Fluids*, vol. 54, 2013.

[66] S. Raghu, "Feedback-free fluidic oscillator and method," 2001.

[67] V. Tesar, "Taxonomic trees of fluidic oscillators," in *EFM 2016*, p. 02128, EPJ Web of Conferences, 2017.

[68] R. Stouffer, "Oscillating spray device," 1979.

[69] W. Zhou, L. Yuan, Y. Liu, D. Peng, and X. Wen, "Heat transfer of a sweeping jet impinging at narrow spacings," *Experimental Thermal and Fluid Science*, vol. 103, pp. 89–98, 2019.

[70] B. C. Bobusch, O. Kr, and C. O. Paschereit, "Numerical investigations on geometric parameters affecting the oscillation properties of a fluidic oscillator," in *21st AIAA Computational Fluid Dynamics Conference*, pp. 1–15, 2013.

[71] Y. Sang, Y. Shan, H. Lei, X. Tan, and J. Zhang, "Effects of geometric parameters on the physica[1] y. sang, y. shan, h. lei, x. tan, and j. zhang, "effects of geometric parameters on the physical mechanisms of supersonic fluidic

oscillators," energies, vol. 13, no. 3919, 2020.l mechanisms of supersonic," *Energies*, vol. 13, 2020.

[72] M. Koklu, "Effects of sweeping jet actuator parameters on flow separation control," *AIAA Journal*, vol. 56, pp. 1–11, 2018.

[73] M. Baghaei and J. M. Bergada, "Fluidic oscillators , the effect of some design modifications," *Applied Sciences (Switzerland)*, vol. 10, 2020.

[74] J. M. Bergadà, M. Baghaei, B. Prakash, and F. Mellibovsky, "Fluidic oscillators , feedback channel effect under compressible flow conditions," *Sensors (Switzerland)*, vol. 21, pp. 1–23, 2021.

[75] A. Abdulnaim, A. Emara, and H. Moneib, "Influence of exit configuration on the flow fields and oscillation characteristics inside and outside the fluidic oscillator influence of exit. influence of exit configuration on the flow fields and oscillati," in *IOP Conf. Series: Materials Science and Engineering*, p. 012052, 2019.

[76] F. Ostermann, R. Woszidlo, C. N. Nayeri, and C. O. Paschereit, "Experimental comparison between the flow field of two common fluidic oscillator designs," *53rd AIAA Aerospace Sciences Meeting*, pp. 1–14, 2015.

[77] M. Nili-Ahmadabadi, D. S. Cho, and K. C. Kim, "Design of a novel vortex-based feedback fluidic oscillator with numerical evaluation," *Engineering Applications of Computational Fluid Mechanics*, vol. 14, pp. 1302–1324, 2020.

[78] M. N. Tomac and E. Sundström, "Fluidic oscillator with variable sweep and inclination angles," *AIAA Journal*, vol. 58, pp. 1182–1193, 2020.

[79] N. H. Kim and K. Y. Kim, "Effects of bent outlet on characteristics of a fluidic oscillator with and without external flow," *Energies*, vol. 14, 2021.

[80] S. Mohammadshahi, H. Samsam-Khayani, Z. Deng, and K. C. Kim, "Experimental investigation of flow dynamics of oscillating jet emitted in confined and non-confined backward-facing step geometries," *European Journal of Mechanics, B/Fluids*, vol. 88, pp. 89–102, 2021.

[81] A. Tajik, K. Kara, and V. Parezanovic, “Sensitivity of a fluidic oscillator to modifications of feedback channel and mixing chamber geometry,” *Experiments in Fluids*, vol. 62, pp. 1–19, 2021.

[82] W. Zhou, K. Wang, T. Yuan, X. Wen, D. Peng, and Y. Liu, “Spatiotemporal distributions of sweeping jet film cooling with a compact geometry,” *Physics of Fluids*, vol. 34, p. 025113, 2 2022.

[83] F. Oz and K. Kara, “Jet oscillation frequency characterization of a sweeping jet actuator,” *Fluids*, 2020.

[84] S. Aram and H. Shan, “Computational analysis of interaction of a sweeping jet with an attached crossflow,” *AIAA Journal*, pp. 1–14, 2018.

[85] M. Alam and K. Kara, “The influence of exit nozzle geometry on sweeping jet actuator performance,” *Fluids*, vol. 7, 2022.

[86] J. Song, S. Wang, Z. Qiu, and et al., “Flow mechanism study and geometrical parameters analysis of fluidic oscillators based on pressure-sensitive paint measurements and modal analysis,” *Experiments in Fluids*, vol. 65, p. 38, 2024.

[87] W. Zhai and Y. Fan, “Influence of structural parameters on the performance of fluid oscillators,” *European Journal of Mechanics, B/Fluids*, vol. 109, pp. 367–377, 1 2025.

[88] J. Yang, X. Zhang, Y. Luo, L. Tang, and B. Liang, “Numerical parametric study of a sweeping-vortex low-frequency fluidic oscillator,” *International Journal of Mechanical Sciences*, vol. 271, 6 2024.

[89] R. Woszidlo, F. Ostermann, C. N. Nayeri, and C. O. Paschereit, “The time-resolved natural flow field of a fluidic oscillator,” *Experiments in Fluids*, vol. 56, pp. 1–12, 2015.

[90] B. J. Slupski and K. Kara, “Effects of geometric parameters on performance of sweeping jet actuator,” in *34th AIAA Applied Aerodynamics Conference*, pp. 1–13, 2016.

[91] M. Hossain, R. Prenter, L. Agricola, R. Lundgreen, A. Ameri, J. Gregory, and J. Bons, “Effects of roughness on the performance of fluidic,” in *55th AIAA Aerospace Sciences Meeting*, 2017.

[92] H. Samsam-Khayani, S. Mohammadshahi, and K. C. Kim, “Experimental study on physical behavior of fluidic oscillator in a confined cavity with sudden expansion,” *Applied Sciences (Switzerland)*, vol. 10, pp. 1–17, 2020.

[93] X. Wen, Y. Liu, and H. Tang, “Unsteady behavior of a sweeping impinging jet : Time-resolved particle image velocimetry measurements,” *Experimental Thermal and Fluid Science*, 2018.

[94] Z. Li, J. Liu, W. Zhou, Y. Liu, and X. Wen, “Experimental investigation of flow dynamics of sweeping jets impinging upon confined concave surfaces,” *International Journal of Heat and Mass Transfer*, vol. 142, p. 118457, 2019.

[95] S. Aram and A. Dejong, “Numerical comparison between steady and sweeping jets for active flow control applications,” in *ASME 2018*, pp. 1–17, 2018.

[96] M. Fuchiwaki and S. Raghu, “Flow structure formed by a sweeping jet ejected into a main flow,” in *ASME 2018*, pp. 1–6, 2019.

[97] J. G. Zheng, L. Xia, J. Hu, and Y. J. Mao, “Numerical investigation of characteristics of fluidic oscillator operating in quiescent air and a crossflow,” *Aerospace Science and Technology*, vol. 113, 2021.

[98] X. Wen, Z. Li, W. Zhou, Y. Liu, X. Wen, Z. Li, W. Zhou, and Y. Liu, “Interaction of dual sweeping impinging jets at different reynolds numbers interaction of dual sweeping impinging jets at different reynolds numbers,” *Physics of Fluids*, vol. 30, 2018.

[99] Q. Meng, X. Du, S. Chen, and S. Wang, “Numerical study of dual sweeping jet actuators for corner separation control in compressor cascade,” *Journal of Thermal Science*, vol. 30, pp. 201–209, 2019.

[100] M. N. Tomac and J. W. Gregory, “Oscillation characteristics of mutually impinging dual jets in a mixing chamber in a mixing chamber,” *Physics of Fluids*, vol. 117102, 2018.

[101] M. Tomac and M. Hossain, “Flow and frequency characterization of the synchronized stacked sweeping jets,” *AIAA Journal*, pp. 1–13, 2021.

[102] E. T. Sundström and M. N. Tomac, “Synchronization and flow characteristics of the opposed facing oscillator pair in back-to-back configuration,” *Flow, Turbulence and Combustion*, 2019.

[103] S. H. Kim and K. Y. Kim, “Effects of installation location of fluidic oscillators on aerodynamic performance of an airfoil,” *Aerospace Science and Technology*, vol. 99, p. 105735, 2020.

[104] N. H. Kim and K. Y. Kim, “Effects of bending of fluidic oscillators on aerodynamic performance of an airfoil with a flap,” *Processes*, vol. 9, 2021.

[105] L. P. Melton, M. Koklu, M. Andino, and J. C. Lin, “Active flow control via discrete sweeping and steady jets on a simple-hinged flap,” *AIAA Journal*, vol. 56, pp. 2961–2973, 2018.

[106] S. H. Tseng, Y. T. Yang, J. Allen, and S. L. Yang, “Numerical simulation of a fluidic oscillator for water removal enhancement in pem fuel cell,” *2008 Proceedings of the ASME Micro/Nanoscale Heat Transfer International Conference, MNHT 2008*, vol. PART A, pp. 219–227, 2008.

[107] G. S. Jones, W. E. Milholen, J. S. Fell, S. R. Webb, and C. M. Cagle, “Using computational fluid dynamics and experiments to design sweeping jets for high reynolds number cruise configurations,” in *8th AIAA Flow Control Conference*, pp. 1–21, 2016.

[108] R. J. Pandey and K. Y. Kim, “Comparative analysis of flow in a fluidic oscillator using large eddy simulation and unsteady reynolds-averaged navier-stokes analysis,” *Fluid Dynamics Research*, 2018.

[109] S. Martinke, R. Woszidlo, C. N. Nayeri, and C. O. Paschereit, “Characteristics of modified fluidic oscillator with adjustable flow parameters,” *AIAA Journal*, vol. 63, no. 7, pp. 2721–2730, 2025.

[110] F. Herr and C. Camci, “Self-oscillating-impinging-jet as a gas turbine cooling enhancement system,” in *Proceedings of the ASME 1997 International Gas Turbine and Aeroengine Congress and Exhibition.*, ASME, 6 1997.

[111] C. Camci and F. Herr, “Enhancement using a self-oscillating impinging planar,” *Transactions of the ASME*, vol. 124, pp. 771–782, 2002.

[112] X. Wen, J. Liu, Z. Li, D. Peng, W. Zhou, K. C. Kim, and Y. Liu, “Jet impingement using an adjustable spreading-angle sweeping jet,” *Aerospace Science and Technology*, vol. 105, p. 105956, 2020.

[113] M. Kim, D. Kim, E. Yeom, and K. C. Kim, “Experimental study on heat transfer and flow structures of feedback-free sweeping jet impinging on a flat surface,” *International Journal of Heat and Mass Transfer*, vol. 159, p. 120085, 2020.

[114] M. N. Tomac, “Novel impinging jets-based non-periodic sweeping jets,” *Journal of Visualization*, vol. 23, pp. 369–372, 2020.

[115] R. K. Lundgreen, M. A. Hossain, R. Prenter, J. P. Bons, J. Gregory, and A. Ameri, “Impingement heat transfer characteristics of a sweeping jet,” *AIAA SciTech Forum - 55th AIAA Aerospace Sciences Meeting*, pp. 1–11, 2017.

[116] L. Agricola, M. A. Hossain, R. Prenter, R. Lundgreen, A. Ameri, J. Gregory, and J. P. Bons, “Impinging sweeping jet heat transfer,” in *53rd AIAA/SAE/ASEE Joint Propulsion Conference, 2017*, pp. 1–18, 2017.

[117] D. Thurman, P. Poinsatte, A. Ameri, and D. Culley, “Investigation of spiral and sweeping holes,” *Journal of Turbomachinery*, vol. 138, pp. 1–11, 2017.

[118] M. A. Hossain, L. M. Agricola, A. Ameri, J. W. Gregory, and J. P. Bons, “Effects of exit fan angle on the heat transfer performance of sweeping jet impingement,” *2018 International Energy Conversion Engineering Conference*, pp. 1–19, 2018.

[119] T. Park, K. Kara, and D. Kim, “Flow structure and heat transfer of a sweeping jet impinging on a flat wall,” *International Journal of Heat and Mass Transfer*, vol. 124, pp. 920–928, 2018.

[120] L. Agricola, M. A. Hossain, A. Ameri, J. W. Gregory, and J. P. Bons, “Turbine vane leading edge impingement cooling with a sweeping jet,” in *Proceedings of ASME Turbo Expo 2018 Turbomachinery Technical Conference and Exposition GT2018 June 11-15, 2018, Oslo, Norway*, pp. 1–11, 2018.

[121] A. Spens and J. P. Bons, *Experimental Investigation of Synchronized Sweeping Jets for Film Cooling Application.* American Institute of Aeronautics and Astronautics, 1 2021. doi:10.2514/6.2021-2003.

[122] M. A. Hossain, L. Agricola, A. Ameri, J. W. Gregory, and J. P. Bons, “Sweeping jet impingement heat transfer on a simulated turbine vane leading edge,” in *GPPS Forum 18 Global Power and Propulsion Society*, pp. 7–9, 2018.

[123] Y. Wu, S. Yu, and L. Zuo, “Large eddy simulation analysis of the heat transfer enhancement using self-oscillating fluidic oscillators,” *International Journal of Heat and Mass Transfer*, vol. 131, pp. 463–471, 2019.

[124] S. Ghanami and M. Farhadi, “Heat transfer enhancement in a single-pipe heat exchanger with fluidic oscillators,” *Journal of Thermal Analysis and Calorimetry*, vol. 140, pp. 1107–1119, 2020.

[125] S. H. Kim, H. D. Kim, and K. C. Kim, “Measurement of two-dimensional heat transfer and flow characteristics of an impinging sweeping jet,” *International Journal of Heat and Mass Transfer*, vol. 136, pp. 415–426, 2019.

[126] S. Mohammadshahi, H. Samsam-khayani, T. Cai, M. Nili-ahmadabadi, and K. Chun, “Experimental study on flow characteristics and heat transfer of an oscillating jet in a cross flow,” *International Journal of Heat and Mass Transfer*, vol. 173, p. 121208, 2021.

[127] B. N. Hewakandamby, “A numerical study of heat transfer performance of oscillatory impinging jets,” *International Journal of Heat and Mass Transfer*, vol. 52, pp. 396–406, 2009.

[128] A. Eghtesad, M. Mahmoudabadbozchelou, and H. Afshin, “Heat transfer optimization of twin turbulent sweeping impinging jets,” *International Journal of Thermal Sciences*, vol. 146, p. 106064, 2019.

[129] M. A. Hossain, R. Prenter, R. K. Lundgreen, A. Ameri, J. W. Gregory, and J. P. Bons, “Experimental and numerical investigation of sweeping jet film cooling,” *Journal of Turbomachinery*, vol. 140, 2018.

[130] M. A. Hossain, A. Ameri, J. W. Gregory, and J. Bons, “Effects of fluidic oscillator nozzle angle on the flowfield and impingement heat transfer,” *AIAA Journal*, vol. 59, pp. 2113–2125, 2021.

[131] S. Mohammadshahi, H. Samsam-Khayani, T. Cai, and K. C. Kim, “Experimental and numerical study on flow characteristics and heat transfer of an oscillating jet in a channel,” *International Journal of Heat and Fluid Flow*, vol. 86, p. 108701, 2020.

[132] T. Ming, Z. Wang, X. Liao, T. Shi, G. Tan, and Y. Wu, “Unsteady rans simulation of fluid dynamic and heat transfer in an oblique self-oscillating fluidic oscillator array,” *International Journal of Heat and Mass Transfer*, vol. 177, p. 121515, 2021.

[133] M. A. Hossain, L. M. Agricola, A. Ameri, J. W. Gregory, and J. P. Bons, “Effects of curvature on the performance of sweeping jet impingement heat transfer,” *AIAA Aerospace Sciences Meeting, 2018*, pp. 1–14, 2018.

[134] D. J. Kim, S. Jeong, T. Park, and D. Kim, “Impinging sweeping jet and convective heat transfer on curved surfaces,” *International Journal of Heat and Fluid Flow*, vol. 79, p. 108458, 2019.

[135] A. Osorio, J. Hodges, H. Zawati, E. Fernandez, J. Kapat, and J. Rodriguez, “Impact of sweeping jet on area-averaged impingement heat transfer,” in *Turbo Expo: Power for Land, Sea and Air*, 2019.

[136] X. Kong, Y. Zhang, G. Li, X. Lu, J. Zhu, and J. Xu, “Numerical simulation of the flow and heat transfer characteristics of sweeping and direct jets on a flat plate with film holes,” *Energies*, vol. 15, p. 4470, 2022.

[137] R. Abdelmaksoud and T. Wang, “Simulation of a confined and a free sweeping air jet impingement cooling from a fluidic oscillator,” *International Journal of Thermal Sciences*, vol. 193, 11 2023.

[138] A. Joulaei, M. Nili-Ahmadabadi, and K. C. Kim, “Parametric study of a fluidic oscillator for heat transfer enhancement of a hot plate impinged by a sweeping jet,” *Applied Thermal Engineering*, vol. 205, p. 118051, 2022.

[139] R. Woszidlo, F. Ostermann, and H. J. Schmidt, “Fundamental properties of fluidic oscillators for flow control applications,” *AIAA Journal*, vol. 57, pp. 978–992, 2019.

[140] B. J. Slupski, A. R. Tajik, V. B. Parezanović, and K. Kara, “On the impact of geometry scaling and mass flow rate on the frequency of a sweeping jet actuator,” *FME Transactions*, vol. 47, pp. 599–607, 2019.

[141] A. Joulaei, M. Nili-Ahmadabadi, and M. Y. Ha, “Numerical study of the effect of geometric scaling of a fluidic oscillator on the heat transfer and frequency of impinging sweeping jet,” *Applied Thermal Engineering*, vol. 221, 2 2023.

[142] H. S. Jeong and K. Y. Kim, “Shape optimization of a feedback-channel fluidic oscillator,” *Engineering Applications of Computational Fluid Mechanics*, vol. 12, pp. 169–181, 2018.

[143] S. Park, H. Ko, M. Kang, and Y. Lee, “An experimental study of the characteristics of a supersonic fluidic oscillator utilizing the design of experiment,” in *AIAA Aviation 2019 Forum*, pp. 1–11, American Institute of Aeronautics and Astronautics Inc, AIAA, 2019.

[144] D. Y. Sheng, “Design optimization of a single-strand tundish based on cfd-taguchi-grey relational analysis combined method,” *Metals*, vol. 10, pp. 1–22, 11 2020.

[145] M. Younas, S. H. I. Jaffery, M. Khan, M. A. Khan, R. Ahmad, A. Mubashar, and L. Ali, “Multi-objective optimization for sustainable turning ti6al4v alloy using grey relational analysis (gra) based on analytic hierarchy process (ahp),” *International Journal of Advanced Manufacturing Technology*, vol. 105, pp. 1175–1188, 11 2019.

[146] J. Tang and Z. Li, “Adjoint shape optimization for enhanced heat transfer in sweeping jet impingement on concave surface,” *International Communications in Heat and Mass Transfer*, vol. 159, 12 2024.

[147] H. Jabbari and A. Esmaeili, “Enhancing fluidic oscillator performance for improved outlet jet frequency and reduced pressure drops by the adjoint method,” *Arabian Journal for Science and Engineering*, 2025.

[148] K. M. Kim, H. Moon, J. S. Park, and H. H. Cho, “Optimal design of impinging jets in an impingement/effusion cooling system,” *Energy*, vol. 66, pp. 839–848, 3 2014.

[149] K. Kara, “Numerical study of internal flow structures in a sweeping jet actuator,” in *AIAA Aviation, 33rd AIAA Applied Aerodynamics Conference*, pp. 1–17, 2015.

[150] B. Jurewicz and K. Kara, “Effects of feedback channels and coanda surfaces on the performance of sweeping jet actuator,” *AIAA SciTech Forum - 55th AIAA Aerospace Sciences Meeting*, pp. 1–13, 2017.

[151] O. Krüger, B. C. Bobusch, R. Woszidlo, and C. O. Paschereit, "Numerical modeling and validation of the flow in a fluidic oscillator," in *21st AIAA Computational Fluid Dynamics Conference*, American Institute of Aeronautics and Astronautics Inc., 2013.

[152] F. R. Menter, M. Kuntz, and R. Langtry, "Ten years of industrial experience with the sst turbulence model," *Turbulence, Heat and Mass Transfer 4*, 2003.

[153] B. E. Launder and N. D. Sandham, *Closure strategies for turbulent and transitional flows.* Cambridge University Press, 2002.

[154] M. Kilic, T. Calisir, and S. Baskaya, "Experimental and numerical study of heat transfer from a heated flat plate in a rectangular channel with an impinging air jet," *Journal of the Brazilian Society of Mechanical Sciences and Engineering*, vol. 39, pp. 329–344, 1 2017.

[155] R. J. Pandey and K. yong Kim, "Numerical modeling of internal flow in a fluidic oscillator," *Journal of Mechanical Science and Technology*, vol. 32, pp. 1041–1048, 2018.

[156] J.-L. Deng, "Control problems of grey systems," *Systems and Control Letters*, 1982.

[157] C. M. Khalde, A. V. Pandit, J. S. Sangwai, and V. V. Ranade, "Flow, mixing, and heat transfer in fluidic oscillators," *Canadian Journal of Chemical Engineering*, vol. 97, pp. 542–559, 2 2019.